

Mechanical characterisation and constitutive modelling of wrought magnesium sheets exhibiting tension-compression asymmetry

**Vom Promotionsausschuss der
Technischen Universität Hamburg-Harburg**

zur Erlangung des akademischen Grades

Doktor-Ingenieurin (Dr.-Ing.)

genehmigte Dissertation

von

Xiaowei Tian

aus China

2017

Vorsitzender des Promotionsverfahrens:

Prof. Dr.-Ing. Norbert Huber (TUHH)

Gutachter der Dissertation:

1. Gutachter: Prof. Dr.-Ing. Swantje Bargmann (Bergische Universität Wuppertal)
2. Gutachter: Prof. Dr.-Ing. Benjamin Klusemann (Leuphana Universität Lüneburg)

Tag der mündlichen Prüfung:

Montag, 13. March 2017

Abstract

Wrought magnesium alloys have emerged as promising candidates for highly loaded structural components in the automobile industry recently, due to their high specific strength and low density. In this work, two aspects of wrought magnesium alloys are studied experimentally and computationally: the mechanism-based modelling of plastic deformation and the crashworthiness assessment of simple structures. A constitutive model was developed to capture the plastic behaviour of wrought magnesium sheets under monotonic loading. Wrought magnesium sheets exhibit a strong and evolving tension-compression asymmetry in terms of flow stress and r -value (strain anisotropy parameter). A yield function originally proposed by Cazacu, Plunkett and Barlat in 2006 was extended by introducing a new parameter depending on the plastic multiplier to describe this tension-compression asymmetry and its evolution.

The model was applied to two different magnesium wrought alloys, AZ31 (Mg+3%Al+1%Zn) and ZE10 (Mg+1%Zn+0.3%Ce), each produced as rolled sheet and as extruded profile. A series of mechanical tests including uniaxial tensile and compression tests along different orientations, through thickness compression tests, shear tests, and notched bar tests was conducted for characterising the mechanical behaviour under various stress states. Experimental results confirm significantly different plastic deformation behaviour of the two alloys, which were resulted from their respective initial textures. For calibration of the material model, identification of material parameters was accomplished with the experimental data based on an error minimisation scheme.

The computational results show that the proposed model captures the tension-compression asymmetry of both alloys. The calibrated model was finally applied to a pure bending simulation. The good agreement between the simulated and the semi-analytically calculated bending moment-curvature diagram demonstrates the predictive capability of the present model for the considered magnesium alloys. Experimental study and numerical simulations were conducted to investigate the plastic buckling and crush behaviour of structural components with hollow rectangular profiles fabricated from the two magnesium alloys. The used modelling approach is justified by balancing achievable accuracy and computational efforts. The performance of the components made by magnesium alloys was evaluated in term of the dissipated specific energy in the crush tests and compared with respective aluminium components. It is revealed that the observed high dissipation of magnesium alloys during crushing is related to the work hardening behaviour in compression.

Kurzfassung

Magnesiumlegierungen sind heutzutage aufgrund der hohen spezifischen Festigkeit und geringen Dichte aussichtsreiche Kandidaten für hochbelastete Strukturbauteile in der Automobilindustrie. In dieser Arbeit werden zwei Aspekte der Eigenschaften von Magnesiumlegierungen in dieser Arbeit experimentell und numerisch untersucht: die Mechanismus-basierte Modellierung der plastischen Verformung und die Beurteilung der Kollisionssicherheit von einfachen Strukturen. Zunächst wird ein Konstitutivmodell zur Beschreibung des mechanischen Verhaltens von Magnesiumblechen unter monotoner Belastung entwickelt. Magnesiumbleche zeigen eine starke und sich mit der Verformung entwickelnde Zug-Druck-Asymmetrie in der Fließspannung und dem R-Wert (Dehnungsanisotropie-Parameter). Eine von Cazacu, Plunkett und Barlat in 2006 vorgeschlagene Fließfunktion wird durch die Einführung der Abhängigkeit eines Parameters vom plastischen Multiplikator zur Beschreibung der Zug-Druck-Asymmetrie und ihrer Evolution erweitert.

Das Modell wird auf zwei unterschiedliche Magnesiumlegierungen angewendet: AZ31 (Mg+3%Al+1%Zn) und ZE10 (Mg+1%Zn+0.3%Ce), die jeweils als gewalztes Blech und als extrudiertes Profil hergestellt wurden. Eine Reihe von mechanischen Versuchen wird zur Charakterisierung der mechanischen Eigenschaften unter verschiedenen Spannungszuständen durchgeführt, einschließlich einachsiger Zug- und Druckversuche mit unterschiedlichen Orientierungen, Kompressions-, Scher- und Kerbversuche. Die Versuchsergebnisse zeigen, dass die beiden Magnesiumlegierungen sehr unterschiedliches plastisches Verformungsverhalten aufweisen, das von den jeweiligen Anfangstexturen erklärt wird. Für die Kalibrierung der Parameter des Materialmodells wird ein Fehlerminimierungsschema verwendet.

Das kalibrierte Modell erfasst die Zug-Druck-Asymmetrie beider Legierungen. Schließlich wird das Modell in einer reinen Biegesimulation eingesetzt. Die Übereinstimmung zwischen dem simulierten und dem semi-analytisch berechneten Biegemoment-Krümmung Diagramm zeigt die Vorhersagefähigkeit des Modells für die beiden betrachteten Magnesiumlegierungen. Experimentelle Untersuchungen und numerische Simulationen werden zur Voraussage und Beurteilung des plastischen Beulens und des Aufprallverhaltens von rechteckigen Hohlprofilen durchgeführt, die aus den beiden Magnesiumlegierungen hergestellt sind. Der angewandte Modellierungsansatz berücksichtigt den Kompromiss zwischen erreichbarer Genauigkeit und benötigtem Rechenaufwand. Die Leistungsfähigkeit der Bauteile wurde anhand der spezifischen dissipierten Energie ausgewertet und mit entsprechenden Aluminiumbauteilen verglichen. Es zeigt sich, dass die beobachtete hohe Dissipation der Bauteile aus den Magnesiumlegierungen während des Aufpralls durch das Verfestigungsverhalten unter Druck verursacht wird.

Acknowledgements

The current thesis is a report of the research work carried out at Helmholtz Zentrum Geesthacht from January 2012 until December 2015. This could not have been accomplished without the smart supervision, constant support, encouragement and help of my supervisor, Professor Bargmann. I would like to express my heartfelt gratitude to her.

I am deeply indebted to Dr. Dirk Steglich, who introduced me to the topic of the research work. I am grateful for his patience, support and all the fruitful discussions.

My sincere appreciation to Dr. Jan Bohlen, Jürgen Knaack and Kay Erdmann who provided me with the required experimental facilities and for the valuable discussions which ultimately shaped up this work.

I would like to express my sincere gratitude to Dr. Ingo Scheider, M.Sc. Jana Wilmers and M.Sc. Mamum Al-Siraj for their brilliant minds and great help.

I would like to thank all members of the department and appreciate their help, specially M.Sc. Edgar Husser, Dr. Songyun Ma, Dr. Lidiia Nazarenko, M.Sc. Jan-Eike Butzke and M.Sc Sebastian Glane.

I would like to acknowledge Professor Norbert Huber for the opportunity I was given to be part of his research work.

I am also grateful to Mr. Le Zhang and all my friends in Geesthacht. It could not have been a colourful and impressive life without their help.

Last but not least, I wish to thank my parents, Mr. Jun Tian and Mrs. Zhonghe Zhai, as well as my sister Mrs. Xiaomin Tian. They guided me to understand the principle of life and the attitude for work. Without their unconditional support, love and encouragement, this work could not have been accomplished.

Contents

1	Introduction	1
2	Physical and modelling background	5
2.1	Deformation mechanisms of magnesium	5
2.1.1	Basal slip	6
2.1.2	Non-basal slip	7
2.1.3	Twinning	7
2.1.4	Magnesium alloy with rare earth elements	9
2.2	Phenomenological modelling of plastic deformation in metals .	9
2.2.1	Yield criterion	10
2.2.1.1	Isotropic yield criterion	10
2.2.1.2	Anisotropic yield criterion	12
2.2.2	Flow rule	14
2.2.3	Work hardening	15
2.2.3.1	Isotropic hardening	15
2.2.3.2	Distortional hardening	16
2.3	Constitutive model for wrought magnesium sheets	17
2.4	Fitting of the model parameters	22
3	Mechanical characterisation	25
3.1	Materials under investigation	25
3.2	Experimental setup	27
3.2.1	Tensile tests	27
3.2.2	Uniaxial compression tests	30
3.2.3	Through thickness compression tests	32
3.2.4	U-notched bar tensile test	33
3.2.5	Shear tests	34
3.3	Mechanical responses	36
3.3.1	Uniaxial tensile tests	36
3.3.2	Uniaxial compression tests	39
3.3.3	Through thickness compression tests	41
3.3.4	U-notched bar tensile tests	47
3.3.5	Shear tests	47
3.4	Conclusions	48
4	Model parameter identification	51
4.1	Determination of isotropic hardening	51
4.2	Parameter identification strategy	52
4.3	Parameter calibration	54

4.3.1	CPB2006 model	54
4.3.2	Modified CPB2006 model	54
4.4	Macroscopic effects described by the two models	55
4.5	Pure bending simulation	71
5	Crashworthiness of magnesium sheets structure	75
5.1	Configurations and manufacturing of hollow rectangular profiles	75
5.2	Crush test	76
5.3	Finite element simulation	76
5.4	Results	78
5.5	Discussion	83
6	Summary and conclusion	85

1 Introduction

Magnesium alloy is the third most commonly used structural metal, following steel and aluminium alloy. Its density is about one-fourth of steel and two-thirds of aluminium. The specific strength and stiffness of magnesium exceeds that of most commonly used metals. As the lightest structural metal, magnesium offers great possibility for lightweight applications in automotive and aerospace industries.

Magnesium has a long history in automotive use. In 1935, Bugatti Aêrolithe concept car debuted. It used Elektron (a magnesium alloy) for its body panels. With the introduction of the Volkswagen Type 1, automotive magnesium consumption again accelerated and reached a peak in 1971, the major applications being the air-cooled engine and gearbox which are all cast products. Recently, high-pressure die casting is the dominant manufacturing process for automotive magnesium applications. The applications then expanded to instrumental panels, steering wheels and steering column components. However, the use of wrought magnesium (sheets and extrusions) is still in the development stage and receives increased attention from industry. Compared with magnesium castings, wrought magnesium alloys offer better mechanical properties (higher strength and higher ductility), and provide further mass saving opportunities. Automotive body constructions offer a great potential for the application of magnesium sheet metal components. In general, the automotive body completely consists of sheet metal parts and represents a share of about 25% of the entire vehicle mass. Therefore, the substitution of conventional sheet materials by magnesium sheets would lead to essential weight savings in this application.

Except to minimise the weight of the car itself and therefore reduce the fuel consumption, the first necessity is to validate the crashworthiness of magnesium structures. Crashworthiness is the ability of a restraint system or component to withstand loads below a certain level and to reduce the damage caused in the crash scenario. An efficient crashworthy system should be able to dissipate the kinetic energy of the impact in a controllable manner. Modelling is an efficient tool to investigate the crashworthiness behaviour of magnesium structures and thus enabling cost reduction and shortening of the crashworthiness design phase. A constitutive model, a mathematical description of the mechanical behaviour of the wrought magnesium sheet, is needed to improve the reliability of the modelling results.

In this work, the plastic deformation of two different magnesium sheets (AZ31 and ZE10) under quasi-static loading conditions at room temperature is studied. Both rolled sheets and extruded products are under investigation. The

rolled sheets are received from the former Salzgitter Magnesium Technology SZMT of Germany. The extrusion is done at the Extrusion Research Centre of TU Berlin. In order to better understand the mechanical behaviour of wrought magnesium sheets and provide necessary input for the constitutive model, a comprehensive set of experiments is conducted which includes the standard uniaxial tensile tests, uniaxial in-plane compression tests using layered sheets, through thickness compression tests, shear tests and U-notched bar tensile tests. Moreover, for the purpose of evaluating the crashworthiness of magnesium sheet structures, the performance of hollow rectangular profiles produced from magnesium alloys AZ31 and ZE10 under quasi-static macroscopic compressive axial loading is investigated experimentally and numerically. These experiments are conducted within the joining technologies group and the magnesium innovations centre MagIC of Helmholtz-Zentrum Geesthacht HZG.

A typical attribute of wrought magnesium sheets is the strength differential effect. Wrought magnesium alloys have larger yield stress in tension than compression. Moreover, the hardening evolution differs significantly between tension and compression. In addition, wrought magnesium shows a pronounced anisotropy, which means the mechanical properties (e.g., yield strength) depend on the material direction. Taking the uniaxial tensile test of rolled sheets as an example, the anisotropy can be reflected in two aspects. Firstly, the yield strength and work hardening behaviour are different in rolling direction (RD) and transverse direction (TD). Secondly, the strain anisotropy parameter r -value, which is the ratio between plastic strain in width and the thickness of the sheet, is bigger than unity (for isotropic material r -value equals to 1). It means the material tends to flow in width direction (in plane of the sheet) but not in thickness direction (normal to the sheet). It is an advantage of the magnesium sheets because one of the defects happened in deep drawing is the fracture deduced by the thinning of the sheets while for wrought magnesium alloy which has high r -value will depress the thinning. Furthermore, wrought magnesium shows abnormal hardening under biaxial loading conditions. The hardening rate recorded under biaxial tension is higher than that of uniaxial tension so that the stress strain curves under the two loading conditions are not parallel to each other. This is called differential hardening effect. Mechanical behaviour under biaxial stress state should be investigated because forming operations as well as service conditions generally involve multi-axial loadings.

Considering the complicated mechanical behaviour mentioned above, the reliable constitutive model for the application of wrought magnesium alloys is required and this needs non-state-of-the-art simulation techniques. The CPB2006 (Cazacu et al., 2006) yield function is adopted and extended in this work. The CPB2006 yield function could describe the tension compression

asymmetry and the initial plastic anisotropy by the introducing of the asymmetry parameter and the linear transformation approach. In this research, the asymmetry parameter is modified to be evolved respectively in tension and compression to account for the evolute strength differential effect. Moreover, the anisotropy parameters in the linear transformation tensor are also evolved according to suitable evolution equations to describe the anisotropy of magnesium sheets. Having calibrated the constitutive model based on the mechanical characterisation, this model is applied to simulate the pure bending test which includes both tension and compression stress states.

The crush tests were performed to assess the crashworthiness behaviour of magnesium sheet structures. An isotropic Hill plasticity model with the hardening evolution obtained from the uniaxial compression test results was employed in the numerical analyses of the crush test.

2 Physical and modelling background

2.1 Deformation mechanisms of magnesium

Wrought magnesium sheets exhibit a complex mechanical behaviour. This is related to its hexagonal close-packed (hcp) structure and texture (distribution of crystallographic orientations) developed during rolling or extrusion. This section discusses the deformation mechanisms and alloy effects which are responsible for mechanical behaviours of wrought magnesium sheets.

The slip and twin systems which are activated in magnesium are shown in Fig. 2.1. The basal, prismatic and 1st order pyramidal slip systems produce deformations perpendicular to c-axis so that they cannot produce any deformation along c-axis direction, see Al-Samman and Gottstein (2008). The deformation mechanisms which can accommodate c-axis strains are the 2nd order pyramidal slip system and the two twinning modes.

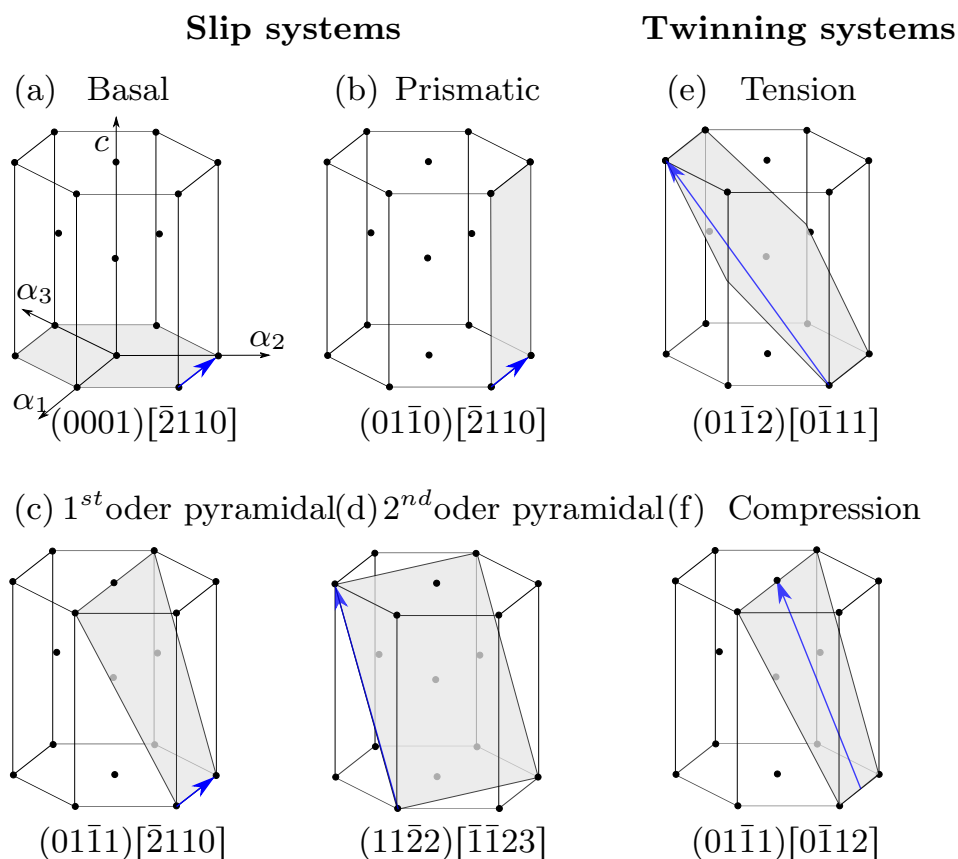


Figure 2.1: Deformation modes in hcp Mg: (a) basal, (b) prismatic, (c) 1st order pyramidal, (d) 2nd order pyramidal slip systems and (e) tension and (f) compression twinning systems (John and Jens, 1982)

2.1.1 Basal slip

Basal slip is responsible to accommodate a big fraction of the total plastic strain in the deformation at room temperature, because it is the softest slip system for magnesium alloys, or in other words the critical resolved shear stress (CRSS) of basal slip is the lowest (about 0.3 MPa) among all of the slip systems, see Kim (2011). CRSS is the component of shear stress, resolved in the direction of slip, necessary to initiate slip in a grain. It is a constant for a given crystal and can be obtained by single crystal experiments.

Although basal slip systems are the softest deformation mechanisms for magnesium, it is not sufficient to accommodate all arbitrary strains. On one hand, there are three α type dislocations glide towards three α axis directions on basal planes and only two of them are independent, see Fig. 2.1(a). However, Taylor (1938) suggests that at least five independent easy slip systems are necessary for uniform arbitrary deformation. On the other hand, crystallographic texture has a significant impact on the activities of the slip systems, since c-axes orientation strongly influences the ease of basal slip. For wrought magnesium sheets which have strongly textured polycrystals (c-axes tends to be perpendicular to the sheet plane), basal slips are not so easy to be activated, see Fig. 2.2 which exhibits the texture and the schematic view of the crystal orientation of the traditional magnesium alloy sheet AZ31 (Mg + 3%Al + 1%Zn). Consequently, it is necessary to discuss also non-basal slip systems.

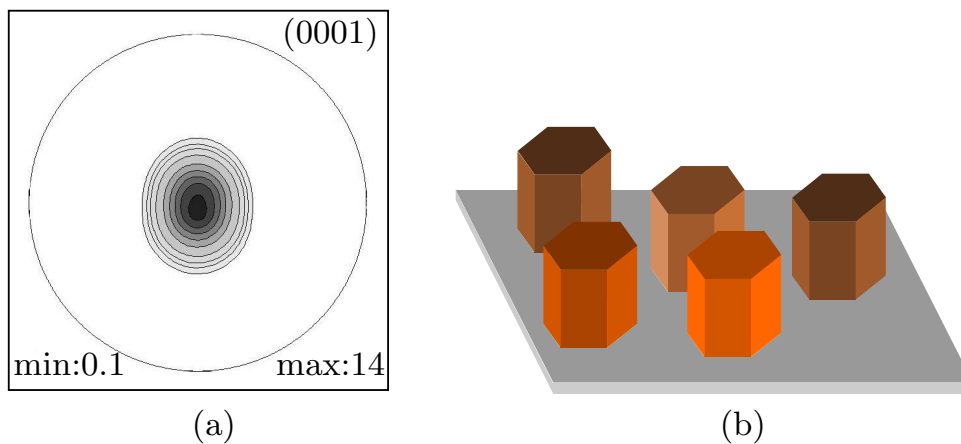


Figure 2.2: (a) Pole figure of basal plane of AZ31 rolled magnesium sheets (Steglich et al., 2014), (b) Schematic view of crystal orientation of the rolled sheets

2.1.2 Non-basal slip

As discussed in the last section, basal slip cannot accommodate all plastic deformation so that the importance of non-basal slip should also be emphasised. Magnesium and its alloy exhibit tensile elongation until failure to 10%, 20% or even greater. The finite failure strain of magnesium alloy can only be explained with the additional deformation mechanisms.

From the early experimental results on magnesium single crystal, it is illustrated that the CRSS of prismatic slip of dislocation, see Fig. 2.1(b), is 50-100 times higher than that of basal slip at room temperature (Wonsiewicz and Backofen, 1967). Even at high temperature the difference of CRSS between the two deformation mechanisms are still very high (Flynn et al., 1961). It is generally considered that prismatic slip cannot be significantly activated at ambient temperature (below 225°C), see Roberts (1964). But from experimental results on magnesium polycrystals, Hauser et al. (1958) has observed prismatic slip at grain boundary region because of the mis-orientation between neighbouring grains. The ratio of CRSS between prismatic slip and basal slip is reduced to around 2-2.5 at room temperature, see Agnew and Duygulu (2005). It is necessary to incorporate a significant amount of prismatic slip to explain the observed plastic anisotropy (e.g., r-values) of textured magnesium alloy, see Agnew et al. (2003).

A non-zero shear plane for the deformation perpendicular to the basal plane (parallel to the *c*-axis) is supplied by pyramidal slip $(1\bar{1}22)[\bar{1}\bar{1}23]$, see Fig. 2.1(d). Obara et al. (1973) observed pyramidal slip in the compression test along the *c*-axis and the material show rapid strain hardening. There is outstanding debate regarding the role of $\langle\alpha+c\rangle$ slip. Some view it as a helpful mechanism, which promotes homogeneity in plastic strain accommodation and overall ductility, see Agnew et al. (2003), while others view it as a mechanism of plastic instability and failure based on single crystal tests, see Obara et al. (1973).

2.1.3 Twinning

Twinning is the result of identical motions of atoms in the twinning direction which caused by a homogeneous simple shear of the parent lattice. The crystal structure of the strained part becomes a mirror image of the parent material with respect to the twinning plane (Christian and Mahajan, 1995), see Fig. 2.3(a). When the polished surface of such a material is subjected to etching, usually the regions on both sides of the twin crystals will be attacked differently because of a difference in the atomic configurations. Hence, viewed under a microscope the surface will show dark and bright parallel regions

within each grain, see Fig. 2.3(b).

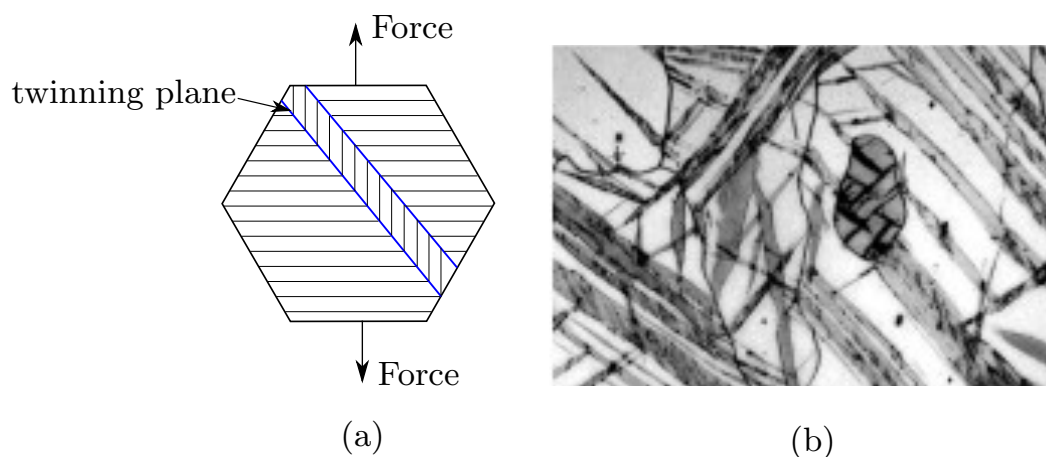


Figure 2.3: (a) Twinning in a hexagonal lattice. The cross hatching lines correspond to basal plane traces and the image zone axis is one of the α axis. (b) Twin boundaries as dark and bright regions within each grain in a magnesium based alloy (Jiang et al., 2007)

Deformation twinning is an important mechanism of plastic strain accommodation in Mg and its alloys. A good explanation for this is the case provided by Kocks and Westlake (1967) who suggested that Mg has 4.5 independent ‘slip’ modes if one considers basal and non-basal slip of α dislocations plus the role of the main $(01\bar{1}2)$ twinning mode. Their description helps one to understand why Mg is not brittle, since it has (according to this construct) nearly five independent slip systems. The limitations of considering twinning as a slip mode help one to understand why Mg does not exhibit such general ductility as more typical engineering materials based upon Fe or Al, see Agnew (2012).

The predominant deformation twinning mechanism in all hcp metals is the $(01\bar{1}2)[0\bar{1}11]$ twin, see Fig. 2.1(e). It is also named as extension twin as it produces extension along the c -axis for magnesium alloys. The normally observed tension-compression asymmetry for wrought magnesium alloys can be explained by the extension twinning mechanism. The so called tension-compression asymmetry is that the material exhibit bigger yield stress in tension than in compression along the in-plane direction. As mentioned before, after the processing routes like rolling or extrusion, the majority of grains are orientated in a direction which the softest slip system basal slip of α dislocation could not be easily activated so that the hard slip systems and twinning should be activated. The extension twin mechanism can only be activated when the crystals are pulled along the c -axis direction or compressed perpendicular to that direction. Due to the initial texture of wrought magnesium alloys, the condition can be satisfied when the materials are compressed in-

plane but not when the materials are stretched which results in a higher yield stress in tension.

Another mechanical twinning can occur on the $(01\bar{1}1)$ planes which is called compression twin. For magnesium sheets with strong basal texture, the compression twin can be activated when through thickness compression are conducted. Because of the high CRSS of this deformation mechanisms, it will substantially limit the formability. Obara et al. (1973) observed an immediately fracture in the compression test along c-axis after compression twinning happened.

2.1.4 Magnesium alloy with rare earth elements

Recently, new magnesium alloys containing rare earth elements tend to exhibit different microstructure, and especially texture, developing during rolling, which has a significant influence on resulting sheet properties. These sheets typically form microstructures with grain sizes between 10-20 μm , but have textures that are significantly weaker compared to those of the conventional sheets. These sheets do not have a high concentration of basal planes parallel to the sheet plane, but exhibit a preferential tilt of the basal planes of $10 - 20^\circ$ to the RD (rolling direction) (Bohlen et al., 2007) or the TD (transverse direction) (Mackenzie and Pegguleryuz, 2008; Wendt et al., 2009). Tensile tests at ambient temperature for ZK61 (Mg-6.63 wt.% Zn-0.56 wt.% Zr) revealed that the failure strain is correlated with the initial texture of magnesium sheets and increases with the weakening of basal texture, see Chen et al. (2012).

2.2 Phenomenological modelling of plastic deformation in metals

Plastic deformation refers to the deformation of a material undergoing permanent changes of shape in response to applied force. The phenomenological model describes the relations based on experimental observations of the macroscopic behaviour and on general principles of mechanics (no individual slip systems are considered). The phenomenological modelling of metal plasticity establishes relations between the mechanical quantities (such as stress, strain, etc.) under a complex stress state that can describe adequately the observed plastic (irreversible) deformation. This chapter presents the theoretical framework for the phenomenological modelling of metal plasticity. The model for the prediction of the material response specifically for wrought magnesium sheets is also introduced in this chapter.

In order to analyse the stress and strain relations in plastic deformation, a

phenomenological theory for plasticity must include three aspects:

- 1) a yield criterion defining the limit of elasticity under any possible combination of stresses;
- 2) A flow rule expressing the relationship between the plastic deformation increments or plastic rate-of-deformation components and the stress components;
- 3) A hardening rule describing the change of the yield criterion with work-hardening.

2.2.1 Yield criterion

The general yield condition is: for a given state of a given material, there is a function f of the stress components σ_{ij} ($i, j = 1, 2, 3$), so that the material is elastic for $f < 0$ and plastic for $f = 0$. Hence the yield condition can generally be expressed as

$$f(\sigma_{ij}, k) = 0, \quad (2.1)$$

where k is a material constant which can be determined by an experiment like the uniaxial tensile test or shear test, see Lubliner (2008).

2.2.1.1 Isotropic yield criterion

For the initial yield in polycrystalline metals when the crystallites have a random orientation, it leads to an apparent isotropy in any sample large enough compared to crystallite dimensions. For isotropic materials, the plastic yielding can depend only on the magnitudes of the three principal stresses, and not on their directions, any yield criterion is expressible in the form

$$f(\sigma_1, \sigma_2, \sigma_3, k) = 0. \quad (2.2)$$

f is a symmetric function of the three principal stresses $\sigma_1, \sigma_2, \sigma_3$ of the stress deviator tensor \mathbf{s} , so that the yield conditions are the same for each directions.

von Mises yield criterion

An important experimental fact for metals, shown by Bridgman (1909), is that yield is independent of the hydrostatic pressure (one third of the average of the three normal stress components of any stress tensor) so that the yield function can be reduced to the function of the second and third invariants of the stress deviator tensor \mathbf{s} ,

$$f(J_2, J_3, k) = 0, \quad (2.3)$$

in which J_2 and J_3 are the second and third invariants of the stress deviator tensor \mathbf{s} which are defined as follows,

$$\begin{aligned}
 J_2 &= \frac{1}{2} \mathbf{s} : \mathbf{s} \\
 &= \frac{1}{2} (s_1^2 + s_2^2 + s_3^2) \\
 &= \frac{1}{6} [(\sigma_{11} - \sigma_{22})^2 + (\sigma_{22} - \sigma_{33})^2 + (\sigma_{33} - \sigma_{11})^2] + \sigma_{12}^2 + \sigma_{23}^2 + \sigma_{31}^2, \quad (2.4) \\
 &= \frac{1}{6} [(\sigma_1 - \sigma_2)^2 + (\sigma_2 - \sigma_3)^2 + (\sigma_3 - \sigma_1)^2] \\
 J_3 &= \det(\mathbf{s}) \\
 &= s_1 s_2 s_3
 \end{aligned}$$

where s_1, s_2, s_3 are the principal values of the stress deviator tensor \mathbf{s} .

The von Mises yield criterion which is dating from 1913 states that a material transfers from an elastic to a plastic state when the second deviatoric stress invariant J_2 reaches a critical value k (Mises, 1913), so this yield criterion is also called the J_2 plasticity. Mathematically the von Mises yield criterion is expressed as:

$$J_2 = k^2, \quad (2.5)$$

where k is the yield stress of the material in pure shear τ_0 . As the definition of von Mises yield criterion, the yield stress in uniaxial tension is $\sqrt{3}$ times of the yield stress in pure shear. Thus, we have:

$$k = \frac{\sigma_0}{\sqrt{3}}. \quad (2.6)$$

The von Mises yield criterion defines the yield surfaces as a circular cylinder, see Fig. 2.4. Its intersection with the deviatoric plane ($\sigma_1 + \sigma_2 + \sigma_3 = 0$) is a circle with radius $\sqrt{2}k$. When the stress state lies on the surface the material is said to have reached its yield point and the material is said to have become plastic.

For isotropic material, the yield criterion must fulfill the following two aspects:

1. Yield for isotropic materials must be independent of the labelling of the axes. Thus f must be a symmetric function of σ_i ($i = 1, 2, 3$).
2. If the yield stresses measured in compression are equal to the yield stresses measured in tension, then f must be an even function of σ_i ($i = 1, 2, 3$). If not, then f must be an odds function of σ_i ($i = 1, 2, 3$).

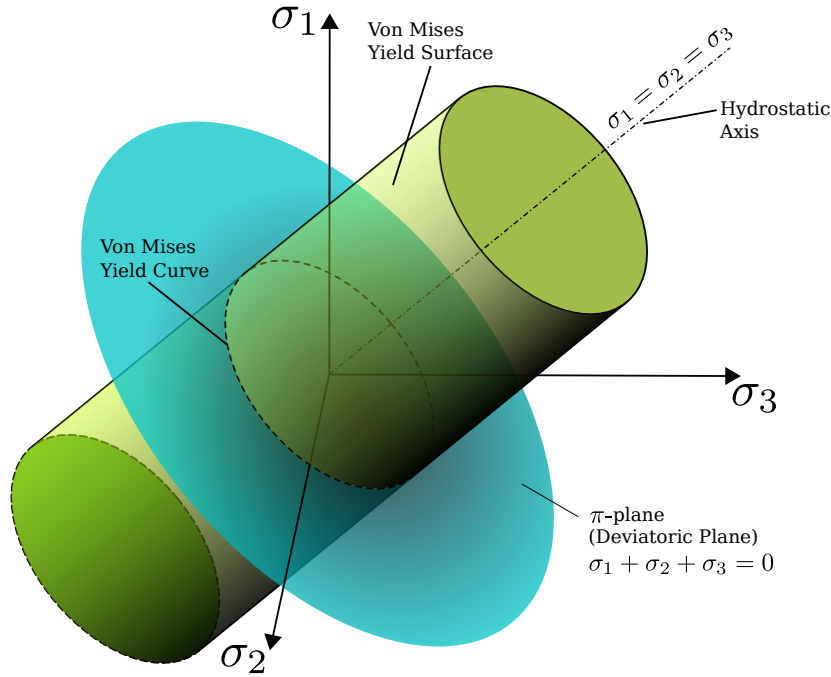


Figure 2.4: The von Mises yield surfaces in principal stress coordinates (Wikipedia)

2.2.1.2 Anisotropic yield criterion

Lankford coefficient

Textured material like metal sheets products shows anisotropic mechanical behaviour. Lankford coefficient (also called r-value) is a strain anisotropy parameter for sheet metals, see Lankford et al. (1950). In a uniaxial tensile or compression test of metal sheets, it is defined as follows,

$$r = \frac{\epsilon_w^p}{\epsilon_t^p}, \quad (2.7)$$

in which, ϵ_w^p and ϵ_t^p are the plastic strain in width direction and thickness direction of the specimen.

As the thickness of the specimen is very small compare to its width, the relative errors of measurement of the two strains will be quite different. Therefore the above relationships are replaced by one implying quantities having the same order of magnitude: length and width of the specimen (Banabic et al., 2000). Considering the assumption that volume of material keeps constant during plastic deformation so that

$$\epsilon_l^p + \epsilon_w^p + \epsilon_t^p = 0, \quad (2.8)$$

in which, ϵ_l^p is the plastic strain in loading direction of the specimen. The

following form of Eq. 2.7 is obtained,

$$r = -\frac{\epsilon_w^p}{\epsilon_l^p + \epsilon_w^p}. \quad (2.9)$$

Hill 1948 yield criterion

The general idea to establish the anisotropic yield criterion is to introduce a large number of anisotropy coefficients, which enable more details of the material anisotropy to be captured at the expense of simplicity.

Hill proposed an anisotropic yield criterion in 1948 (Hill, 1948). It is an extension of the von Mises yield criterion. The yield criterion can describe an anisotropic material with three orthogonal symmetry planes (orthotropic material). The yield criterion is expressed as follows:

$$2f(\sigma_{ij}) = F(\sigma_{11}-\sigma_{22})^2 + G(\sigma_{22}-\sigma_{33})^2 + H(\sigma_{33}-\sigma_{11})^2 + 2L\sigma_{12}^2 + 2M\sigma_{23}^2 + 2N\sigma_{31}^2. \quad (2.10)$$

Here f is the yield function. F , G , H , L , M and N are the constants describing the anisotropy state of the material.

If X , Y , Z are the yield stresses in the principal directions and R , S , T are the yield stress in shear. The value of these constants in the yield criterion can be solved as follows,

$$\begin{aligned} 2F &= \frac{1}{Y^2} + \frac{1}{Z^2} - \frac{1}{X^2} \\ 2G &= \frac{1}{Z^2} + \frac{1}{X^2} - \frac{1}{Y^2} \\ 2H &= \frac{1}{X^2} + \frac{1}{Y^2} - \frac{1}{Z^2} \\ 2L &= \frac{1}{R^2} \\ 2M &= \frac{1}{S^2} \\ 2N &= \frac{1}{T^2} \end{aligned} \quad (2.11)$$

The anisotropy of the material can be described as long as the six yield stresses (X , Y , Z , R , S and T) are available. The Hill 1948 yield criterion has been widely used in practice for the advantage that the criterion needs a small number of mechanical parameters for determining the yield function.

2.2.2 Flow rule

The stress strain relation in the uniaxial tensile test is rather easy to be understood. However, the material flow under a complex stress state is not so straightforward because it requires 5 stress and 5 strain independent components. The flow rule is the theory about how is the stress-strain relationship under any general combined stress state. It gives the ratio of the components of the plastic strain increment tensor $d\epsilon_{ij}^p$ and also the direction of the plastic strain increment vector in the strain space. An elastic, plastic generalisation proposed by Prandtl (1924) for the plane problem, and by Reuss (1930) in general, assumed that

$$d\epsilon_{ij}^p = d\lambda s_{ij}, \quad (2.12)$$

where $d\epsilon_{ij}^p$ is the component of plastic strain increment tensor, $d\lambda$ is a plastic multiplier which can be determined by ensuring the stress state lies on the yield surface during plastic flow. s_{ij} is the component of the stress deviator tensor.

The complete strain increment $d\epsilon_{ij}$ is decomposed into the elastic strain increment $d\epsilon_{ij}^e$ and the plastic strain increment $d\epsilon_{ij}^p$,

$$d\epsilon_{ij} = d\epsilon_{ij}^e + d\epsilon_{ij}^p, \quad (2.13)$$

where the elastic strain increment $d\epsilon_{ij}^e$ is given as follows using Hooke's law,

$$d\epsilon_{ij}^e = \frac{1 + \nu}{E} d\sigma_{ij} - \frac{\nu}{E} d\sigma_{kk} \delta_{ij}, \quad (2.14)$$

where ν is the Lamé elastic constant and δ_{ij} is the Kronecker delta. These expressions are called the Prandtl-Reuss equations.

Mises (1928) proposed the concept of the plastic potential function, which is a scalar function of the stresses, $g(\sigma_{ij})$. Then the plastic flow equations can be written in the form

$$d\epsilon_{ij}^p = d\lambda \frac{\partial g}{\partial \sigma_{ij}}. \quad (2.15)$$

The equation implies that the plastic strain increment vector $d\epsilon^p$ is directed along the normal to the surface of plastic potential.

The simplest case when the yield function and the plastic potential function coincide, $f = g$. Thus, Eq. 2.12 takes the form

$$d\epsilon_{ij}^p = d\lambda \frac{\partial f}{\partial \sigma_{ij}}. \quad (2.16)$$

This is called the associated flow rule because the plastic flow is connected or associated with the yield criterion. The direction of the plastic strain increment vector is normal to the surface of the yield surface so the associated flow rule is also called normality rule. In general, due to very little experimental evidence on plastic potential functions, for engineering materials the associated flow rule is applied predominantly to these materials for practical reasons.

2.2.3 Work hardening

When an initial yield surface is known, the rule of work hardening defines its modification during the process of plastic flow. A number of hardening rules have been proposed. The most widely used rules, isotropic hardening (expansion of the initial yield surface), will be introduced. Distortional hardening which describes the changes of the shape of the yield surface during strain-hardening will also be discussed in this section.

2.2.3.1 Isotropic hardening

The simplest work-hardening rule, isotropic hardening, is based on the assumption that the size of the yield surface expands uniformly without distortion and translation as plastic flow occurs. Two scalar quantities - the effective stress $\bar{\sigma}$ (measuring the size of the yield surface) and the effective plastic strain increment dp are implied to specify the size of the subsequent yield surface and its dependence on the deformation respectively. The most commonly used definition of the effective stress and effective plastic strain in engineering practice, particularly for computational analysis, is based on the von Mises yield criterion, sometimes called von Mises stress and equivalent plastic strain,

$$\bar{\sigma} = \sqrt{\frac{3}{2} \mathbf{s} : \mathbf{s}}. \quad (2.17)$$

In uniaxial stress state, $\bar{\sigma} = |\sigma_{11}|$.

$$dp = \sqrt{\frac{2}{3} d\mathbf{p} : d\mathbf{p}}, \quad (2.18)$$

where the numerical factor has been chosen so that in uniaxial stress state, $dp = dp_{11}$.

Hence the equation for the subsequent yield surface or loading surface can be written in the general form,

$$\bar{\sigma} = F\left(\int dp\right). \quad (2.19)$$

It permits the determination of the function F related with the variable $\int pdp$ in principle by a single tensile test.

2.2.3.2 Distortional hardening

Experimental evidence shows that the yield locus changes its shape during forming processes. Taghvaipourm et al. (1972) observed a big variation of the r-value with the increase of plastic strain in titanium which implies that the corresponding slope of the yield surface is evolving with the plastic deformation. Tozawa (1978); Hill et al. (1994b); Kuwabara et al. (1998) reported a distortion of the proportionality of the hardening curves along different loading radius under biaxial loading in brass, steel and aluminium alloys, respectively. These variations imply the progressive changes of the yield surface's shape. In other words, a variation of the yield criterion is to be expected.

To account for this kind of physical phenomenon, Hill and Hutchinson (1992) introduced the concept of differential hardening in which the radius of the yield locus in polar coordinates is expressed in the form of the power law

$$\tau = k(\theta)y^{n(\theta)}, \quad (2.20)$$

where θ is the polar angle. By selecting appropriate $n(\theta)$ and $k(\theta)$, differential hardening can be realised along different loading paths. The determination of functions $n(\theta)$ and $k(\theta)$ should be based on experimental data which, however, are not easily obtainable.

An alternative method is the so called isotropic distortional hardening, which is to allow model parameters of the yield function to vary during forming processes since the locus of any yield function is uniquely determined by these parameters (such as the r-value and uniaxial tension yield stress, etc.). Ghafari et al. (2014); Steglich et al. (2011); Mekonen et al. (2012) defined the coefficients as functions of an equivalent plastic strain. At the same time, the size of the yield surface can be determined from the uniaxial tensile test like in the isotropic hardening.

Fig. 2.5 shows the contours of constant equivalent plastic strains at 0.02, 0.08 and 0.14 from radial loading paths using the extension of the yield function CPB2004 (Cazacu and Barlat, 2004). The components c_{ij} of the linear transformation tensor \mathbf{L} was defined as a saturating exponential function, see Steglich et al. (2011),

$$c_{ij} = A_{ij} + B_{ij}(1 - e^{-C_{ij}p}), \quad (2.21)$$

where A_{ij} , B_{ij} and C_{ij} are the model parameters. It is noted that Eq. 2.21 depends solely on the plastic equivalent strain as an internal variable. This

limits the application of the constitutive model to monotonic loading paths. Neither load path changes nor load reversals may be described properly. However, for monotonic path it is assured that, through the exponential functions, the material tends towards a steady state behaviour. Fig. 2.5 exhibits the changing of the contours shape with the strain hardening.

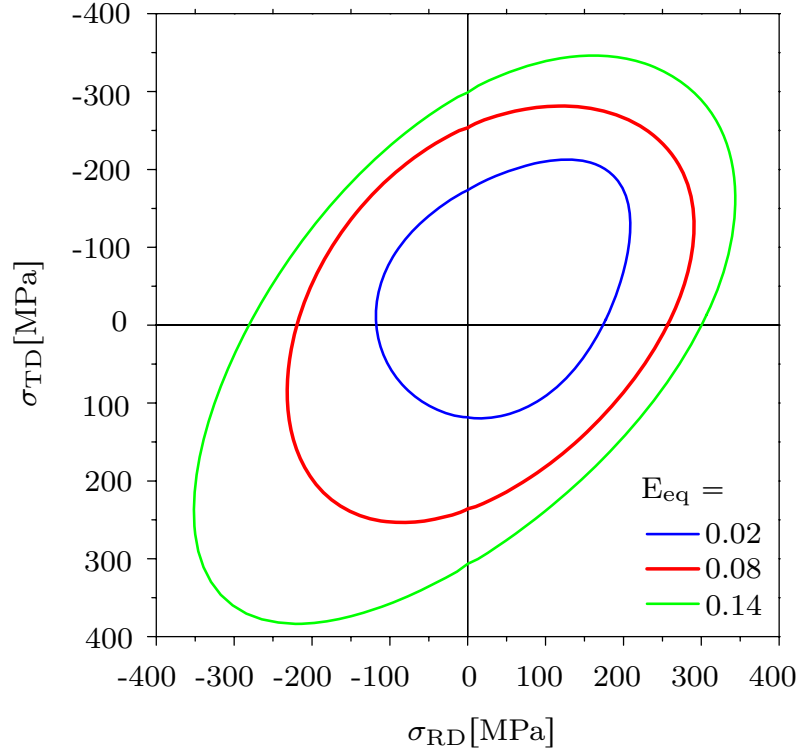


Figure 2.5: Contours of constant equivalent plastic strains of 0.02, 0.08 and 0.14 from radial loading paths using yield function described in Steglich et al. (2011)

2.3 Constitutive model for wrought magnesium sheets

Cazacu-Plunkett-Barlat 2006 yield function

In order to describe both the anisotropy of a material and the yielding asymmetry between tension and compression, a yield function was proposed by Cazacu et al. (2006). It is a hydrostatic pressure insensitivity yield function based on the principal values of the stress deviator. The orthotropic yield criterion is of the form

$$\bar{\sigma} = ((|\Sigma_1| - k \cdot \Sigma_1)^a + (|\Sigma_2| - k \cdot \Sigma_2)^a + (|\Sigma_3| - k \cdot \Sigma_3)^a)^{1/a}, \quad (2.22)$$

where a is the degree of homogeneity and it is considered to be a positive number and is not necessary to be a integer. k is a material constant related to the tension-compression asymmetry of the material. $\Sigma_1, \Sigma_2, \Sigma_3$ are the principal values of the transformed tensor Σ which is defined as

$$\Sigma = \mathbf{C} : \mathbf{S}, \quad (2.23)$$

where \mathbf{S} is the stress deviator and \mathbf{C} is a constant fourth order tensor which should satisfy the major and minor symmetries to describe the orthotropic material. Thus for 3-D stress conditions \mathbf{C} involves 9 independent anisotropy coefficients. In case of a sheet, 1, 2 and 3 represent the rolling (or extruded), transverse, and the normal directions, the tensor \mathbf{C} is represented as

$$\mathbf{C} = \begin{pmatrix} c_{11} & c_{12} & c_{13} & 0 & 0 & 0 \\ c_{12} & c_{22} & c_{23} & 0 & 0 & 0 \\ c_{13} & c_{23} & c_{33} & 0 & 0 & 0 \\ 0 & 0 & 0 & c_{44} & 0 & 0 \\ 0 & 0 & 0 & 0 & c_{55} & 0 \\ 0 & 0 & 0 & 0 & 0 & c_{66} \end{pmatrix}. \quad (2.24)$$

It is worth to notice that in spite that the transformed tensor is not deviatoric, the orthotropic criterion is insensitive to hydrostatic pressure and thus the condition of plastic incompressibility is still satisfied. Furthermore, for k belongs to $[-1,1]$ and any positive numbers $a \geq 1$, this yield function is convex.

Role of parameters

In this section, the role of each parameters is investigated.

The role of a is presented in Fig. 2.6(a). The corners and flats are in evidence with the increase of a . In the case of $a = 2$ and $c_{ij} = 1$ when $i = j$ or 0 when $i \neq j$, the yield function is the same with von Mises yield function.

Fig. 2.6(b) shows the influence of value of k to the ratio of the yield stress in tension and compression. Note that the higher the ratio between the yield stress in tension and compression, the greater is the departure from the von Mises ellipse. When $k = 0.8$, the yield surface represents a triangle with rounded corners.

For the anisotropy coefficients in tensor \mathbf{C} , they allow to distort the isotropic yield surface. No restriction applies to the c_{ij} coefficients, in particular they can be negative. Each parameter modifies a given part of the yield surface as shown in Fig. 2.7.

The yield surface is defined by:

$$\bar{\sigma} - R(p) = 0, \quad (2.25)$$

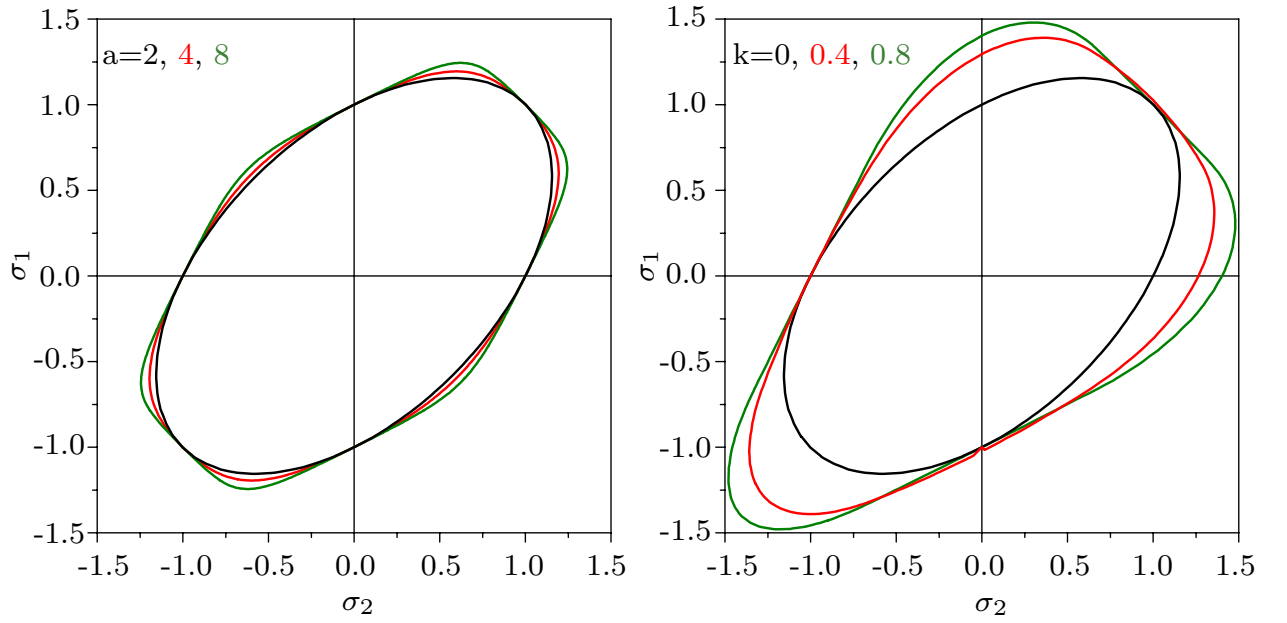


Figure 2.6: Influence of a and k to the shape of the yield surface

where $\bar{\sigma}$ is the yield function, p is the equivalent plastic strain and R is the flow stress. Associated flow rule was adopted for the plastic flow, the direction of the plastic strain rate $\dot{\epsilon}^p$ is perpendicular to the yield surface and is given by

$$\dot{\epsilon}^p = \dot{\lambda} \frac{\partial \bar{\sigma}}{\partial \boldsymbol{\sigma}}, \quad (2.26)$$

where $\dot{\lambda}$ is the plastic multiplier.

The effective strain rate \dot{p} is defined by writing the equivalence of the microscopic and the macroscopic plastic dissipations,

$$\bar{\sigma} \dot{p} = \boldsymbol{\sigma} : \dot{\epsilon}^p = \dot{\lambda} \boldsymbol{\sigma} : \frac{\partial \bar{\sigma}}{\partial \boldsymbol{\sigma}}. \quad (2.27)$$

The formulation of the yield function Eq. 2.22 entails that $\bar{\sigma}$ is a homogeneous function of degree 1. According to the Euler's theorem about homogeneous functions applies,

$$\bar{\sigma} = \boldsymbol{\sigma} : \frac{\partial \bar{\sigma}}{\partial \boldsymbol{\sigma}}, \quad (2.28)$$

which gives directly $\dot{p} = \dot{\lambda}$.

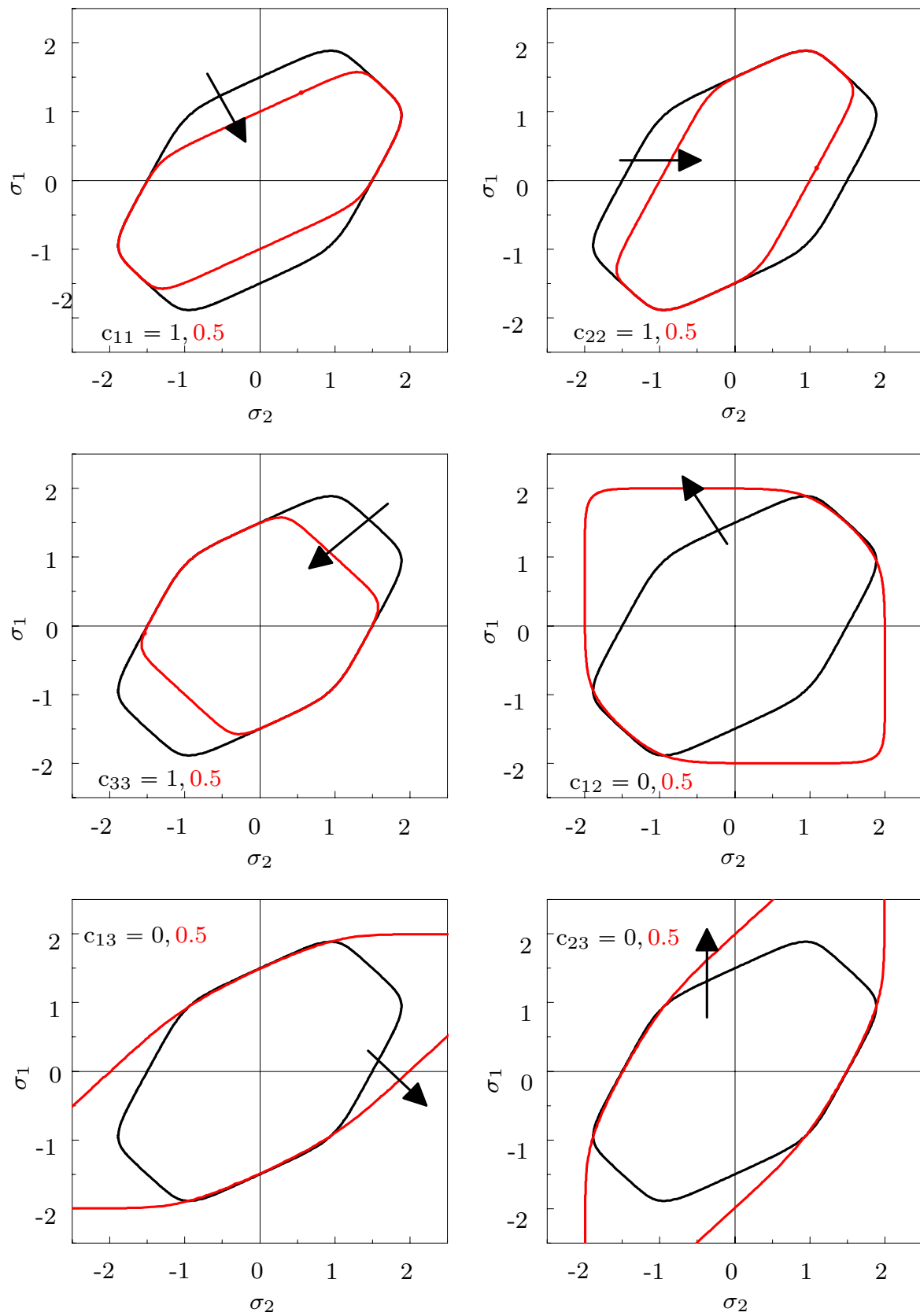


Figure 2.7: Influence of c_{ij} on the shape of the yield surfaces ($a=8$ and the initial value of the C parameters are 0 or 1)

Modified CPB2006 model

In order to account for the evolving plastic anisotropy, the yield function CPB2006 is modified to account for anisotropic hardening with the effective plastic strain. A saturation-type function is used to describe the change in anisotropy parameters. The anisotropy parameters are rewritten in terms of the effective plastic strain as follows,

$$c_{ij} = A_{ij} + B_{ij}(1 - e^{-C_{ij}p}), \quad (2.29)$$

where A_{ij} , B_{ij} , C_{ij} are the model parameters. p is defined as $p = \int \dot{p} dt$.

To capture the tension compression asymmetry, the value k is determined to be evolved respectively in tension and compression and this is achieved by employing the hyperbolic tangent equation,

$$\begin{aligned} k_t &= A_t \tanh(B_t p) + C_t \\ k_c &= A_c \tanh(B_c p) + C_c \\ k &= k_c * (\tanh(\text{tr}(\epsilon^{el}) \times 10^4) + 1) + \\ &\quad k_t * (\tanh(-\text{tr}(\epsilon^{el}) \times 10^4) + 1) \end{aligned} \quad (2.30)$$

, where k_t and k_c are the k function in tension and compression respectively. A_c , B_c , C_c , A_t , B_t , C_t are the model parameters. The trace of elastic strain tensor $\text{tr}(\epsilon^{el})$ is employed to determine the mode between tension and compression during each increment as shown in Fig. 2.8(a) and the illustration of k function Eq. 2.30 is plotted in Fig. 2.8(b). It is shown that the value of k can evolve respectively in tension and compression.

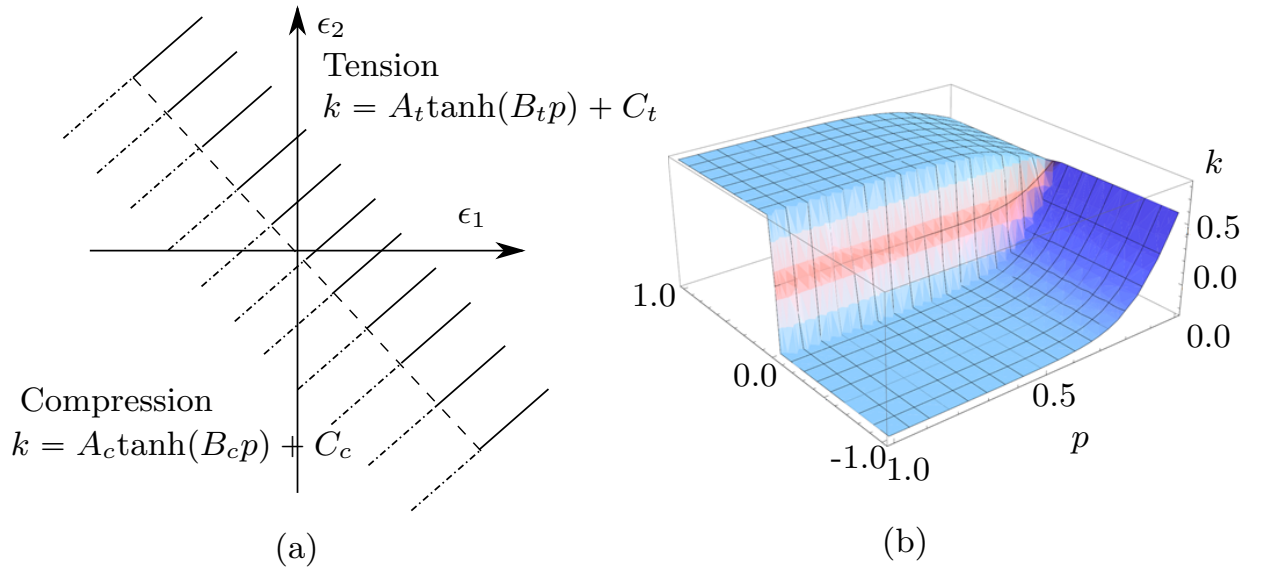


Figure 2.8: (a) Determination of the mode between tension and compression hardening modes; (b) The illustration of k function.

The model was implemented into the Finite Element code ZeBuLoN (Besson et al., 1998), using a θ -method solved by an implicit Newton scheme for the local integration.

2.4 Fitting of the model parameters

In order to calibrate the material parameters of constitutive laws, many authors work on the experimental specimen and experimental equipment design to obtain the shape of the yield surface for anisotropic material.

For the von Mises yield function, only the yield stress in uniaxial tension or shear test is enough to determine the shape of the yield surface. With the development of the yield function for anisotropic material, more and more material parameters are introduced for higher accuracy. For magnesium sheets with strong anisotropy, the mechanical behaviour in each quadrant in the stress space should be investigated.

The yield surface for a plane stress case is illustrated in Fig. 2.9. The black points indicate the particular stress states under which the experiments were performed respectively and the stripes on the loaded squares designate the material orientation. These stress states are uniaxial, biaxial, and pure shear which are comprehensive enough for the material parameter identification.

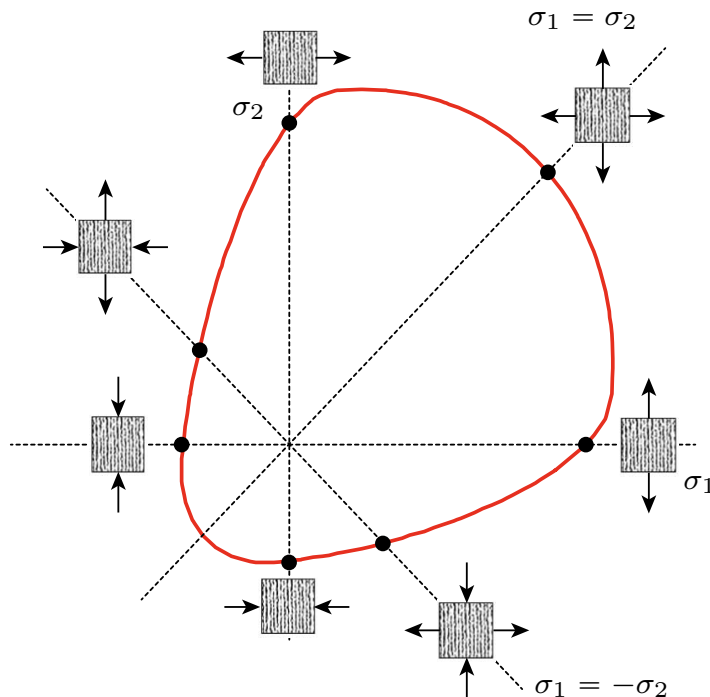


Figure 2.9: Stress states defined in the yield surface

Usually, the material parameter identification is divided into three parts: elastic behaviour, initial yield surface and work hardening model.

As the main research focus of the thesis is the plastic deformation, isotropic elasticity is assumed in the thesis, and the elastic modulus and Poisson's coefficient are determined from the publication.

When the anisotropy evolution is taken into account, the identification of material parameters should consider not only the initial yield surface but also the evaluated yield surface, see Barros et al. (2013). Many anisotropic yield models were proposed to describe the initial anisotropy. The initial anisotropy description coupled with hardening evolution can lead to a good representation of the mechanical behaviour over a large strain range in the most of the previous work, as shown in Zang et al. (2011). In this case, the identification of the material parameters is based on the initial values of the experimental data like yield stress and anisotropic coefficients.

But for the material like magnesium which exhibits the evolved anisotropy behaviour, the material parameters should be identified considering over the temporal evolution of experimental data. Some works investigated the identification of material parameters considering not only the initial values but also values recorded at higher strains (Barros et al., 2013; Wang et al., 2009). Another approach without considering initial yield stress values consists in parameter identification over the temporal evolution of experimental data. Zang et al. (2011) considered a combination of stress level in uniaxial tension, equibiaxial tension and simple shear, both monotonic and Bauschinger tests, to identify material parameters of Bron and Besson yield function. Bron and Besson (2004) also proposed a similar identification strategy with the temporal evolution of stress levels in tensile tests, both on straight and U-notched samples. It can be concluded that due to the dispersion on initial yield stresses, as well as the evolution of anisotropy with strain, considering only initial yield stresses does not give an accurate description of the mechanical behaviour.

3 Mechanical characterisation

In this chapter the mechanical properties of the commercial wrought magnesium alloys AZ31 (Mg + 3%Al + 1%Zn) and the alloy with rare earth element composition ZE10 (Mg + 1%Zn + 0.3%Ce based mischmetal) are investigated by a series of experiments under different loadings. The aims of these comprehensive experiments are generally two points: to get a better understanding of the anisotropic behaviour of wrought magnesium sheets (the relation between the texture and the mechanical properties), to collect the experimental data (stress, strain) for the constitutive material model parameters identification.

Two sets of experiments were conducted: the experiments having only homogeneous states which include uniaxial in-plane tensile test, uniaxial in-plane compression test (using layered sheets) and through thickness compression test (equal to equi-biaxial tensile test); the experiments having inhomogeneous stress states which include the U-notched bar tensile test (biaxial tension stress state dominant) and shear test (shear stress state dominant). Among them, the non-standard testing methods like uniaxial in-plane compression test and through thickness compression test were validated by comparing the generated results with data from a well established method and from the publication, respectively. The work in this chapter is published in Steglich et al. (2014).

3.1 Materials under investigation

Rolled sheets and extruded products of two different magnesium alloys: AZ31 (Mg + 3%Al + 1%Zn based mischmetal) and ZE10 (Mg + 1%Zn + 0.3%Ce based mischmetal) were studied in the research. AZ31 is a widely applied alloy. The traditional wrought alloy which based on the Mg-Al-Zn system has an inclination to generate a strong basal-type texture in the recrystallisation during sheet rolling process. This basal-type texture means the most grains have their c-axes in the sheet normal direction (ND). It limits the formability of the sheets because it constrains the activity of α type dislocation slip, especially under loading in the ND. ZE10 is a developed magnesium alloy with weak basal type texture which benefits from the included rare earth element (Senn and Agnew, 2006). ZE10 shows improved formability because that α dislocation will contribute more to accommodating the deformation (Mishra et al., 2008).

The rolled sheets of the two alloys with a thickness of 2 mm were received in an annealed condition (O - temper). Both of them were made by the former Salzgitter Magnesium Technology SZMT of Germany. Fig. 3.1 is the micrographs and pole figures of the two rolled sheets (?). Fully recrystallised

microstructures with an average grain size of $15\ \mu\text{m}$ for both alloys are observed. For AZ31, the grains are equi-axed whereas for ZE10 the grains show a preferential elongation along the rolling direction (RD) which indicates that the recrystallisation is delayed during the rolling process of this alloy. These differences in the grain structure itself will not influence significantly the mechanical behaviour. The recalculated (0001) basal pole and (01 $\bar{1}$ 0) prismatic pole figures of the two sheets are obtained from x-ray measurements of six incomplete pole figures in an analytical X'Pert Pro x-ray diffractometer with a goniometer setup. An open source code MTEX (Bachmann et al., 2010) has been applied to calculate the orientation distribution function and re-calculate full pole figures. The (0001) basal pole figure of the ZE10 has a maximum intensity of 3.4 which is much weaker than that of the AZ31 having the value of 14. The pole figures of the AZ31 sheet show that most grains have their basal planes aligned in the sheet plane, which corresponds with the strong basal-type texture. Another important feature of AZ31 sheet is that there is a broader intensity spread of basal poles from ND toward the RD than between ND and TD (transverse direction). This type of texture has often been found for rolled or rather tempered magnesium alloy sheets. The (0001) pole figure of ZE10 sheet does not show the strong basal-type texture like AZ31 sheet. It shows a significantly weaker texture and there is a broader intensity spread of basal poles from ND toward TD which is just in the opposite of AZ31.

In order to investigate the influence of processing method on the microstructures and mechanical properties of the two alloys, extruded products of the two alloys are also produced. Slabs of AZ31 and ZE10 were made by gravity casting and then homogenised at 350°C for 15 hours before the extrusion which were performed at 300°C . The produced profiles are hollow rectangular profiles that consist of four plane rectangular cross sections with a thickness of 1.7 mm. The outer-dimension of the profile is $50\text{mm}\times 50\text{mm}$. The sheet-like profile was also analysed as the rolled sheets. It shows different results compared with rolled sheets. Both of extruded AZ31 and ZE10 reveal an almost fully recrystallised grain structure. The grains show longer axis along the ED for both materials. The average grain size of the two alloys are different. For AZ31 the average grain size is $11\ \mu\text{m}$ while it is coarser for ZE10 which reveals an average grain size of $15\ \mu\text{m}$. ZE10 does not show weaker texture like in rolled sheet (?), see Fig. 3.1(b). Both AZ31 and ZE10 show the so-called strong basal-type texture. AZ31 appears broader intensity distribution of the basal pole between ND and TD but not between ND and RD like the rolled sheets.

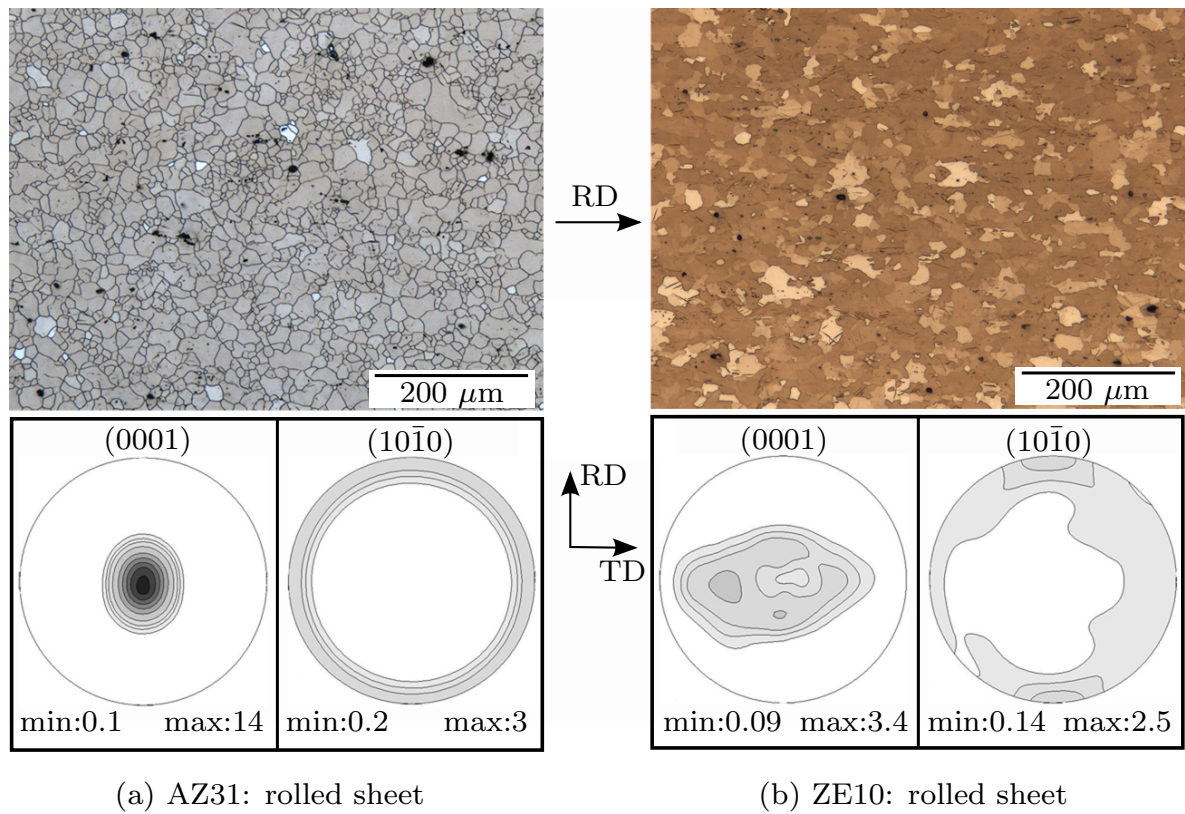


Figure 3.1: Microstructure and texture of rolled sheets of alloys a) AZ31 and b) ZE10

3.2 Experimental setup

In order to investigate the plastic anisotropy of the wrought magnesium sheets, a series of tests will be conducted along different directions. Table. 3.1 exhibits all the tests performed for every material.

3.2.1 Tensile tests

Two sets of tensile tests were performed. Macro-tensile tests which are the standard uniaxial tensile tests were done for rolled material. Micro-tensile tests were made for extruded material with a miniaturised flat tensile specimen because the size of the extruded products along the transverse direction is not enough for the standard tensile specimen.

Macro-tensile tests

Quasi-static uniaxial tensile tests were performed at room temperature at the strain rate of 0.001/s with a universal testing setup Zwick Z050. Flat dog bone

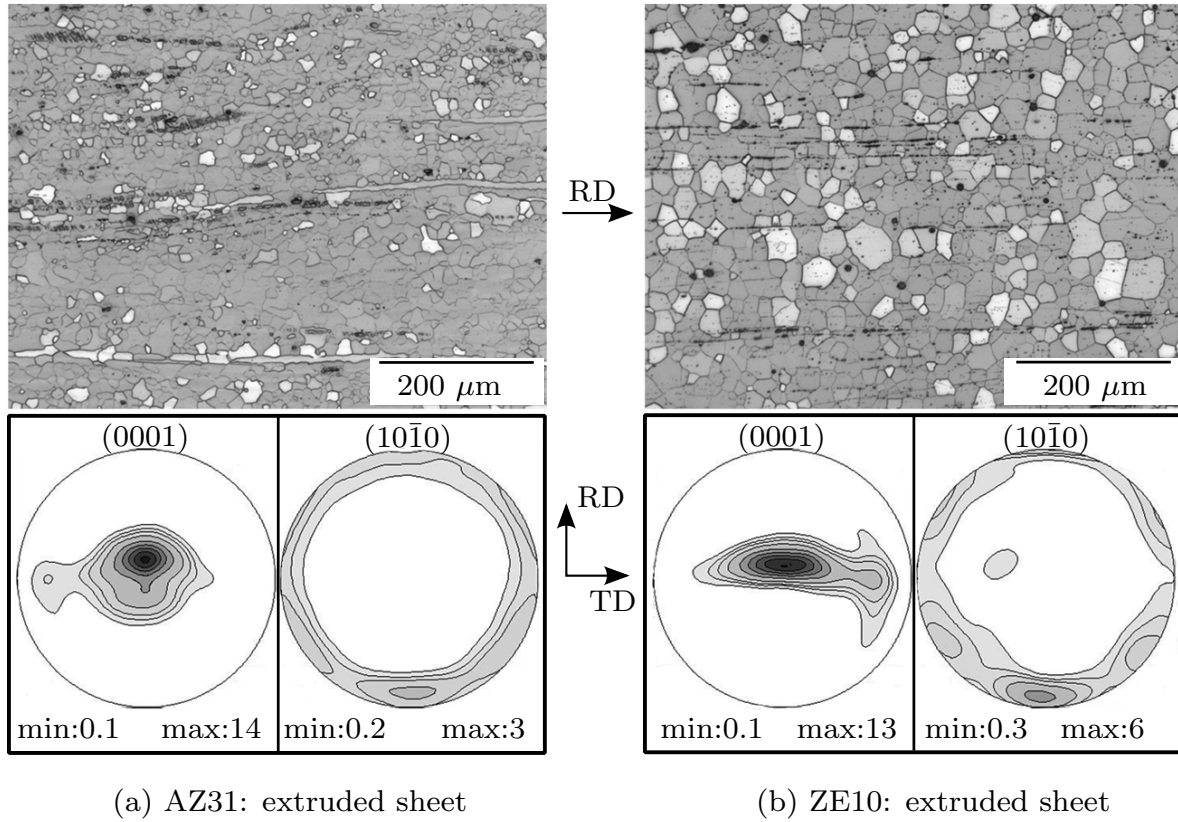


Figure 3.2: Microstructure and texture of extruded sheets of alloys a) AZ31 and b) ZE10

shaped specimens with parallel length of 75 mm and width of 12.5 mm were used. The experiments used two sets of extensometers. One used to measure the strain along the loading direction and the gauge length is 60 mm. Another used for the strain along the width direction to calculate the r-value. The specimens were fabricated along rolling direction (RD) and transverse (TD) direction for rolled sheets to investigate the anisotropy of magnesium sheets. However, for extruded products, the specimens were only fabricated along extruded direction (ED) because the width of the extruded products is only 50 mm which is not enough to produce the standard tensile test specimens. The mechanical properties along the transverse direction of the extruded products were investigated using miniaturised flat tensile specimen and introduced in the next section. For each direction at least three tests were performed to reveal the standard deviations of mechanical properties.

The (cumulative) r-value (Lankford coefficient) was calculated using the relation

$$r = -\frac{\varepsilon_w^{pl}}{\varepsilon_l^{pl} + \varepsilon_w^{pl}}, \quad (3.1)$$

Table 3.1: The experimental arrangements

Alloy	Ori.	UTT	UCT	TTC	UNB	SH
AZ31	Rolled-RD	✓	✓	✓	✓	✓
	Rolled-TD	✓	✓	✓	✓	✓
ZE10	Rolled-RD	✓	✓	✓	✓	✓
	Rolled-TD	✓	✓	✓	✓	✓
AZ31	Extruded-ED	✓	✓	✓	-	-
	Extruded-TD	✓	✓	✓	-	-
ZE10	Extruded-ED	✓	✓	✓	-	-
	Extruded-TD	✓	✓	✓	-	-

The experimental arrangements for all the materials: UTT-Uniaxial tensile tests, UCT-Uniaxial compression tests, TTC-Through thickness compression tests, UNB-U notched bar tests, SH-shear tests

where $\varepsilon_w^{\text{pl}}$ and $\varepsilon_l^{\text{pl}}$ are the logarithmic plastic strains in the width and longitudinal direction, respectively. These two plastic strain components were calculated by subtracting the elastic strain from the respective total strain

$$\begin{aligned}\varepsilon_w^{\text{pl}} &= \varepsilon_w + \nu \frac{\sigma}{E}; \\ \varepsilon_l^{\text{pl}} &= \varepsilon_l - \frac{\sigma}{E},\end{aligned}\tag{3.2}$$

where ε_w and ε_l are the true (logarithmic) strains in the width direction and longitudinal direction, σ is true stress, E is Young's modulus and ν is Poisson's ratio. For E and ν the values of 43 GPa and 0.3 were used.

Micro-tensile tests

To evaluate the tensile behaviour of extruded products, tensile tests were performed with a miniaturised flat tensile specimen (1.7 mm in thickness, 3 mm in width) which has been introduced by Çam et al. (1998). The sample dimension is shown in Fig. 3.3(c). A Zwick Z010 TN testing frame was used. The deformation was monitored by a laser speckle extensometer (Zwick laserXtens). The specimen is illuminated with the laser light (Fig. 3.3(a)). This generates a speckle pattern on the surface of the test specimen (Fig. 3.3(b)). The two green squares on the left and right are for the strain measurement along loading direction and the two green squares on the top and bottom are for the strain measurement along the width direction. The laserXtens software tracks this virtual measuring mark in consecutive images taken during the test. This procedure is called speckle tracking. The specimens were machined along both, extrusion direction and transverse direction, so that this testing results can be evaluated by comparing the experimental results along extruded direction with that of macro-tensile tests.

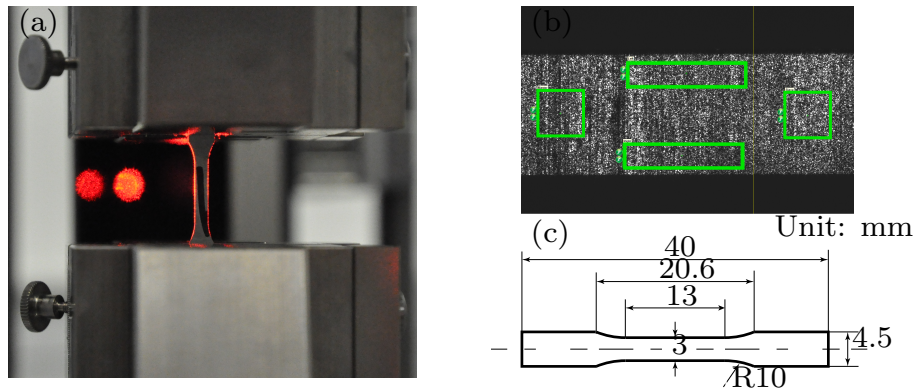


Figure 3.3: Strain measurement using laser extensometer: (a) experimental setup of micro-tensile test; (b) analysis window for determination of the strain along the loading direction and the transverse direction; (c) the dimension of the specimen.

3.2.2 Uniaxial compression tests

The uniaxial in-plane compression test of metal sheets is still a challenge because buckling happens easily to prevent uniform uniaxial deformation. There are generally two methods to ensure uniform deformation in the experiments. One is to apply the anti-buckling facilities on the surfaces of the specimen. Boger et al. (2005) applied two flat steel plates to provide side force to support the modified dog-bone specimen. Lou et al. (2007) extended this method to perform cyclic tension-compression experiments. Kuwabara et al. (1995) designed and developed the comb-type dies for the continuous in-plane stress reversal tests to the specimens. The comb-type dies used for preventing the buckling.

Another method is to minimise the length to thickness ratio of the specimen. Tozawa (1978) carried out the biaxial compression tests (including in-plane uniaxial compression test) using a rectangular specimen prepared by stacking and gluing metal sheets. Khan et al. (2011) prepared the compression specimens by bonding (using J-B Weld adhesive) two sheets with the specimen dimensions of 12.7 mm length and 4 mm thickness. Ghaffari et al. (2014) have conducted the uniaxial compression tests using the adhesively stacked 8 mm cubic sample successfully for magnesium.

In this work, the glued cubes were used for the uniaxial in-plane compression tests. In order to validate this testing method, the experimental results using the facility designed by Kuwabara et al. (1995) was used to compare with the respective experimental data.

For rolled sheets, the cubic specimens glued with five pieces of magnesium

sheets were prepared for the tests, see Fig. 3.4(a). The specimens were

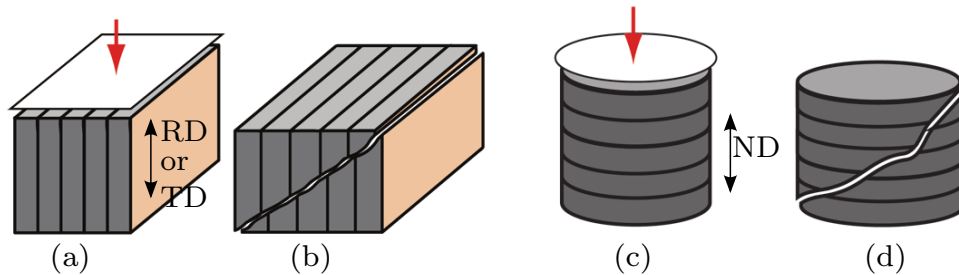


Figure 3.4: Compression test specimens used in this investigation: initial (a) and fractured specimen (b) for in-plane loading; initial (c) and fractured specimen (d) for through-thickness compression

machined along RD and TD. Before applying the J-B-Weld[®] adhesive, the surfaces of the metal sheets were roughened using an abrasive tool mounted on a milling machine and then cleaned using acetone to improve the performance of the adhesive. Pressure was applied on the specimen to squeeze out the excess glue before drying and the thickness of the specimen is slightly above 10 mm. In order to decrease the effect of the misalignment of the compression plates, the machining of the specimens should ensure that the two surfaces on which the compression force will be applied should be exactly parallel to each other and perpendicular to the other surfaces. The two surfaces were also mirror polished and Teflon spray was applied to decrease the friction. The machine used for the compression tests is the Schenck servo-hydraulic 1000 KN machine. The compression displacement control was applied and the force was recorded by the load cell. The same with the tensile tests, two sets of mechanical extensometers were used to measure the deformation history, see Fig.3.5. The displacement along the compression direction was recorded using two extensometers and the average of them were adopted for the following analyse. The third extensometer was used for the measurement of the width change. The experiments were stopped when cracks occurred. In order to check the repeatability of the testing method, three tests were conducted along each direction for each material.

For extruded sheets, the experimental setup is the same with that of the rolled sheets but the cubic specimens are glued with six pieces of magnesium sheets in order to maintain the similar length to thickness ratio, because the thickness of extruded sheets is 1.7 mm.

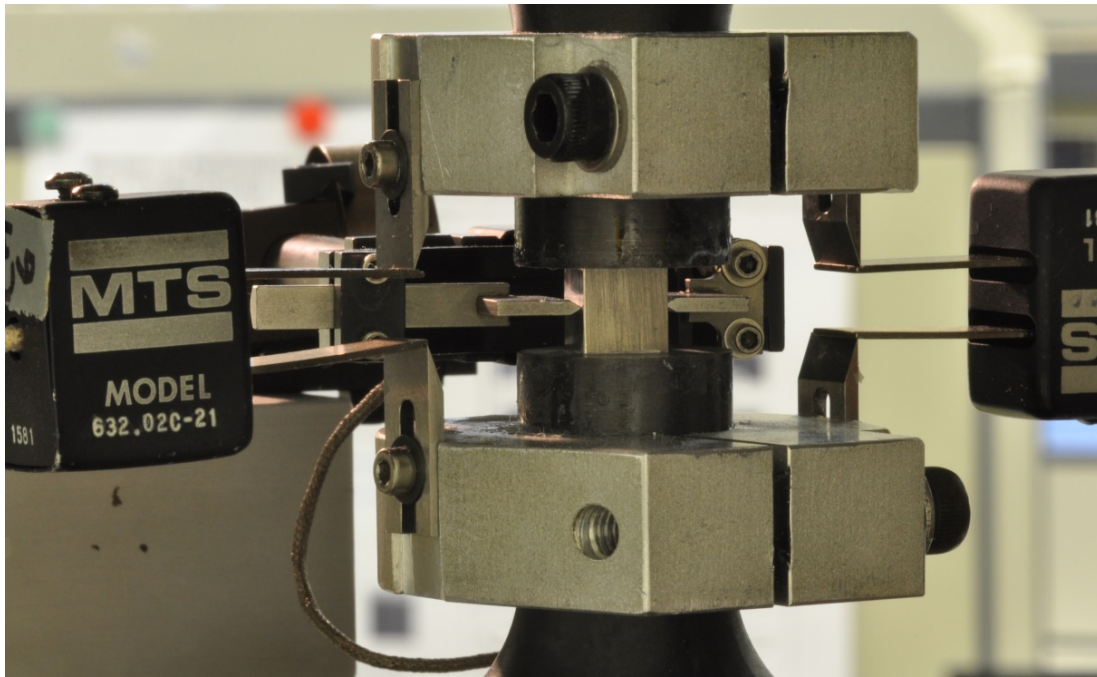


Figure 3.5: Setup for uniaxial compression testing using cube specimens (mounted in the middle)

3.2.3 Through thickness compression tests

The study of material behaviour under biaxial loading has been an meaningful topic for decades, because multi-axial stress states exist in the forming process or on the structure components. The distortional (or differential hardening) hardening was evidenced in the experimental findings reported by (Stout et al., 1983; Hill et al., 1994a; Andar et al., 2012) in the first quadrant of the stress space. However, multi-axial loading experiments are not so straightforward like uniaxial tensile test. The testing facilities and the geometry of the specimen always involve a lot of controversy. Among the variety of experimental methods for biaxial tensile test, the hydraulic bulge test and the biaxial tension tests using cruciform specimens are already well established. The hydraulic bulging test is wildly used to achieve larger plastic strains, see Mellor and Parmar (1978). The improvements of the biaxial extensometer (Johnson and Duncan, 1965) and automated hydraulic bulge testers (Young et al., 1981) simplified the experimental procedure. For the biaxial tensile test using cruciform specimens, different shapes of the specimen were designed by (Shiratori and Ikegami, 1968; Makinde et al., 1992; Boehler et al., 1994; Kuwabara et al., 1998) to create the specimen with a uniform deformation in the gauge section. Steglich et al. (2012) performed equi-biaxial tests using cruciform specimens and hydraulic bulge test with magnesium sheet alloy AZ31 with 1 mm thick-

ness. The experimental data from these two methods show consistent results.

Considering the assumption that the plastic yielding is independent of the hydrostatic pressure, through thickness compression of a sheet is equivalent to the balanced biaxial tension. Barlat et al. (2003) applied the through thickness compression test on a single circular sheet to obtain the experimental data of balanced biaxial tension stress state. The tests were stopped in between to release the elastic deformation and measure the diameter of the deformed specimen. Merklein and Kuppert (2009) used the layered circular sheets to conduct the continued through thickness compression tests revealing a continuous stress-strain curve.

In this work, through thickness compression tests were conducted to collect the experimental data for the balanced biaxial stress states.

Five pieces of circular magnesium sheets with diameter of 20 mm were stacked and glued as described previously, see Fig.3.4(c). A SCHENCK servo-hydraulic 1000 kN universal testing machine was used. The initial strain rate is 10^{-2} /s. The compression displacement control was applied along the thickness direction. The relative deformation between the top and bottom surface was recorded by two MTS extensometers. The average of the two extensometers records were used for the calculation of the strain. The force F was measured by the load cell. The biaxial stress σ_b and the thickness strain ϵ_t was calculated from the following equations.

$$\begin{aligned}\sigma_b &= \frac{4F}{\pi d_0^2} \left(1 - \frac{u}{t_0}\right); \\ \epsilon_t &= \ln\left(1 - \frac{u}{t_0}\right),\end{aligned}\tag{3.3}$$

where t_0 is the initial thickness of the stack and d_0 is initial diameter. It is assumed that the deformation along the in-plane direction is isotropic. When these experimental data are used for the model parameter identification, the scalar character of the stress signal should be considered.

In order to validate this experimental method, additional through thickness compression tests using the same magnesium sheet with the material used in Steglich et al. (2012) were performed to compare the respective experimental results. Five pieces of magnesium ‘‘coins’’ with 1 mm thickness were glued to stacks of 5 mm height, to keep the same aspect ratio of the specimens described above.

3.2.4 U-notched bar tensile test

Tensile tests on U-notched specimens were used for the investigation of the mechanical behaviour of rolled magnesium sheets at high stress triaxility in

this work. The stress triaxiality η is defined in the followed equation,

$$\eta = \frac{\sigma_m}{\bar{\sigma}}; \sigma_m = \frac{1}{3}(\sigma_1 + \sigma_2 + \sigma_3); \bar{\sigma} = \frac{1}{2}[(\sigma_1 - \sigma_2)^2 + (\sigma_2 - \sigma_3)^2 + (\sigma_3 - \sigma_1)^2]^{\frac{1}{2}}, \quad (3.4)$$

in which $\sigma_1, \sigma_2, \sigma_3$ are the principal stresses. The nominal stress triaxiality value can be varied by different radii of the U shape notch. In most cases, the tests are for the research on the damage behaviour of material, see (Brunig et al., 2008; Bonora et al., 2005). Bridgman (1952) calculated the distribution of the triaxiality in a pre-necked tensile test specimen analytically. Hancock and Mackenzie (1976); Earl and Brown (1976) applied this analytical method to a pre-notched specimen to correlate the triaxiality and failure strain.

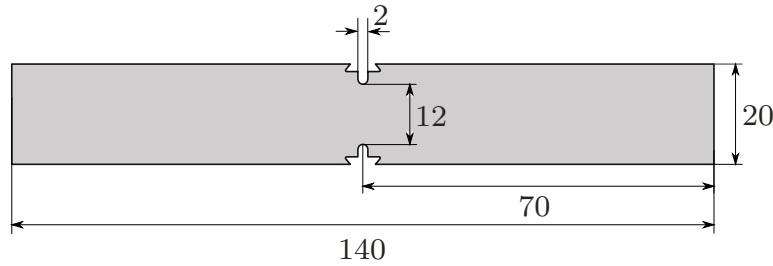


Figure 3.6: The dimension of the U-notched bar specimen

The U-notched bar specimens with notch radius of 2 mm were used. The shape and the dimension of the specimen can be seen in Fig.3.6. The specimens were processed along TD and RD. The experiments were carried out on a Zwick servo hydraulic testing machine with a capacity of 200 kN and the speed of the cross head is constant 0.5 mm/min. The force was recorded by the load cell, and additionally the notch opening displacement (NOD) was measured by two MTC mechanical extensometers on both notches to obtain the displacement close to the deformation zone. The average of the two NOD was used as the unique displacement signal for each test. Three specimens were tested for each direction and each alloy to check the reproducibility of the measurement.

3.2.5 Shear tests

In the previously described tests the stress states are primarily governed by normal stresses. Shear stresses (considering a coordinate system collinear with the axes of orthotropy) are relatively small and confined in small regions of the U-notched samples. Hence, the experimental database for parameter calibration should include tests in which significant shear stresses are present. Frequently shear testing is driven by the possibility of achieving plastic strains

several magnitudes higher than the strain obtained before onset of diffuse necking in an uniaxial tensile test. Simple shear tests conducted for the material AZ31, however, revealed that failure appears at similar levels of effective plastic strain compared to tensile tests, which is confirmed by Khan et al. (2011). Consequently, the purpose of including a shear test in this experimental program is that the tests provide stress and strain fields that are not explored in other experiments as well as it facilitates a validation of the modelling concept.

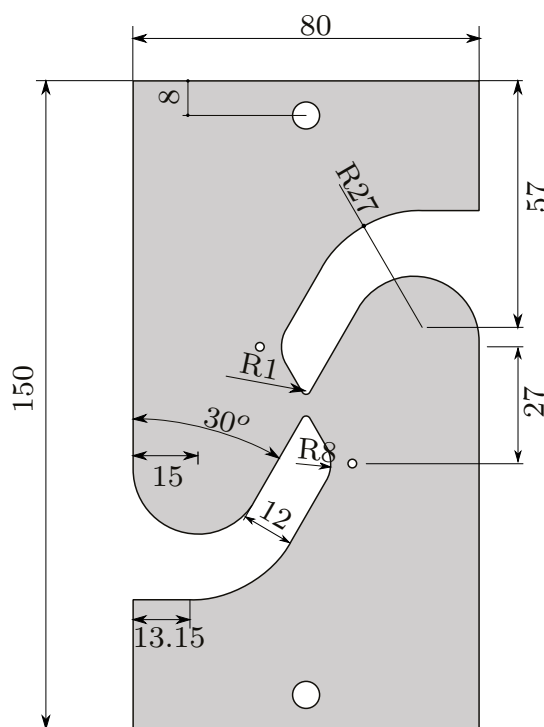


Figure 3.7: The dimension of the shear specimen

In order to impose a shear-dominated stress state, several designs for specimens were proposed depending on the intended use of the test and the material considered. Commonly, the ASTM standard B831-14 (2014) is used for plate material. Once thinner sheets are considered, buckling may easily occur and the test is hence not suitable. Bao and Wierzbicki (2004) stated that in a pure shear test the mean stress is zero or very small compared to the equivalent stress at locations of crack formation. They also presented a new concept for a shear test specimen with a butterfly gauge section and a groove with reduced thickness in the shear zone. However, the reduced thickness in the shear zone requires machining of the plate material which may introduce surface effects such as residual stresses and micro-cracks, and the machining will also vary the initial texture of magnesium sheets. Another design more suitable for testing of magnesium sheets was proposed by Reyes et al. (2009). This setup

avoids the geometrical instability while generating a small and concentrated shear zone. The specimen is sketched in Fig. 3.7. Three specimens oriented along the longitudinal and transverse direction were tested with a constant cross head speed of 0.5 mm/min. The force was measured by a load cell. In order to monitor the global deformation, the displacement in longitudinal direction of two pins attached to the specimen was recorded using a laser extensometer.

3.3 Mechanical responses

3.3.1 Uniaxial tensile tests

Macro-tensile tests

Flow curves and r-values of the materials under investigation relating true strains AZ31 and ZE10 tested in the two selected loading directions (RD and TD) are shown in Fig. 3.8. Both sheets exhibit in-plane anisotropy in the yield stress, which was also observed in earlier work of Yi et al. (2010). The flow curves obtained for the alloy ZE10 show higher yield stresses in the RD than in the TD. In the opposite, the same tests on AZ31 reveal higher yield stresses along the TD. Between the two alloys, AZ31 generally shows a higher stress level for both variants, rolled and extruded products. The ductility of ZE10 in the TD is much higher compared to the RD and the failure strain reaches 35%.

Considering the initial texture, the angular distribution of basal planes of the AZ31 sheet between the normal direction and the RD is broader compared to the one between the ND and the TD, see Fig. 3.1, so that the activation of basal slip is favoured if the uniaxial stress is applied along RD rather than along TD. This results in the mechanical anisotropy of higher yield stress along TD than RD. This is on the contrary for ZE10 because the angular distribution of basal planes is broader along TD. Moreover, ZE10 shows a less strong basal texture which means the alignment of basal planes is more random in the sheet plane. The unfavourable orientation for the activation of basal slip in the sheet plane is not distinct anymore which causes the reduced yield stress in tension compared with AZ31.

For extruded products, both materials exhibit the typical convex curve like it was also found in the tests of the rolled sheets. One difference is that the fracture strains of extruded sheets are lower than that of rolled material, see also Table 3.2.

The r-value was determined from the specimen's width change up to the maximum force. Fig. 3.8 shows considerable evolution of the plastic anisotropy

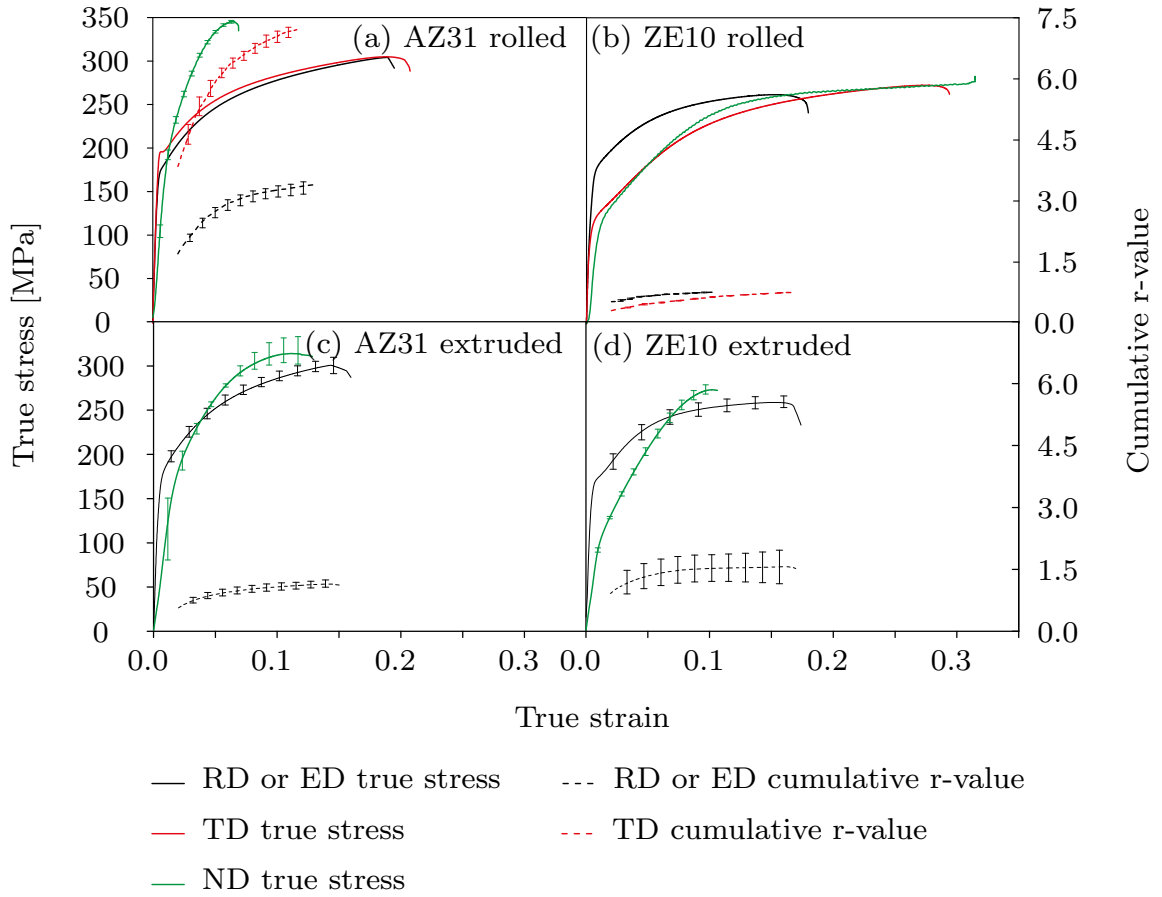


Figure 3.8: Experimental results of the macro-tensile tests: (a) AZ31 rolled sheets (b) ZE10 rolled sheets (c) AZ31 extruded sheets (d) ZE10 extruded sheets

(r-values). This evolution has been related to a transition from basal slip to non-basal slip (Avery et al., 1965; Agnew, 2014). It is noted that the r-value of AZ31 rolled sheets is significantly higher than that of ZE10 rolled sheets. The respective differences in r-value between the RD and the TD are also remarkable. While the r-value of AZ31 rolled sheets reaches 7.1 at maximum load, its respective counterpart in case of ZE10 rolled sheets is 0.76.

For instantaneous r-values, of more relevance to plastic yield function forms via the normality rule, the strain increments are computed in the vicinity of the current strain. The instantaneous r-value is defined as follows,

$$r' = \frac{d\epsilon_w^{pl}}{d\epsilon_t^{pl}}, \quad (3.5)$$

where ϵ_w^{pl} and ϵ_t^{pl} are the plastic strain increments in width direction and thickness direction. Once the normality rule is used for computing the strain increments from the yield function, Eq. 3.5 gives the normal to the yield

Table 3.2: Mechanical properties of the magnesium sheets

Alloy	Variant	Av. grain size [μm]	TYS [MPa]	CTC [MPa]	SD	UTS [MPa]	Fracture strain [%]
AZ31	Rolled-RD	15(1)	170(1)	72(2)	2.36	254(1)	22.2(1.5)
	Rolled-TD		194(1)	77(2)	2.52	257(1)	22.6(0.5)
ZE10	Rolled-RD	15(1)	157(1)	104(2)	1.51	229(1)	21.7(0.1)
	Rolled-TD		107(1)	92(1)	1.16	216(1)	32.2(1.6)
AZ31	Extruded-ED	11(1)	152(11)	93(2)	1.78	261(5)	19.9(1.5)
	Extruded-TD		163(7)	90(1)	1.81	256(1)	19.1(1.6)
ZE10	Extruded-ED	15(1)	134(5)	65(1)	2.06	221(1)	27.8(0.8)
	Extruded-TD		82(16)	57(2)	1.44	208(2)	18.2(1.5)

Tensile and compression tests along rolling direction (RD) and transverse direction (TD) of sheets and along extrusion direction (ED) and perpendicular transverse direction (TD) of extrudates; TYS: tensile yield stress, CYS: compressive yield stress, SD: strength differential TYS/CYS, UTS: ultimate tensile strength; standard deviation in brackets

surface. The dependence of plastic width and thickness strain was fitted by cubic function and their first derivatives are shown as instantaneous r-values in Fig. 3.9.

Micro-tensile tests

The true stress strain curves of extruded AZ31 along ED obtained from the micro-tensile tests are compared with that of macro-tensile tests, see Fig. 3.10. Two experimental results coincide with each other and the three curves from micro-tensile tests show very good reproducibility.

The stress along ED is higher than that of TD for both extruded AZ31 and ZE10, see Fig. 3.11. This is consistent with the initial texture for each material. The angular distributions of basal planes of the extruded AZ31 and ZE10 between the ND and ED are broader compared to the one between the ND and the TD, see Fig. 3.2.

The failure strain for ZE10 along ED is higher than that of TD. For the strain measurements along the width direction, the recorded results for each variant show great differences so that the obtained results could not be used for the analyse of the material strain anisotropy behaviour. This could be explained in two aspects: firstly, the ratio of the width and thickness of the specimen is 1.76 so that the material exhibits bulk material but not sheet metal behaviour, while the r-value is the strain anisotropy measurement for sheet metal; Secondly, considering the grain size of the extruded material, there are around 200 grains along the width direction which is considered to be insufficient for magnesium with hcp structure to exhibit homogeneous

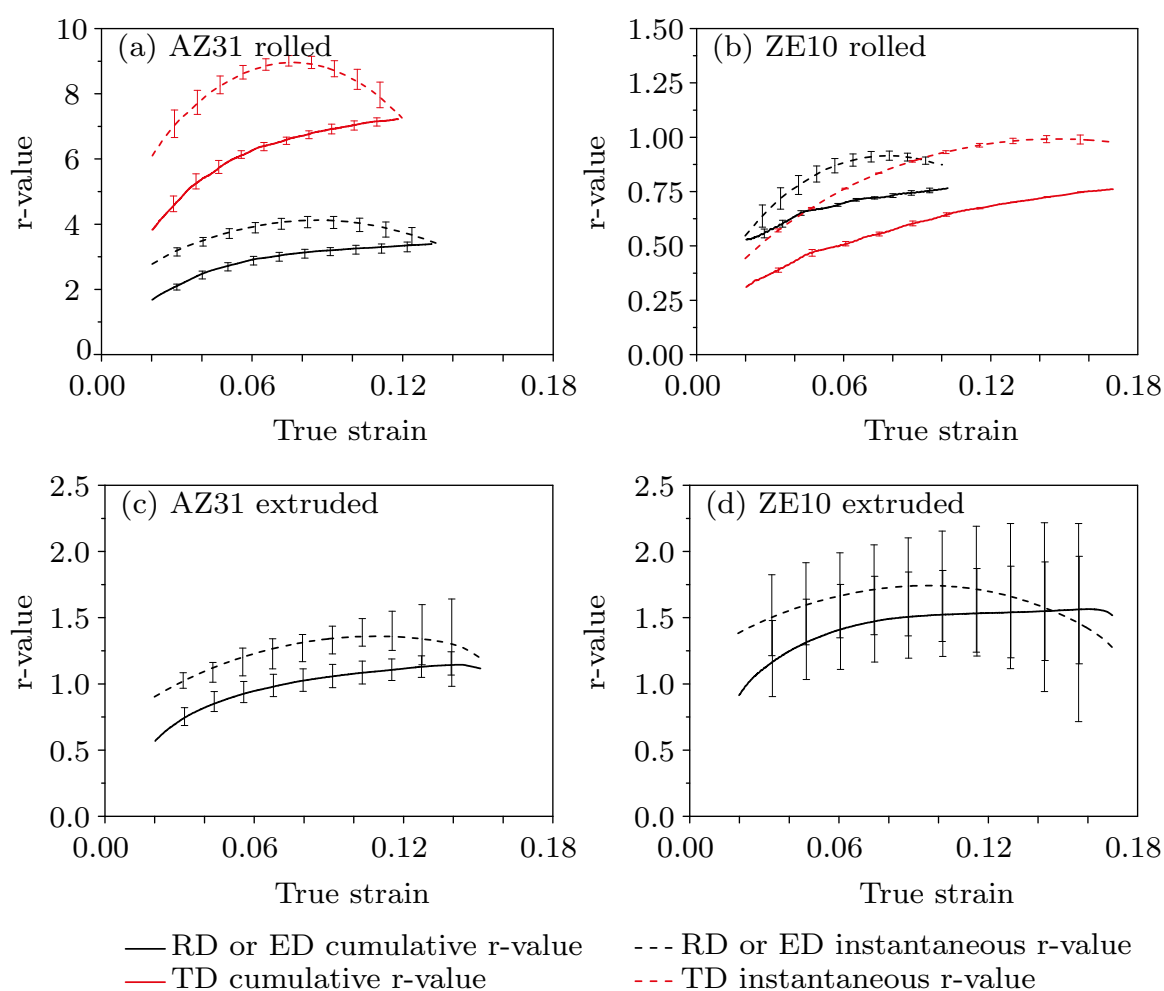


Figure 3.9: Cumulative r-value vs. instantaneous r-value in uniaxial tensile tests for (a) AZ31 rolled (b) ZE10 rolled (c) AZ31 extruded (d) ZE10 extruded

mechanical behaviour. It can be concluded that the measurements of the width change of the micro-tensile specimen with laser extensometer could not be used for magnesium alloys.

3.3.2 Uniaxial compression tests

In order to validate the in-plane compression testing method using glued cube samples described above, the results obtained for AZ31 rolled sheet material by this method are compared with data acquired using a comb-shaped die and a single sheet. The engineering stress strain curves of the three samples oriented in RD using cube specimens are plotted together with the result using flat specimens, see Fig. 3.12. The respective sets of curves differ in the early stage of deformation, in which elastic deformation is dominant. While the

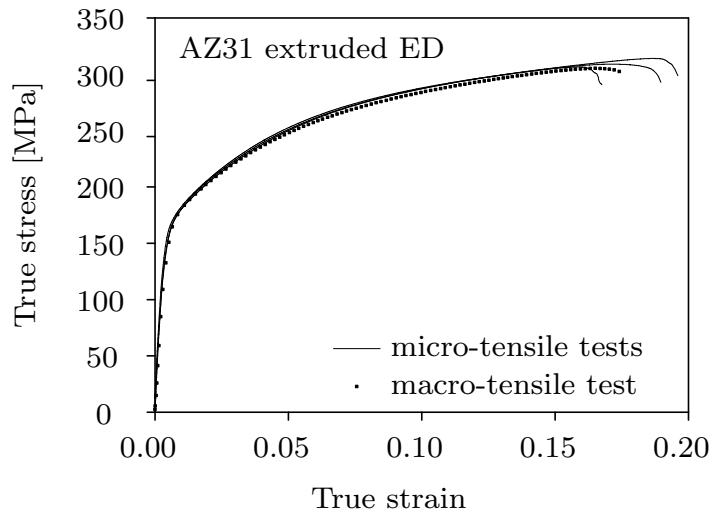


Figure 3.10: Comparing between macro-tensile tests and micro-tensile tests results for AZ31 extruded sheets in ED

displacement signal calculated from the comb-shaped die is based on strain gauges and therefore can be regarded as being exact, the displacement signal from the cube tests is influenced by “seating” of the sample. Consequently, the elastic slope (indicated in Fig. 3.12) is not met. This can be compensated once the plastic response is calculated by subtracting a “pseudo-elastic strain” from the recorded strain. In this case the differences between the two uniaxial compression tests are acceptable. The cube tests furthermore show a very good reproducibility.

Fig. 3.13 illustrates the stress-strain curves of AZ31 and ZE10 during uniaxial compression tests. The results obtained are presented in terms of direction dependent flow curves and r-values.

The anisotropic behaviour follows the same way with that of the tensile test. The in-plane anisotropy can be observed. In case of AZ31, the yield stress in TD is higher. On the contrary, the yield stress in RD is higher for ZE10. Differences between rolled and extruded material are not pronounced. Failure of the samples happened slightly earlier in case of the extruded products, which follows the same trend recorded in tension. It should be noted here that the extruded product showed a tendency to buckling before failure, but the rolled sheets did not. Compared to the plane rolled products, the extruded panels were slightly warped, fostering plastic instability.

An interesting feature of the compression tests is the evolution of the r-value during deformation. Different to the frequently reported evolution in tension, the r-values in compression are very low - the respective values are generally below 0.2. Only in case of ZE10 rolled sheet (RD) it reaches a maximum value of 0.4 prior to failure. The negative values result from thickening of the samples

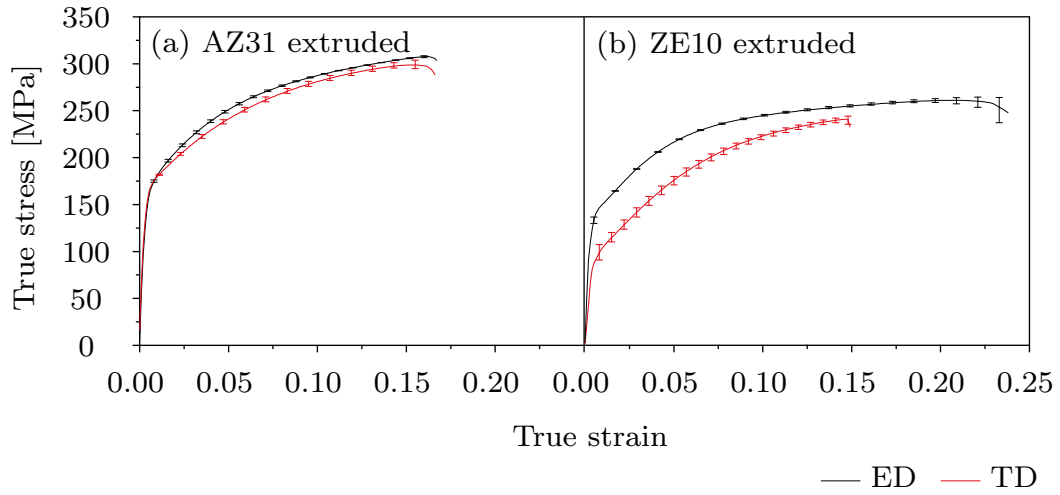


Figure 3.11: True stress strain curves in micro-tensile tests for extruded (a) AZ31 (b) ZE10

due to extensive twinning activity. The difference between the cumulative r -value and instantaneous r -value in compression is more impressive, see Fig. 3.14. For rolled sheets, the strong basal texture of AZ31 favours twinning when the compression stress is applied along the in-plane direction compared with ZE10 which leads to higher yield stress in compression because twinning cannot be easily activated as it does in AZ31. It results the differences between tension and compression yield stress which is called strength differential effect (SD effect). It is consequently less significant in the ZE10 sheets, see Table. 3.2. For the ZE10 extrusion, the texture exhibits big difference with rolled sheets, it shows strong basal texture with broad angular distribution towards the TD, which explained the larger yield stress in ED but not RD as for the rolled sheets and the strength differential (SD) is also higher than its counterpart in rolled sheets.

3.3.3 Through thickness compression tests

The experimental results of two through thickness compression tests using AZ31 stacked coins with 1 mm thickness were plotted together with the already published results from hydraulic bulge test and the test using cruciform specimen (Steglich et al., 2012), see Fig. 3.15.

It shows the biaxial stress σ_b related with the plastic thickness strain ϵ_t^{pl} . For the tests using cruciform specimens, ϵ_t^{pl} were recomputed from the measured strain components along RD and TD assuming isochoric plastic deformation.

All tests revealed very similar characteristics. The experimental results of

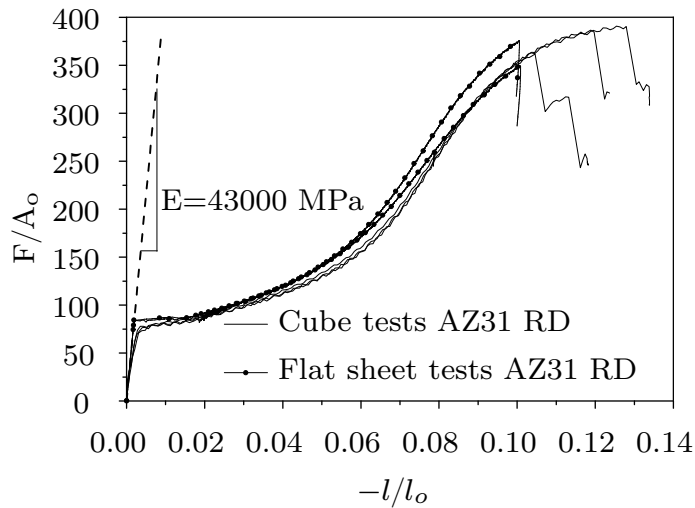


Figure 3.12: Engineering stress strain curves of cube and flat sheet tests for AZ31 along RD (Steglich et al., 2014)

the bulge test are subjected to scatter, while the experiments using cruciform specimens and the through thickness compression tests show smooth signal. The cruciform specimen reveals not equal signals for the two stress components in RD and TD due to the anisotropy of the material - which can only be identified by the magnification of the results, see Fig. 3.15. The experimental results derived from the through thickness compression tests yield almost identical result up to a total strain of 0.011, then the specimens failed by a shear fracture through their thickness, see Fig. 3.4(d). While in the tests using cruciform specimens the experiments were stopped once the arms of the cruciform specimen were torn off (Andar et al., 2012). Due to the good agreement of the tests with respect to the biaxial stress-strain curve, it seems that the compression test described here can be used to generate valid biaxial stress strain characteristics without further correction for friction.

Fig. 3.8 summarises the biaxial stress-strain curves obtained for the materials, ZE10 and AZ31, rolled sheets and extruded products. Note that in this case the thickness strain is used as the independent variable. For all materials, the curves are not parallel to those obtained by uniaxial tension. This evidences the distortional character of hardening (Mekonen et al., 2012). For AZ31 a high hardening rate is recorded. Failure of the samples appeared at relatively low strains - with ZE10 rolled sheet as an exception. In this particular case material separation appears at a plastic thickness strain of 0.3, which is approximately the same with the fracture strain observed in uniaxial tension along RD. The respective sample showed strong anisotropic deformation, leading to an oval shape of the initially circular coin stack. It fits with the desired results, because equal stresses imposed along the RD and the TD direction only result in identical principal strains once the biaxial r -value of the material equals unity

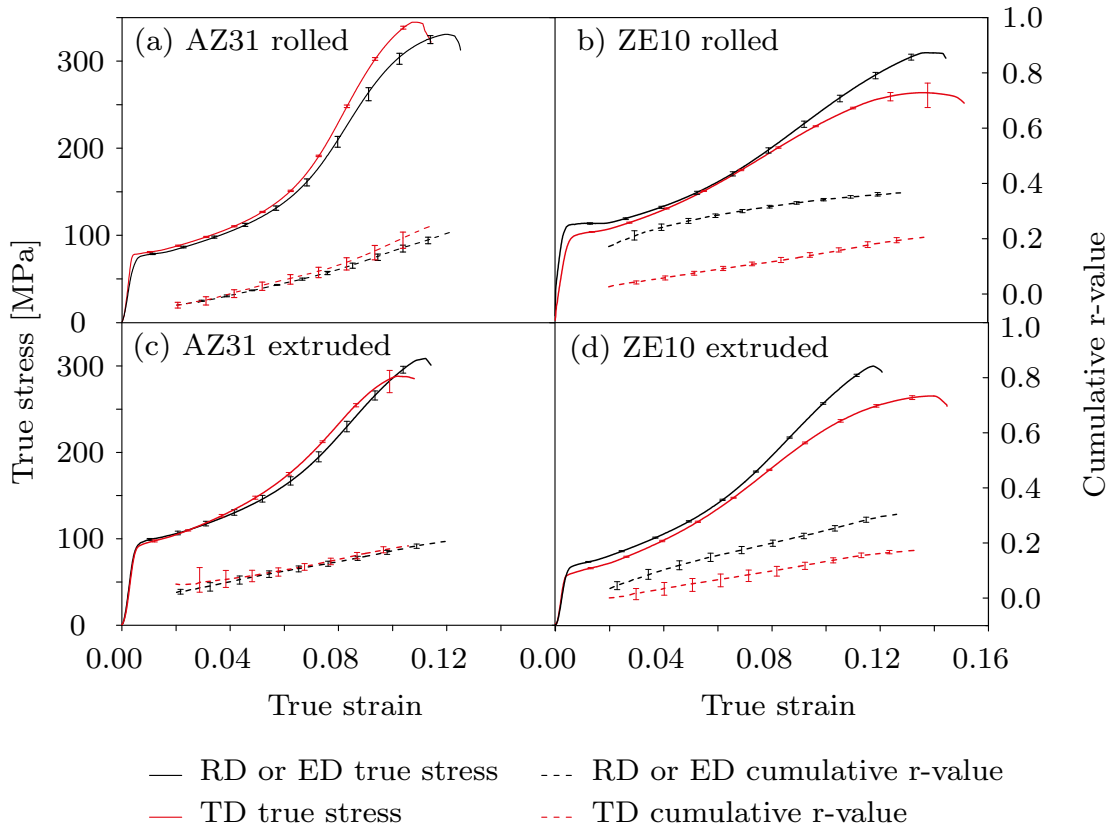


Figure 3.13: True stress strain curves for (a) AZ31 rolled (b) ZE10 rolled (c) AZ31 extruded (d) ZE10 extruded

(Aretz and Keller, 2011). Hence, any ellipticity of the stack observed after compression evidences a biaxial r-value different from unity.

It has been shown that the differential work-hardening behaviour comparing between biaxial testing and uniaxial tensile testing is caused by the delayed activation of prismatic slip under equi-biaxial stresses acting perpendicular to the basal plane (Takayuki and Hirohiko, 2012). To examine the mechanism of the change in the activity of the prismatic slip systems, the following simple analytical model is used. To simplify the model, an idealised HCP crystal structure whose c-axis trends exactly in the sheet normal direction is considered as shown in Fig. 3.16, although the directions of the c-axes in wrought Mg alloy sheets in fact exhibit some variation from the sheet normal direction. Assuming that biaxial stresses σ_1 and σ_2 are acting on the crystal structure in the 1 and 2 directions respectively, the Schmidt's resolved shear stress of an arbitrary slip system can be expressed in the form

$$\tau_{slip} = \mathbf{m} \cdot \boldsymbol{\sigma} \cdot \mathbf{s} = \begin{Bmatrix} m_x & m_y & m_z \end{Bmatrix} \begin{bmatrix} \sigma_1 & 0 & 0 \\ 0 & \sigma_2 & 0 \\ 0 & 0 & 0 \end{bmatrix} \begin{Bmatrix} s_x \\ s_y \\ s_z \end{Bmatrix} = m_x s_x \sigma_1 + m_y s_y \sigma_2,$$

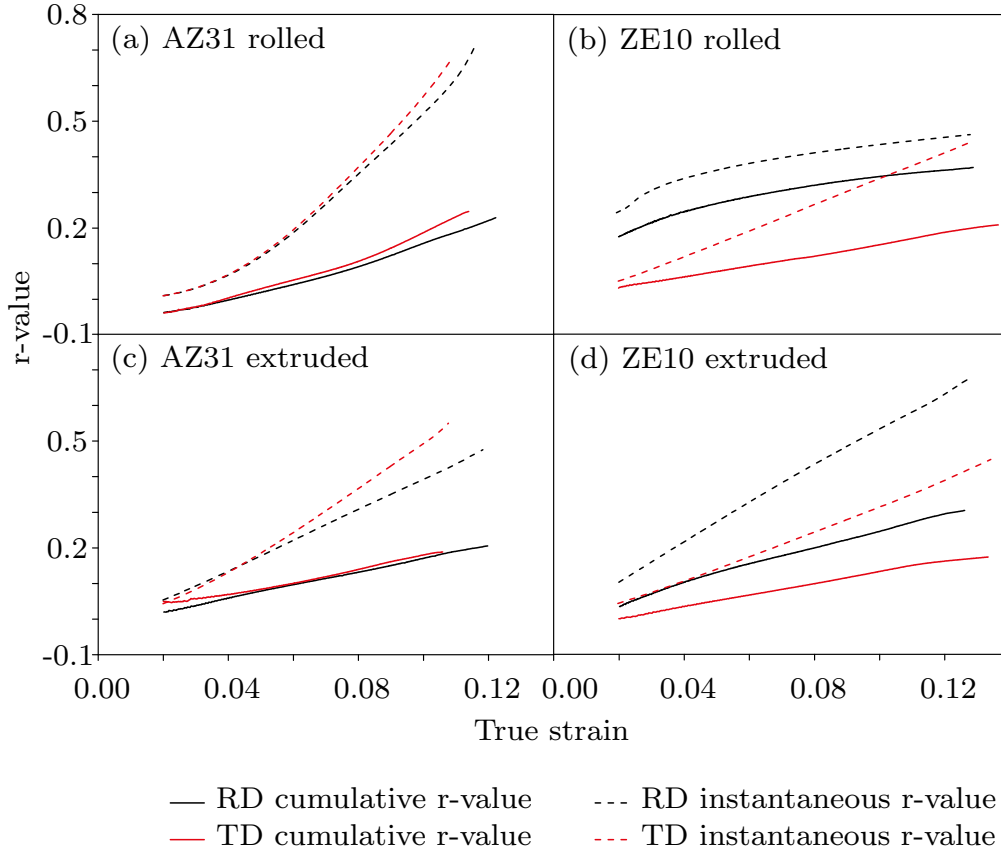


Figure 3.14: Cumulative r-value vs. instantaneous r-value in uniaxial compression tests for (a) AZ31 rolled (b) ZE10 rolled (c) AZ31 extruded (d) ZE10 extruded

(3.6)

where m_i and s_i are the components of the unit vectors \mathbf{m} and \mathbf{s} of this slip system which refer to the slip plane direction and the slip direction. They are indicated in the 1-2 coordinate system in Fig. 3.15. Using the angles θ and λ shown in Fig. 3.15, \mathbf{m} and \mathbf{s} of an arbitrary prismatic slip system are given by

$$m = \begin{Bmatrix} \cos\theta \\ \sin\theta \\ 0 \end{Bmatrix}, s = \begin{Bmatrix} \cos\lambda \\ \sin\lambda \\ 0 \end{Bmatrix}. \quad (3.7)$$

Introducing of Eq. 3.6 and Eq. 3.7 yields the resolved shear stress of the prismatic slip τ_{pris} given in the form

$$\tau_{\text{pris}} = (\sigma_1 - \sigma_2)\sin\lambda\cos\lambda \quad (3.8)$$

This equation revealed that τ_{pris} becomes 0 for equi-biaxial tension stress state, because the two biaxial stresses tended to cancel each other thus decreasing

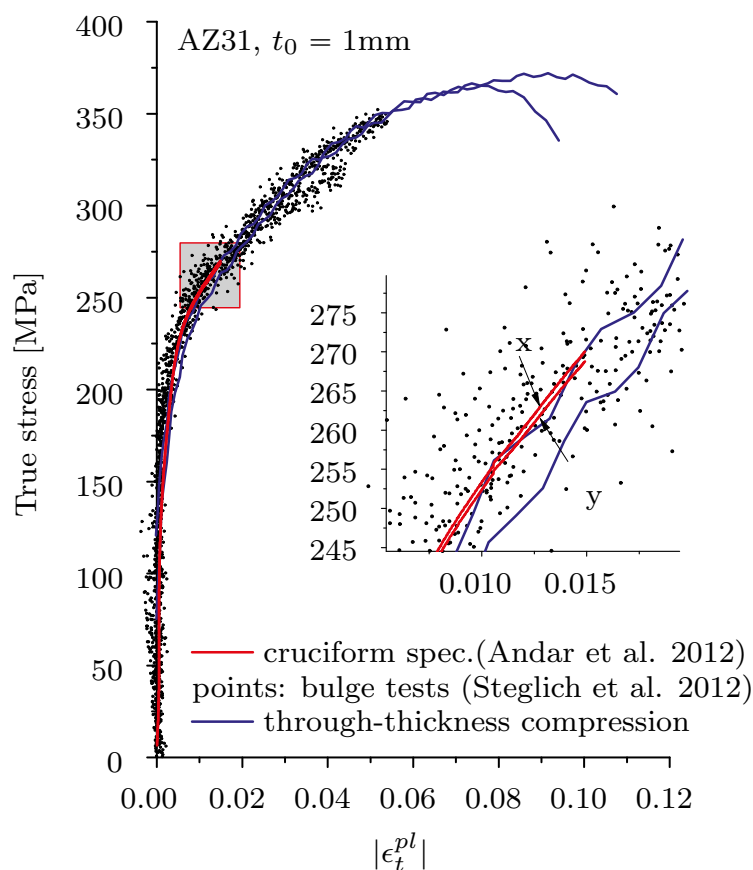


Figure 3.15: Verification of the through-thickness compression method (Steglich et al., 2014)

the relative activity as the biaxial stress ratio approached unity. As all tested products show a (more or less pronounced) basal texture, this effect is present in rolled and extruded products of both alloys (except for rolled ZE10).

For optical microscopy analysis, a deformed specimen of AZ31 rolled were cut out and mounted so that the plane perpendicular to the sheet plane can be observed. Subsequently, the samples were mechanically ground, polished and etched with a solution containing 30 ml water, 7 ml acetic acid, 140 ml ethanol and 9 g picric acid. Fig. 3.17(a) shows the overview of the middle layer of the deformed through thickness compression specimen.

The equi-biaxial tension loading condition resulted in extensive twinning, which was generally localised in bands of compression twins. The compression twin shear bands can be identified. They are indicated as the dashed lines in Fig. 3.17(a). The magnified image of compression twins in the shear bands can be observed in Fig. 3.17(b). The shear bands composed of compression twins were also observed by Scott et al. (2012) when the sheet is stretched in both biaxial and plane strain tension at room temperature. The shear banding

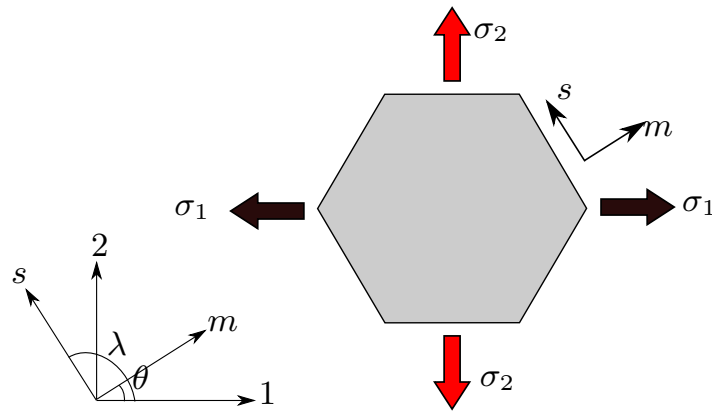


Figure 3.16: Analytical model of HCP crystal structure on which biaxial stresses are acting

phenomenon arises from the inability of the textured sheet to contract in the direction of the c-axis without tensile twinning. Extreme deformations occurring within shear bands lead to intense damage and fracture. The study conducted by Kang et al. (2011) showed that the onset of shear bands with a high density of compression twins in uniaxial specimens immediately precedes diffuse necking and failure. This explained the very low failure strain in the through-thickness compression tests for the material with very strong basal texture.

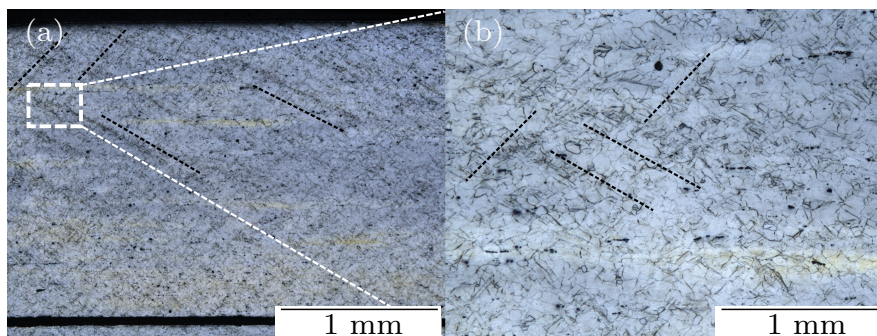


Figure 3.17: The microstructure of the third layer of the through thickness compression specimen of AZ31 after deformation: (a) Overview of the specimen, (b) Microstructure of the shear bands; The dashed lines indicated the direction of the shear bands.

3.3.4 U-notched bar tensile tests

Fig. 3.18 shows the force displacement curves of AZ31 and ZE10 along RD and TD in the U-notched bar tensile tests. For AZ31, the force level along TD is higher than that of RD and it is just in the opposite for ZE10. It has the same trend with the experimental results of the uniaxial tensile tests. ZE10 exhibits higher displacement before failure than AZ31 in the notched bar tests and the displacement before failure along TD is higher than RD which is also the same trend with the experimental results of the uniaxial tensile tests.

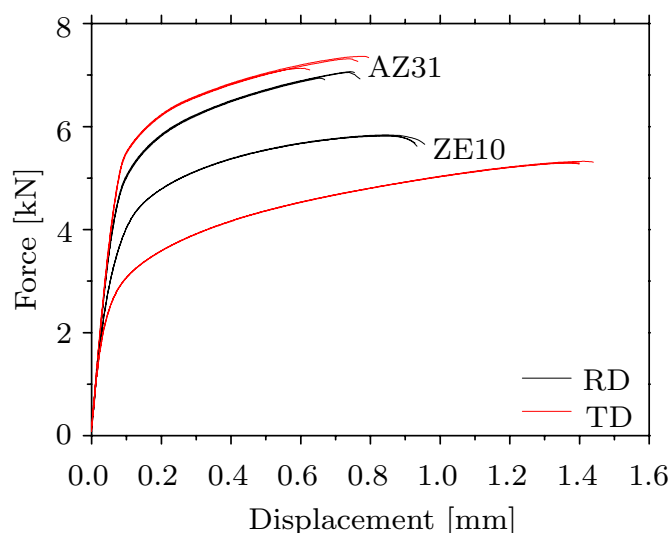


Figure 3.18: Force-displacement curves of the U-notched bar tensile tests for AZ31 and ZE10.

3.3.5 Shear tests

Fig. 3.19 shows the force-displacement curves of the shear tests and the error bars are included. AZ31 exhibits higher force than ZE10 while the elongation of ZE10 is higher than that of AZ31.

For optical microscopy analysis, the deformation zone of the tested shear specimens were cut out and mounted to investigate the twinning behaviour under shear stress state. Subsequently, the samples were mechanically ground, polished and etched with a solution containing 30 ml water, 7 ml acetic acid, 140 ml ethanol and 9 g picric acid.

Fig. 3.20(a) shows the overview of the deformation zone of AZ31 after etching. It was generally divided into dark part and bright part. In the transition part, the dark lines can be clearly identified. The dark zone b, transition zone c and bright zone d was magnified and shown in Fig. 3.20(b), Fig. 3.20(c),

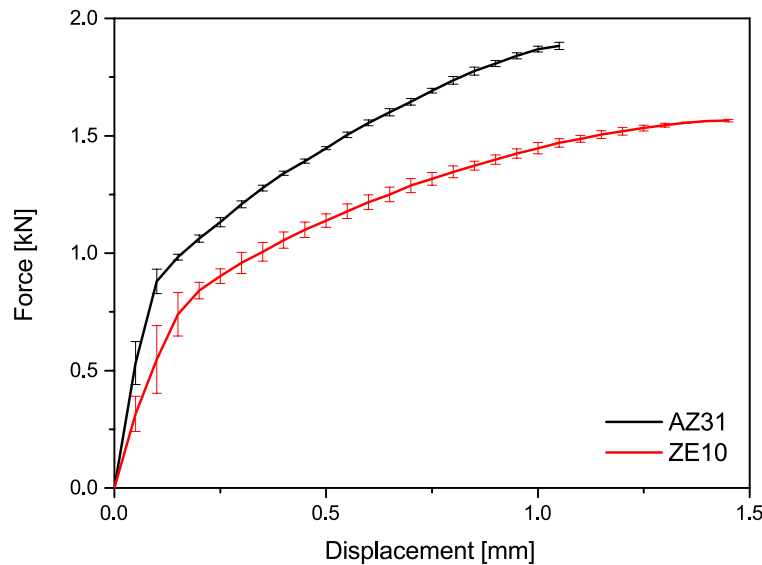


Figure 3.19: Force-displacement curves including error bars of the shear tests for AZ31 and ZE10.

Fig. 3.20(d) respectively. Fig. 3.20(b) indicated the big fraction of twins that were identified mainly as $(10\bar{1}2)[10\bar{1}1]$ tensile twins. In the transition part, the black lines represent the extension direction of the twins which can be seen in Fig. 3.20(c). In the bright part, no twins were identified. The thickness of the center of the deformation zone was carefully measured and found to be 2.19 mm. The original thickness of the rolled sheet is 2 mm. This is consistent with the presence of tensile twins with the extension of the c axis which is the thickness direction for rolled AZ31 sheets. The same with the observation of Lou et al. (2007), the tensile twinning deformation mechanism is activated under shear stress state combined with the thicken of the metal sheet.

3.4 Conclusions

A relatively simple method to determine the compressive behaviour of sheet metal was used to quantify the mechanical behaviour of both of rolled and extruded magnesium alloys, AZ31 and ZE10. Two independent sets of extensometers were used to simultaneously record longitudinal and transversal strains. The method was successfully validated by a more sophisticated setup based on comb dies.

A very similar setup was used to assess the equi-biaxial tensile behaviour of these materials. This method was also successfully validated by hydraulic bulge and cruciform specimen tests. Higher strain before failure can be achieved with this method because the plastic instabilities are suppressed compared

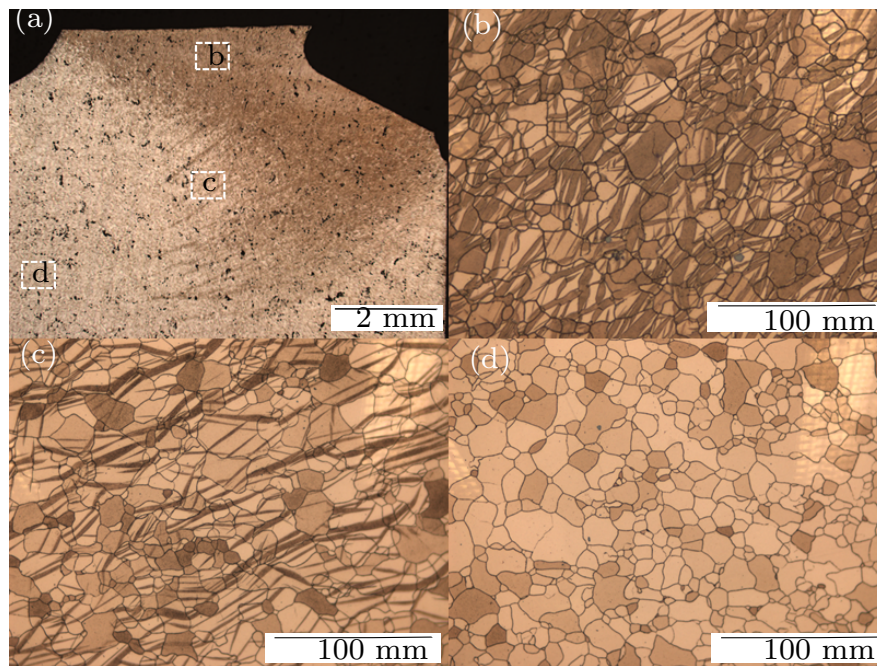


Figure 3.20: Microstructure of AZ31 rolled sheets in the deformation zone after the shear test

with the two aforementioned methods.

Mechanical tests were conducted along the orthotropic axes of the materials. The measured behaviour was correlated with the microstructural information. Certain trends could be explained through the fundamental deformation mechanisms present in magnesium alloys. An evolving strength differential effect in flow stress response of all materials was observed. The compressive r -values are generally lower than the tensile r -values.

Except the elementary tests mentioned above, two “structure test”: notched bar tensile tests and shear tests were conducted to investigate the mechanical behaviour at lower stress triaxility and inhomogeneous stress and strain fields. The generated results are comprehensive enough to be used as an input for constitutive modelling.

4 Model parameter identification

In order to describe the evolved tension compression asymmetry behaviour of wrought magnesium, the modified CPB2006 model (Cazacu et al., 2006) including a series of parameters is developed which is described in Chapter 2. According to the experimentally observed mechanical response in Chapter 3, the series of parameters are identified to achieve the best estimate of the developed model. The parameter identification is achieved by minimising the difference between the experimental observation and that predicted by the model.

4.1 Determination of isotropic hardening

The isotropic hardening was assumed to obey the following form,

$$R(p) = R_0 + Q_1(1 - e^{-b_1 p}) + Q_2(1 - e^{-b_2 p}). \quad (4.1)$$

It describes a two phase exponential association. R starts out equal to R_0 and increases with fast and slow components (related with the double exponential function) to a maximum plateau $R_0 + Q_1 + Q_2$. The function describes the typical convex shape of strain hardening in case of uniaxial tension. The curve is not obviously biphasic, and it takes a very practiced eye to see that the curve does not follow a single phase model.

The values for R_0 and the coefficients in the exponential function of Eq. 4.1 were obtained by minimising the target function

$$\delta^{iso} = \sum_p [R_e(p) - R(p)]^2, \quad (4.2)$$

where $R_e(p)$ are the true stress-strain curves in tension along the rolling direction or extruded direction obtained from experiments. The values of these coefficients for rolled and extruded AZ31 and ZE10 are reported in Table 4.1. Fig. 4.1 shows the fitted stress responses established based on the identified parameters for the four materials rolled and extruded AZ31 and ZE10.

Table 4.1: Model parameters describing isotropic hardening for rolled and extruded AZ31 and ZE10

Alloy		R_0 [MPa]	Q_1 [MPa]	b_1 [.]	Q_2 [MPa]	b_2 [.]
Rolled	AZ31	87.8	134.42	15.99	86.42	2400.79
	ZE10	141.94	29.06	404.86	94.83	21.99
Extruded	AZ31	158.5	133.9	15.1	28.3	79.2
	ZE10	74.6	47.9	977.2	121.9	19.3

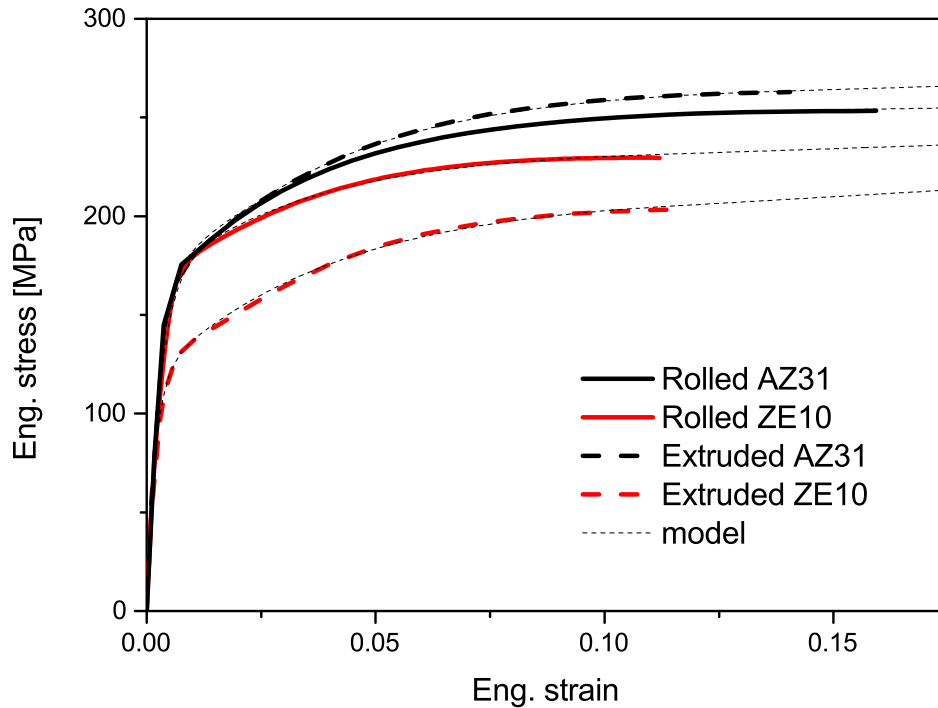


Figure 4.1: Fitted curves of the engineering stress strain responses of the specimens oriented in RD (ED for extruded material)

4.2 Parameter identification strategy

The two isotropic elasticity constants (Young's modulus E and Poisson's ratio ν) for the four materials were taken from the literature and verified using the uniaxial tensile tests. The identification of the model parameters included in the yield function needs an iterative procedure. Sequential quadratic programming (SQP) minimisation algorithms are used together with finite element simulations of the mechanical tests to calibrate the respective parameters. SQP methods solve a sequence of optimisation subproblems, each of which optimises a quadratic model of the objective subject to a linearisation of the constraints. The initial values of these parameters are selected and simulations of the mechanical tests start with these parameters. The difference between the experimental results and simulations is evaluated and based on this evaluation a new set of parameters is determined. This process is repeated until the difference is sufficiently small. For the simulations of uniaxial tensile, uniaxial compression tests and the through thickness compression tests, 3D single elements were used. The remaining tests (notched bar and shear test) were

modelled using 3D meshes, see Fig. 4.2 for the latter two.

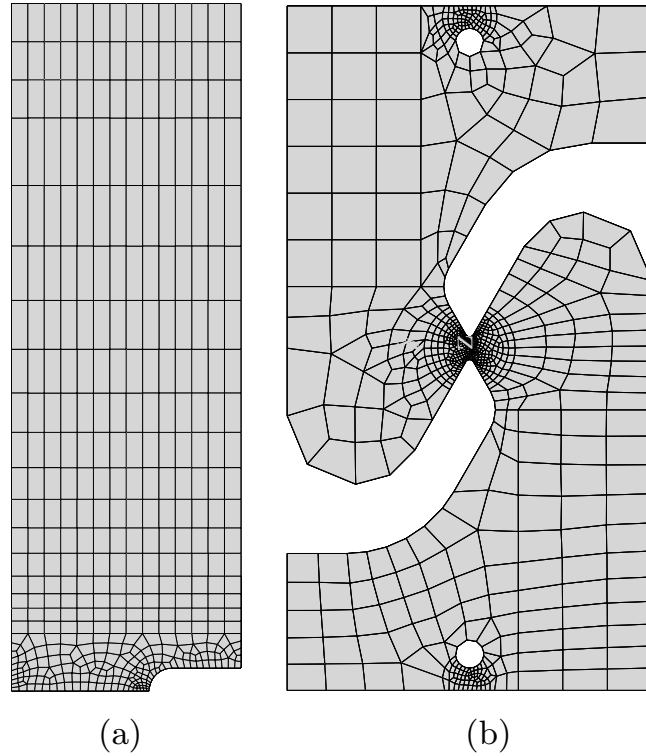


Figure 4.2: 3D finite element models of the notched bar specimen (a) and the shear test specimen (b) used for the optimisation process; Three-fold symmetry was used for the notched bar specimens (Steglich et al., 2016)

The difference between an experimental result $Y_e^n(X)$ and a simulated result $Y_s^n(X)$ is defined by (with n indexing each individual test)

$$\delta^n = \frac{1}{2(X_1^n - X_2^n)} \int_{X_1^n}^{X_2^n} (Y_e^n(X) - Y_s^n(X))^2 dX. \quad (4.3)$$

The interval $[X_1^n, X_2^n]$ depends on the curves that are compared. For smooth tensile and compression specimens, the range of homogeneous deformation was considered. Through-thickness compression, notched bar and shear test were examined up to fracture.

The global error is given by

$$\Delta = \sum_n \omega^n \delta^n, \quad (4.4)$$

where ω^n are weighting factors. Thus, the optimiser accounts for a finite number of tests.

4.3 Parameter calibration

4.3.1 CPB2006 model

The mechanical tests were simulated by means of quasi-static finite element analyses under displacement control using the FE software package ZeBuLoN (Besson et al., 1998). For CPB2006 model (Cazacu et al., 2006), all of the parameters are constants. The uniaxial tensile test and uniaxial compression test including the stress and width change records for rolled materials are included for the parameter identification for CPB2006. Note that the optimisation with respect to the width deformation is equivalent to adjusting the Lankford coefficient. As the value of a does not influence the yield stress in tension, compression, shear and equi-biaxial stress states as shown in Fig. 2.6, the value of a will not have big influence to the calibration results and it is set to 2 in the identification procedure. As the yield function is optimised for a thin sheet (closed to plane stress state), c_{44} c_{55} c_{66} cannot be adjusted. In a 3D calculation, they were set equal to 1. The determined parameters are presented in Table. 4.2.

Table 4.2: Model parameters corresponding to CPB2006 model for rolled AZ31 and ZE10

Parameter	k	c_{11}	c_{22}	c_{33}	c_{12}	c_{23}	c_{31}
AZ31 rolled	0.40	1.37	1.31	-0.51	-0.008	-0.81	-0.81
ZE10 rolled	0.42	1.33	1.30	0.89	0.16	-0.26	-0.17

4.3.2 Modified CPB2006 model

As the model in the original form is not suitable for capturing the evolving tension compression asymmetry behaviour, the CPB2006 model was modified and described in Sec.2.3. A comprehensive set of experiments which are shown in Table. 4.3 are included in the model parameters optimisation for all of the four materials. The value of a was set to 2 and the parameters c_{44} , c_{55} , c_{66} are set to 1.

The determined parameters are presented in Tables 4.4 and 4.5. Figs. 4.3-4.16 show the comparison of the respective simulation results with the mechanical tests.

Table 4.3: The experiments included in the model parameters identification procedure

Alloy		UTT		UCT		TTC	UNB	SH
		NL	NWC	NL	NWC	NL	NL	NL
Rolled	AZ31-RD	✓	✓	✓	✓	✓	✓	✓
	AZ31-TD	✓	✓	✓	✓	✓	✓	✓
	ZE10-RD	✓	✓	✓	✓	✓	✓	✓
	ZE10-TD	✓	✓	✓	✓	✓	✓	✓
Extruded	AZ31-ED	✓	-	✓	✓	✓	-	-
	AZ31-TD	✓	-	✓	✓	✓	-	-
	ZE10-ED	✓	-	✓	✓	✓	-	-
	ZE10-TD	✓	-	✓	✓	✓	-	-

UTT-Uniaxial tensile tests, UCT-Uniaxial compression tests, TTC-Through thickness compression tests, UNB-U notched bar tests, SH-shear tests, NL-Normalised load, NWC-Normalised width change

4.4 Macroscopic effects described by the two models

For the model CPB2006, the optimised results are plotted as the red curves together with that of the modified model. The observed mismatch between the experimental and the computed stresses in compression is obvious, the simulated stress strain curves do not show the “S” shape hardening, see Figs. 4.4, 4.8.

For the modified CPB2006 model, the following statements can be derived from the model calibration results described in Figs. 4.3-4.16:

1. For the uniaxial tension and compression tests, the normalised force-displacement curves and width changes for the four materials are met with good accuracy. The modified CPB2006 model can successfully describe the evolved tension compression asymmetry. This is because the value of k are set as a function evolving respectively in tension and compression. The model can also capture the stress and strain anisotropy. The different yield stress and width change along RD (or ED) and TD can be described.

The different mechanical behaviour between the two alloys AZ31 and ZE10 (both rolled and extruded products) can also be captured by the modified CPB2006 model. For the alloy ZE10, the stress anisotropy in tension is much more pronounce than alloy AZ31. This is successfully captured, see Figs. 4.7 and 4.14. The width changes in uniaxial tension are also met very well for the four materials. The width change in compression is generally small compared to the one in tension, which is related with twinning activity during compression. The upturn of the width change in compression related to the saturation

Table 4.4: Model parameter describing the plastic anisotropy of rolled material AZ31 and ZE10

	AZ31-rolled			ZE10-rolled		
Parameter	A	B	C	A	B	C
k_c	1.31	16.44	0.9	0.69	-0.07	0.48
k_t	0	0	0.2	0	0	0.06
c_{11}	0.94	0	0	0.85	0	0
c_{22}	0.89	0	0	0.8	0	0
c_{33}	-0.77	0	0	-1.12	0	0
c_{12}	-0.18	0	0	-0.16	0	0
c_{23}	-0.62	2.15	2.14	-1.39	2.84	2.89
c_{31}	-0.64	2.05	2.06	-0.51	1.96	2.02

Table 4.5: Model parameter describing the plastic anisotropy of extruded material AZ31 and ZE10

	AZ31-extruded			ZE10-extruded		
Parameter	A	B	C	A	B	C
k_c	1.28	20.72	0.9	0.82	10.44	0.66
k_t	0	0	0.32	0.06	46.95	-0.33
c_{11}	0.97	0	0	0.74	1.36	-1.29
c_{22}	0.95	0	0	0.66	2.39	-0.06
c_{33}	-1.73	0	0	-0.07	1.95	-2.09
c_{12}	-0.16	0	0	-0.24	0	0
c_{23}	-0.27	0	0	-0.57	0	0
c_{31}	-0.16	0	0	-0.5	0	0

of twinning is also captured by the developed model. However, the values are overestimated.

2. In case of the through thickness compression test (TTC), the abnormally high hardening rate of extruded material and rolled AZ31 can be predicted very well, see Fig. 4.5. In the respective counterpart rolled material ZE10, the simulation meets the experiments over a wider range of strain reasonably well although the through thickness compression behaviour of them is significantly different, see Fig. 4.5 and 4.9.

3. The force-NOD record obtained from the notched bars of rolled materials could be described with reasonable accuracy. For ZE10 along TD, the force was overestimated by the prediction, see Fig. 4.10.

4. The shear behaviour quantified by the shear test is well predicted in case

of AZ31. In case of ZE10, the experimentally recorded load is underestimated by the simulation, see Fig. 4.9.

One feature to be mentioned here is the in-convexity of the proposed material model near the shear stress state which is related to the transition of the function for the parameter k from tension stress state to compression stress state to account for the tension-compression asymmetry, see Fig. 2.8(b). The application of the model to the deformation including shear stress state is limited.

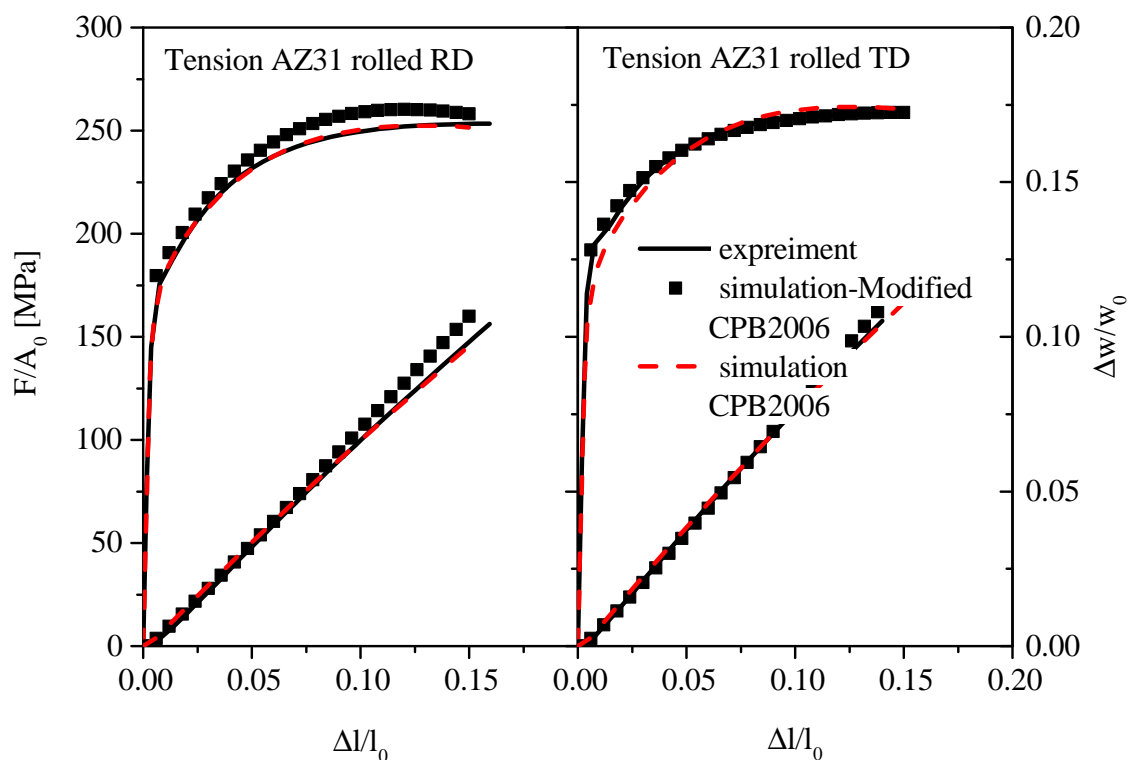


Figure 4.3: Result of the parameter calibration process for AZ31 rolled: tensile test results and FE-predictions

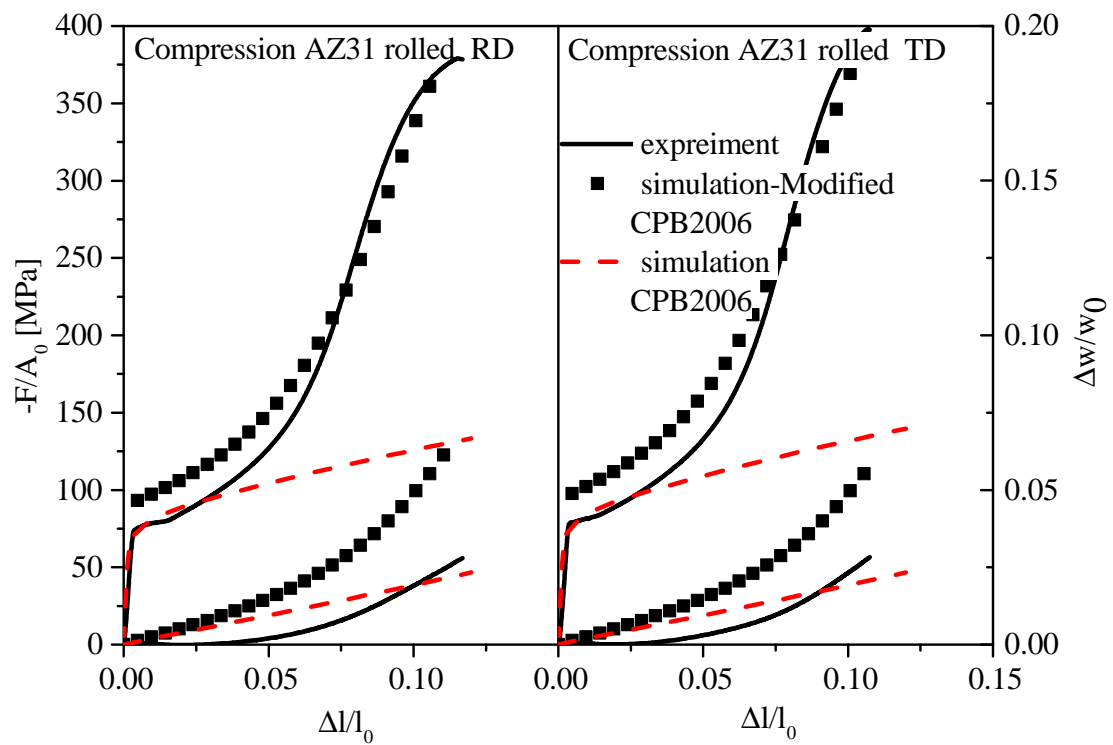


Figure 4.4: Result of the parameter calibration process for AZ31 rolled: compression test results and FE-predictions

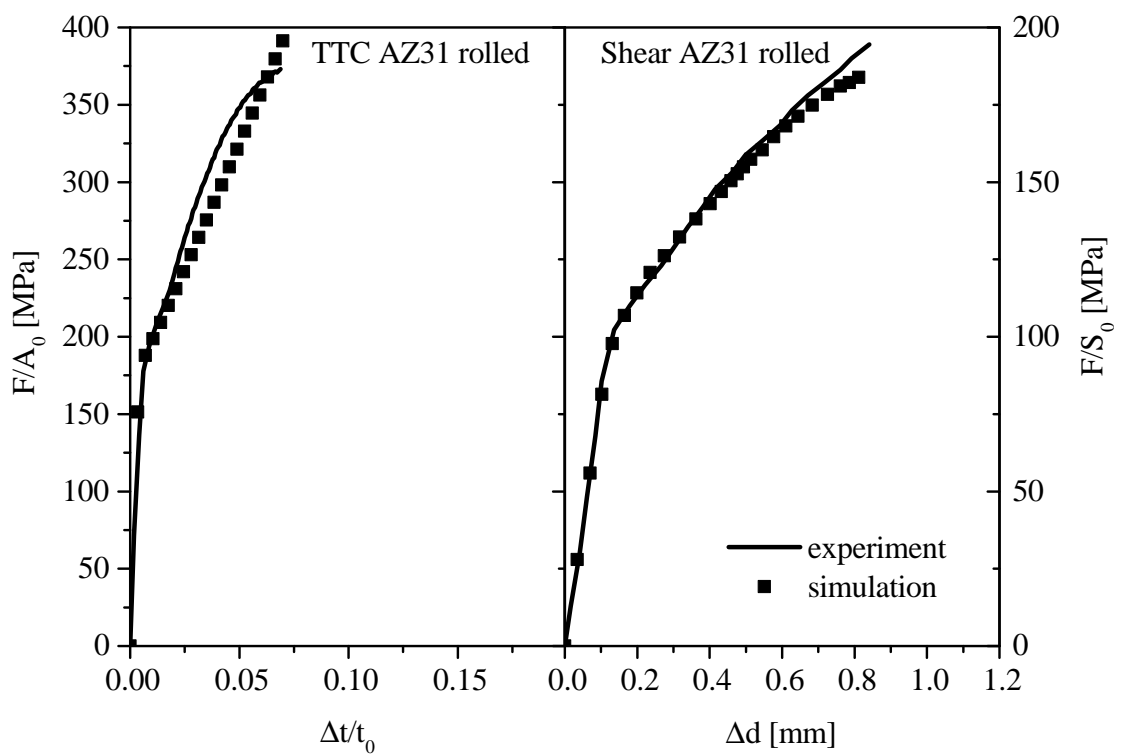


Figure 4.5: Result of the parameter calibration process for AZ31 rolled: through thickness compression test and shear test results and FE-predictions

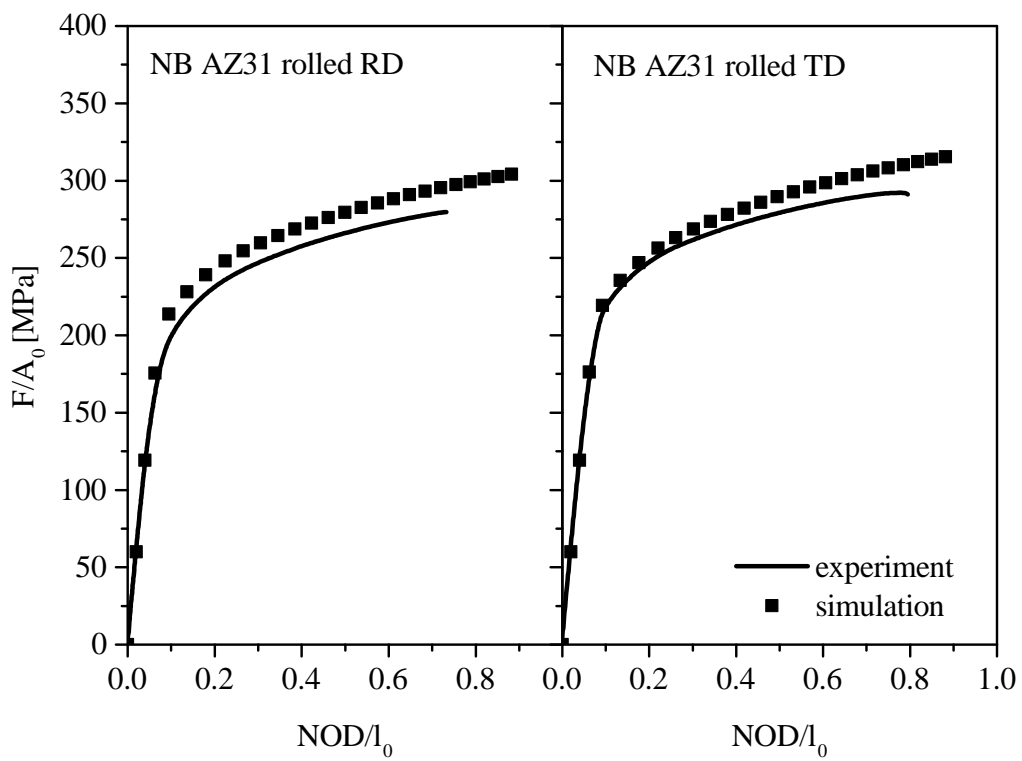


Figure 4.6: Result of the parameter calibration process for AZ31 rolled: Notched bar test results and FE-predictions

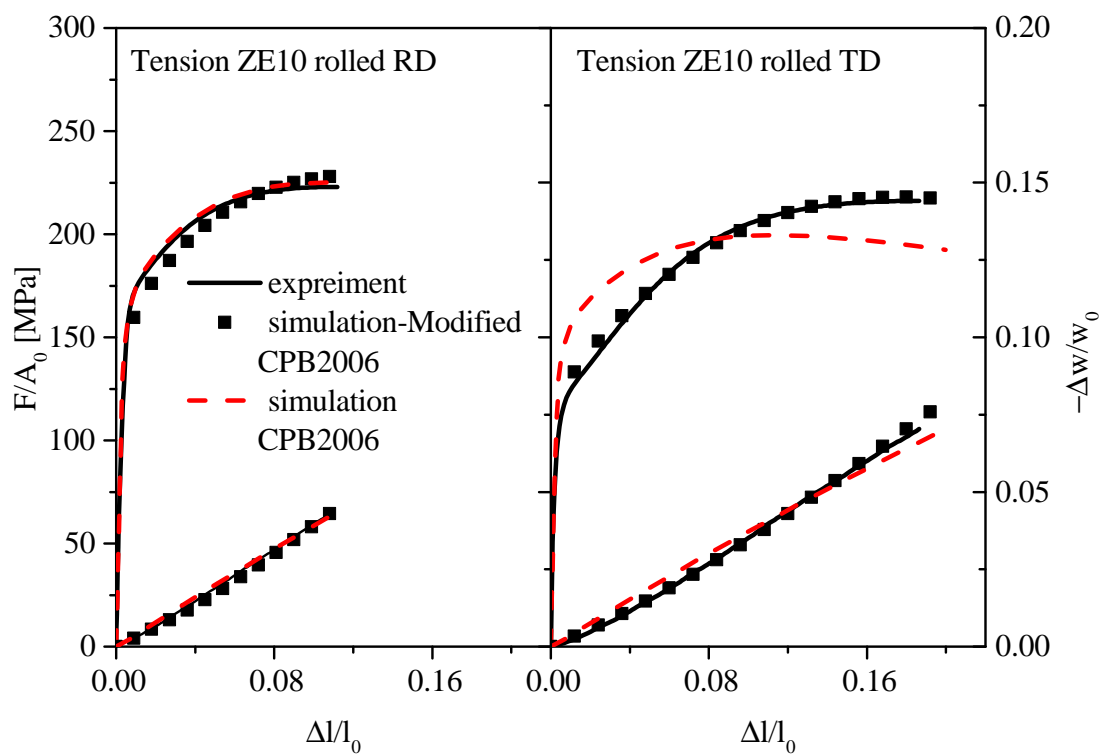


Figure 4.7: Result of the parameter calibration process for ZE10 rolled: tensile test results and FE-predictions

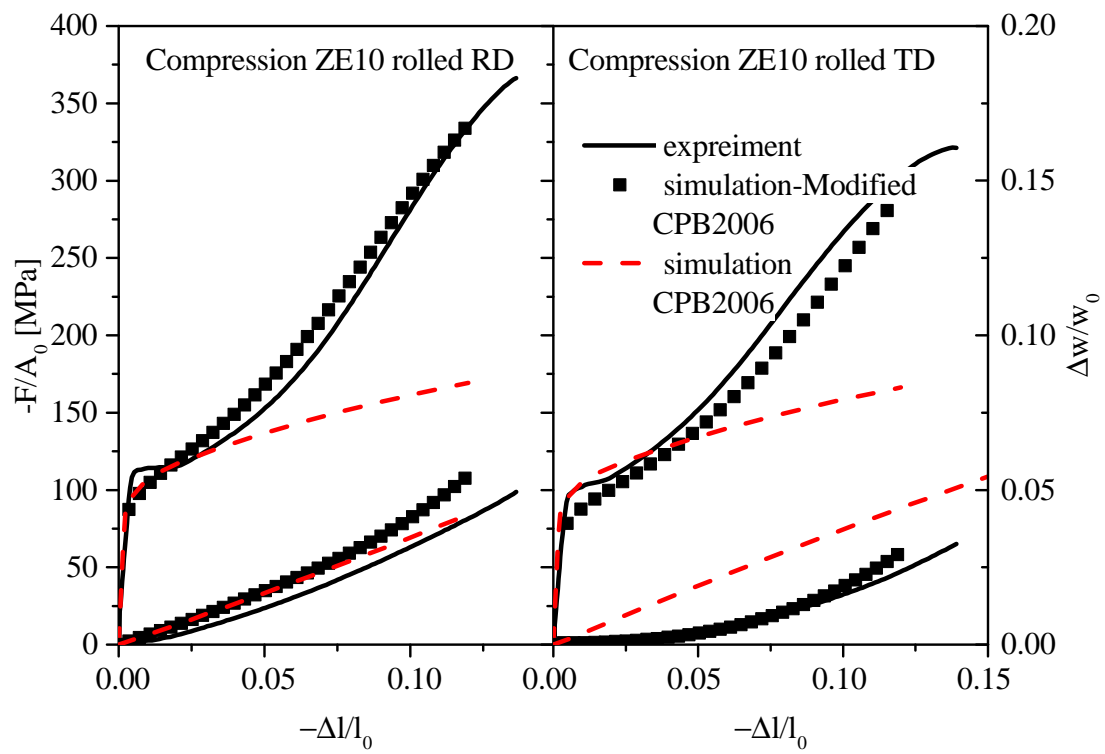


Figure 4.8: Result of the parameter calibration process for ZE10 rolled: compression test results and FE-predictions

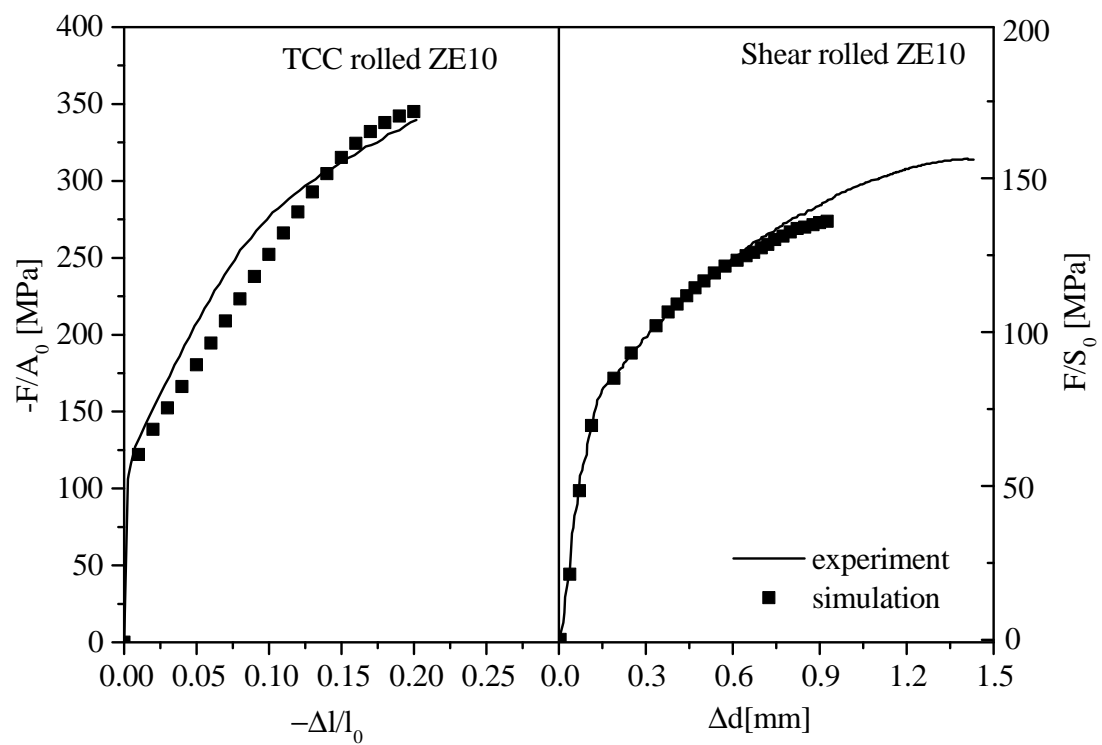


Figure 4.9: Result of the parameter calibration process for ZE10 rolled: through thickness compression test and shear test results and FE-predictions

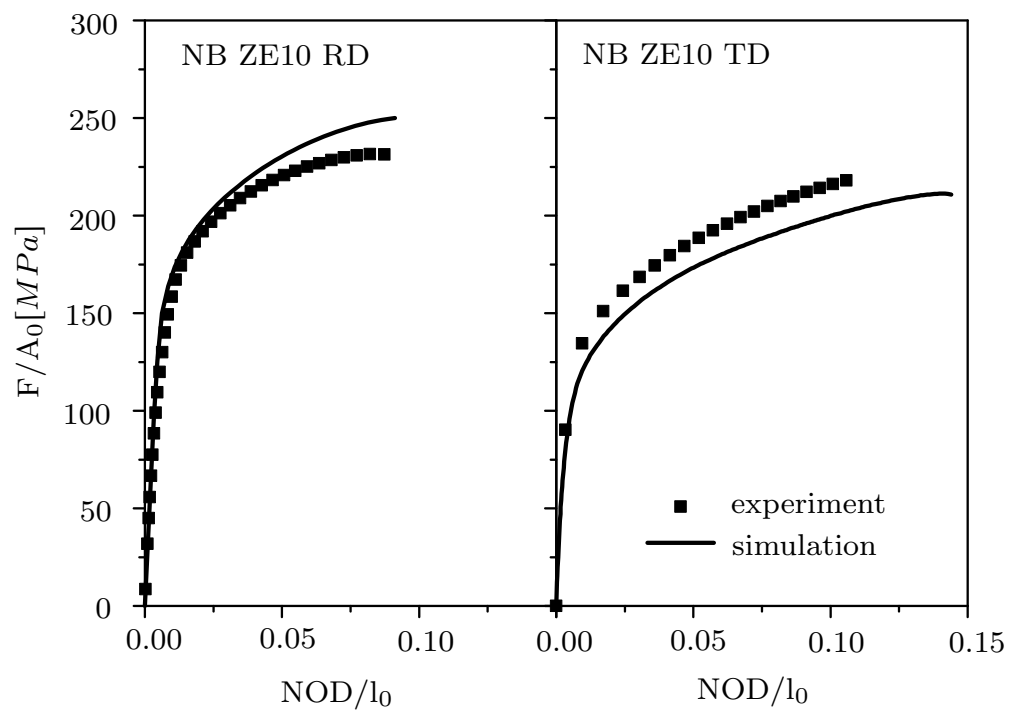


Figure 4.10: Result of the parameter calibration process for ZE10 rolled: notched bar test results and FE-predictions

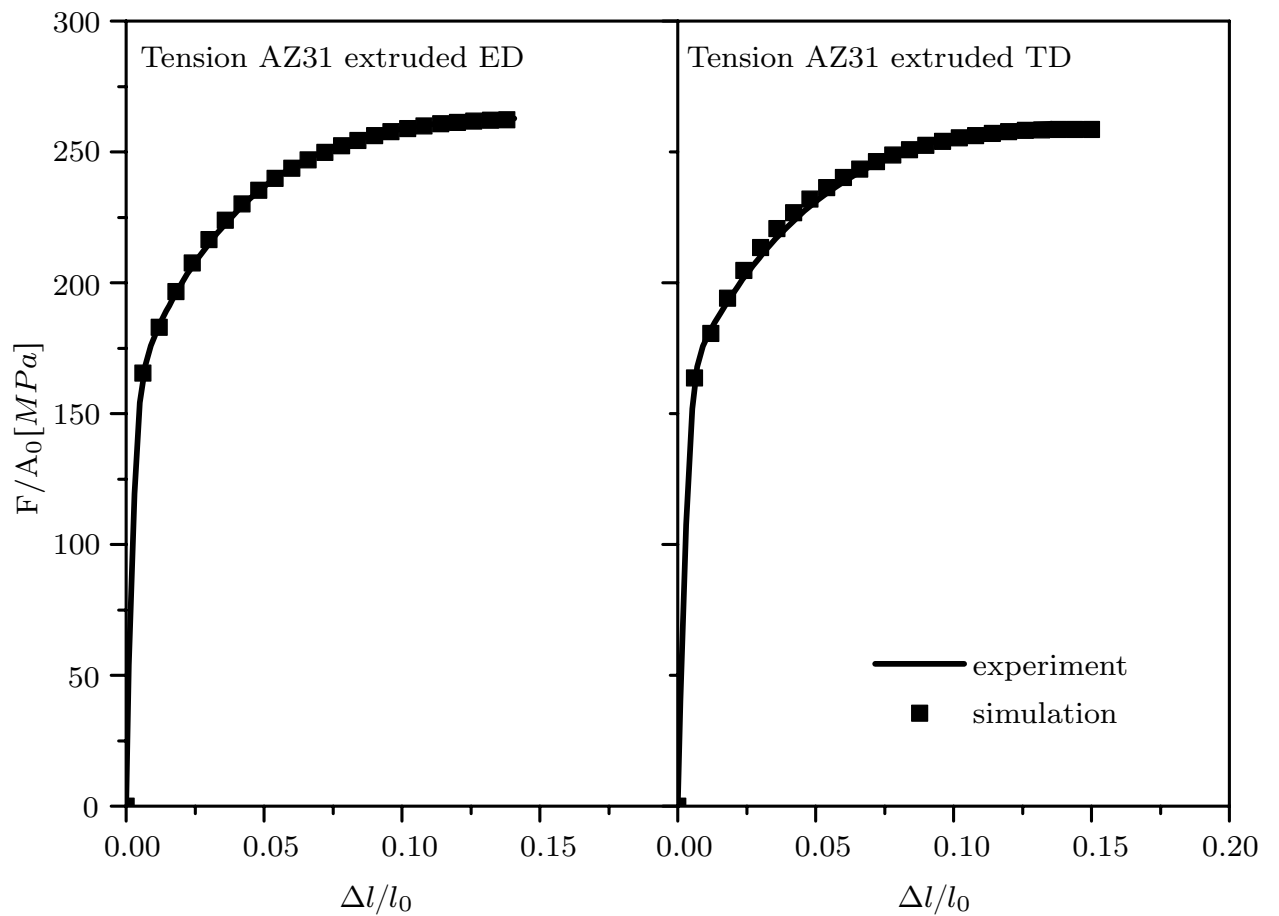


Figure 4.11: Result of the parameter calibration process for AZ31 extruded: tensile test results and FE-predictions

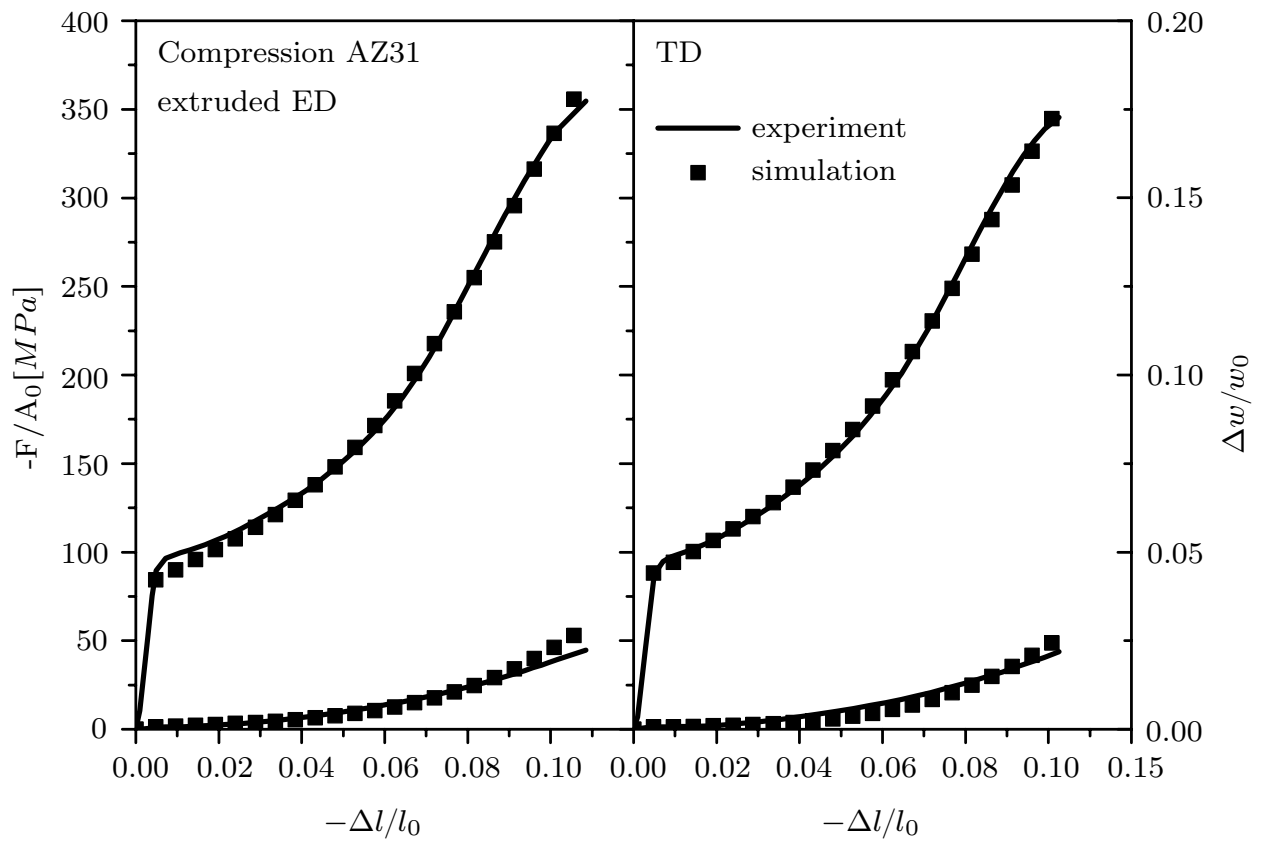


Figure 4.12: Result of the parameter calibration process for AZ31 extruded: compression test results and FE-predictions

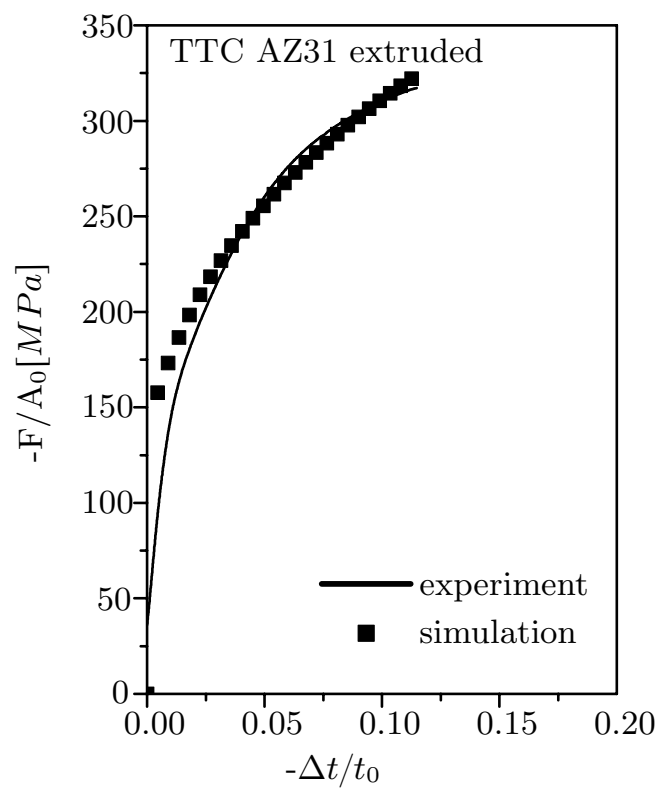


Figure 4.13: Result of the parameter calibration process for AZ31 extruded: through thickness compression test results and FE-predictions

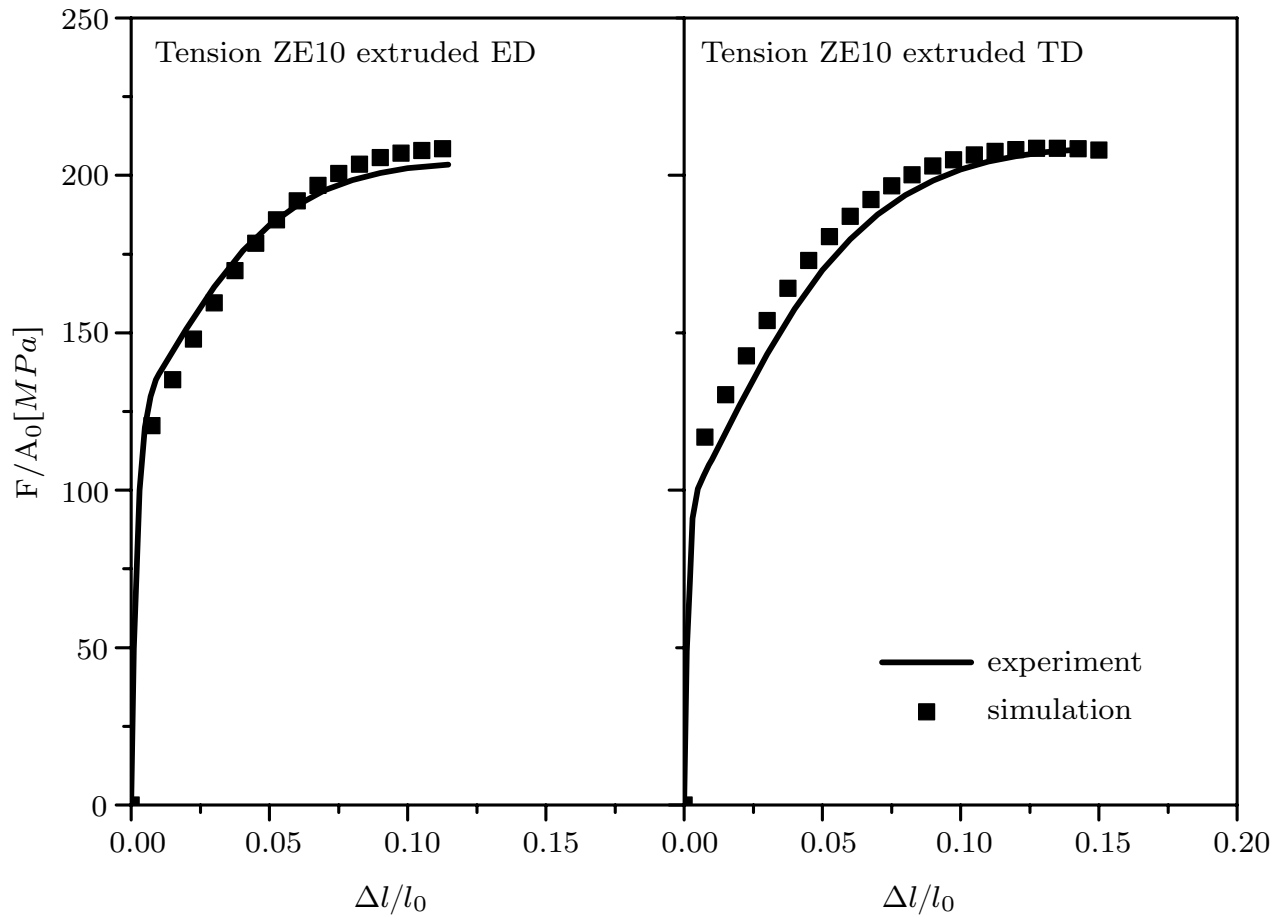


Figure 4.14: Result of the parameter calibration process for ZE10 extruded: tensile test results and FE-predictions

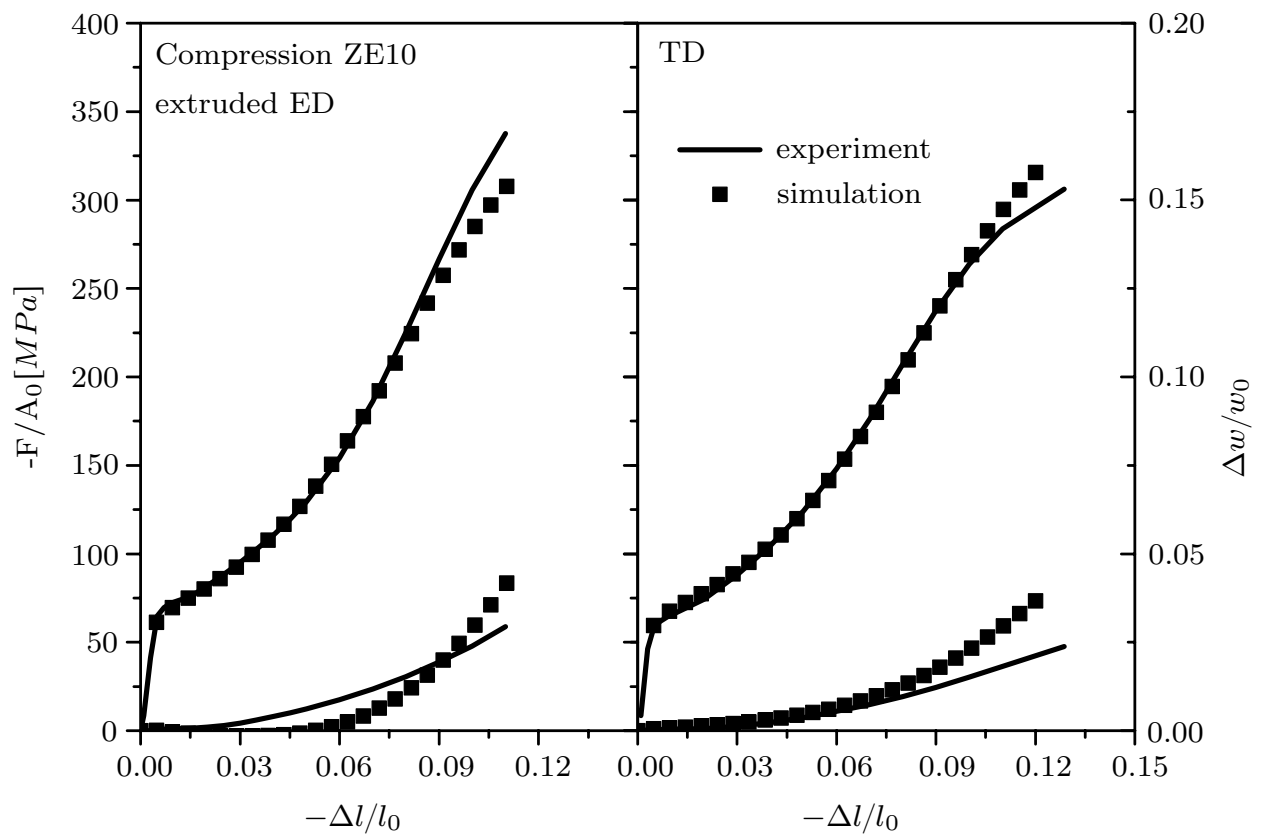


Figure 4.15: Result of the parameter calibration process for ZE10 extruded: compression test results and FE-predictions

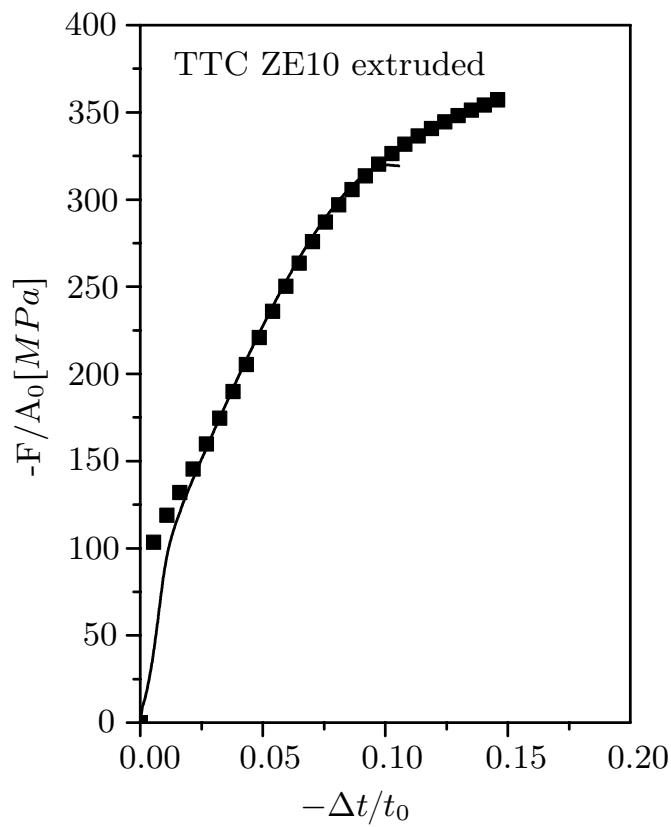


Figure 4.16: Result of the parameter calibration process for ZE10 extruded: through thickness compression test results and FE-predictions

4.5 Pure bending simulation

The pure bending simulation was performed using the calibrated model for rolled AZ31. Moreover, the simulated bending moment-curvature diagrams were compared with those calculated using the stress-strain curves obtained from the experiments to investigate the prediction capability of the developed model and the effect of tension compression asymmetry on the pure bending.

The main feature of the pure bending experiment is the absence of contact forces, material slip and friction. Furthermore, during the pure bending test, the strain gradient through the thickness is kinematically prescribed because the specimen is subjected to a plane strain condition in the direction parallel to the rotational axis (Tan et al., 1995), which allows for a straightforward investigation of the simulation results.

To carry out the finite element simulations, the calibrated material model for rolled AZ31 which is implemented in the finite element code ZeBuLoN (Besson et al., 1998) is used as a material library plugin for finite element solver Abaqus. Two types of material models are used: calibrated modified CPB2006 as well as von Mises with the hardening evolution taken from the uniaxial tensile test. The 4 nodes shell element S4 was selected for the simulation. The boundary condition is shown in Fig. 4.17. The displacement of nodes a and b is constraint along x and y direction. The rotation around the y direction is applied on c and d. The simulation is performed with only one element since the strain distribution in the plane of the sample is uniform.

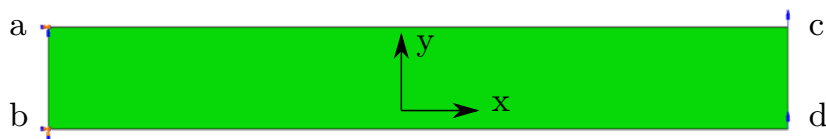


Figure 4.17: Boundary condition for the pure bending simulation

The calculation of the bending moment-curvature diagrams using the observed stress-strain responses of test material is based on the Euler-Bernoulli beam theory (Bauchau and Craig, 2009). It assumes that:

1. The cross section is infinitely rigid in its own plane.
2. The cross section remains plane after deformation.
3. The cross section remains normal to its deformed axis.

Fig. 4.18 shows the geometry of the curved sheet. The z-axis is assumed to be

parallel to the thickness direction of the material. The bending strain ϵ_x and bending stress σ_x were determined as follows. The radius of the layer at which $\epsilon_x = 0$ (neutral line) is denoted as R . Its curvature $\kappa = 1/R$. The z -coordinate for the neutral line is z_0 . Then bending strain can be determined as

$$\epsilon_x = \frac{z - z_0}{R}. \quad (4.5)$$

The corresponding stress value σ_x can be obtained from the stress strain curve from the experiments.

Since the stretching force applied to the sheet is zero, the equilibrium equation in the z -direction must be satisfied as

$$\int_{z_1}^{z_2} \sigma_x w dz = 0, \quad (4.6)$$

where w is the width of the sheet.

The value of R in Eq. 4.5 was iteratively determined so that Eq. 4.6 was satisfied. The bending moment M , corresponding to R was determined as:

$$M = \int_{z_1}^{z_2} \sigma_x z w dz \quad (4.7)$$

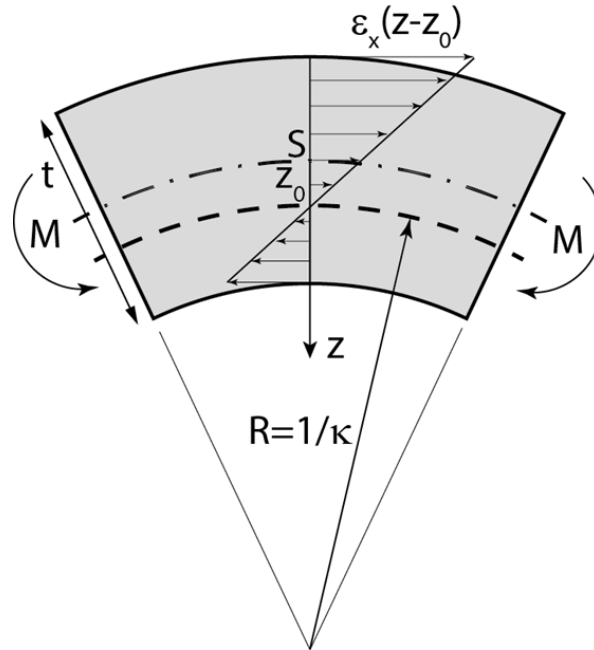


Figure 4.18: Geometry of the curved beam

In order to compare between the semi-analytical results and the simulation results, the bending moment-curvature diagrams are calculated using two sets of

experimental results: tension compression symmetric and asymmetric stress-strain curves. The tension compression symmetric curve is from the uniaxial tensile test result for rolled AZ31 along rolling direction. It corresponds with the simulation result using von Mises model. The tension compression asymmetric curves are the uniaxial stress strain curves obtained from both the uniaxial tension and compression tests. It corresponds with the simulation result using the modified CPB2006 model.

The simulated and semi-analytically calculated bending moment-curvature diagram was shown in Fig. 4.19. First, the simulation result using the modified CPB2006 model fits very good with the semi-analytical calculated result using the asymmetric experimental observations. Second, the moment-curvature diagram for the tension compression symmetric and asymmetric materials are different with each other. In the beginning, the bending moment for the symmetric material is higher than that of asymmetric material. This is because the yield stress in tension is much higher than that in compression in the beginning of the yielding, see Fig. 4.3 and Fig. 4.12. With the increasing of the yield stress in compression, the bending moment with the asymmetric material exceeds that of the symmetric material at last.

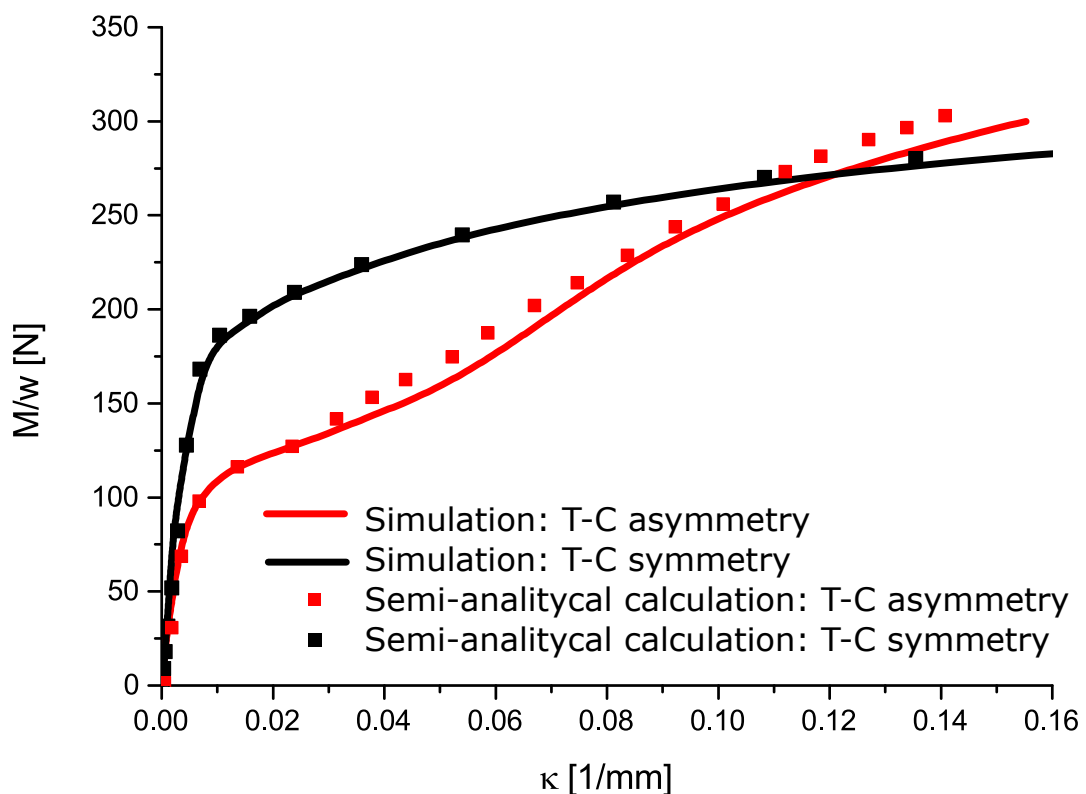


Figure 4.19: The simulated and semi-analytically calculated bending moment-curvature

In this chapter, the modified CPB2006 model was calibrated using a set of experimental results. The model can successfully describe the tension-compression asymmetry of wrought magnesium sheets. It was used in the pure bending simulation and predict the influence of tension-compression asymmetry to the bending moment-curvature diagram.

5 Crashworthiness of magnesium sheets structure

Design and production of structural components for vehicles are challenging tasks, involving the alloys selection and manufacturing processes, the structural design, and the subsequent crashworthiness analysis. For structural components in passenger cars in general, manufacturers need to prove energy absorption and structural integrity in case of crash scenarios.

The axially compressed columnar structures were generally employed to assess the crush behaviour of aluminium and steel structures (Alexander, 1960; Tarigopula et al., 2006; Wierzbicki et al., 1994; Abramowicz and Wierzbicki, 1989). In the early analytical studies, the material behaviour was assumed to be ideally plastic, which gave reasonably good predictions. Investigations of material system like foam-filled aluminium extrusions (Santosa et al., 2000) and carbon/epoxy composite tubes (Greve et al., 2008) were conducted using static and dynamic analyses. Recent studies about magnesium structures focus on the strain rate sensitivity of rolled sheets in tension Ulacia et al. (2011) and the failure pattern of extruded magnesium rods in axial compression.

In this chapter, the performance of different hollow rectangular structures under quasi-static axial compressive loading is investigated. The dissipated energy calculated from the experimental results was assessed to evaluate the crashworthiness of magnesium profile. The work in this chapter is published in Steglich et al. (2015) and Steglich et al. (2013).

5.1 Configurations and manufacturing of hollow rectangular profiles

Three types of prismatic profiles were produced to investigate the influence of the shape on the energy dissipation in the crush tests, see Fig. 5.1. Configuration a and b were produced from rolled sheets. Configuration a was made from pieces of rolled sheets by welding the edges using laser beam welding. For configuration b, the rolled sheets were first bent into two U shaped profiles and then welded along the flanges. Configuration a was processed for both AZ31 and ZE10 along RD and TD. Configuration b was only produced for ZE10, because bending did not work for AZ31 and cracks appeared at the rounded corner. Configuration c which is shown in the figure is extruded product which is the same with the material tested in Chapter 3. The outer dimension of the three configurations is 50 mm*50 mm*400 mm.

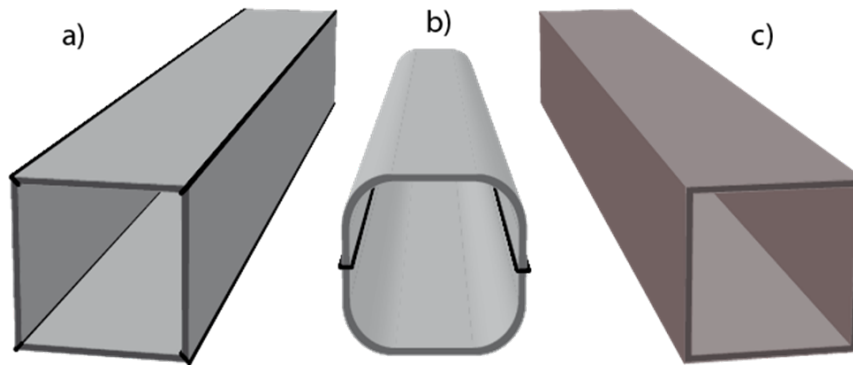


Figure 5.1: Different configurations of magnesium profiles investigated â welded along the ridges (a), bent and welded along the flanges (b) and extruded (c). Welds appear in black

5.2 Crush test

The crush tests were conducted at room temperature. A compressive axial force was applied on the specimen in a quasi-static condition with a cross-head velocity of 10 mm/min. The machine used for the crush tests is a Zwick universal testing machine. The cross head displacement and the load were recorded. A pair of studs of 40 mm height and clamps with screws was used (Abedrabbo et al., 2009) to prevent the non-axial motions of the profile during the tests. The profiles were first centred on the studs and then clamped along their circumference so that the effective buckling length of the profiles reduced to 320 mm. No initial geometrical imperfection was applied before the tests. For each configuration, at least two specimens were tested. All tests were terminated after global failure of the specimens and the crushing load decreased rapidly to half of the maximum force.

5.3 Finite element simulation

The implicit finite element code ABAQUS was used to predict the response of the thin-walled profiles subjected to axial crushing. The full sections of 320 mm length were modelled using quadrilateral fully integrated shell elements with four nodes, four integration points in the shells mid-plane and 21 section points throughout the thickness in order to accurately capture the element bending as suggested in Bron and Besson (2004). The thickness was adjusted to the measured wall thickness of the respective profile, i.e., 2.1 mm for configurations a and b, 1.7 mm in case of configuration c. The load was applied at the upper end of the specimen by prescribing the axial displacement, while the remaining displacement components as well as all rotations were suppressed. At the lower

end, all displacement and rotation components were suppressed in order to model the clamping. To account for the contact between the wrinkles during deformation, a self-contact algorithm without friction was used. No particular zone was introduced to model the welds, neither in case of configuration a, nor configuration b.

An initial geometrical imperfection is introduced to each of the profiles by superimposing the first eigenmode on the initial configuration extracted from a previous buckling analysis. This procedure avoids numerical problems at the bifurcation point. It does not enforce a specific folding pattern in the subsequent crushing analysis. The amplitude of the imposed imperfection generally affects the initial peak force. In the current investigation it was chosen to meet the initial peak load prior to buckling determined in the experiment. This led to a typical value for the amplitude of 0.08 mm.

In order to build a computational efficiency numerical model for the crush test, Hill's plastic potential (Hill, 1948) was selected as the material model. Considering that the big fraction of deformation in the crush test is compressive deformation, the neglect of the mechanical behaviour of tension in the material model will have no apparent influence on the simulation results. The isotropic hardening law extracted from compression tests of the respective materials was applied in the simulation. Hill's potential is implemented in the FE code ABAQUS, therefore it saves more simulation time compared to the developed model.

Hill's plasticity postulated that an equivalent stress is defined by

$$\bar{\sigma} = \sqrt{\frac{1}{2} [F(\sigma_{11} - \sigma_{22})^2 + G(\sigma_{22} - \sigma_{33})^2 + H(\sigma_{33} - \sigma_{11})^2 + 2L\sigma_{12}^2 + 2M\sigma_{23}^2 + 2N\sigma_{31}^2]}. \quad (5.1)$$

The six constants F , G , H , L , M , N describe the plastic anisotropy. From compression tests in the two orientations of orthotropy the constants F , G and H can be determined by considering the yield stress ratio and the (instantaneous) r-value. The constant N is usually determined by uniaxial tests along the 45 degree direction. Here, however, N was calibrated by minimising the variation of the r-value with the direction because the respective test data were not available. The remaining two constants L and M are associated to through-thickness stress components, which are neglected in the current study (plane stress state assumed).

Material failure was addressed by a phenomenological damage model, which is based on a critical (equivalent) failure strain defined as a function of the applied stress (Coelho et al., 2008). The dependence is expressed using the

shear stress ratio

$$\theta_s = \frac{\sigma^{eq} + 3k_s\sigma_m}{\tau_{max}}, \quad (5.2)$$

where σ^{eq} is the equivalent stress defined in Eq. 5.1, σ_m is the mean normal stress, k_s is the maximum shear stress and is a model parameter set as 0.3 (Coelho et al., 2008). The value of θ_s assigns the weight of mean stress in the shear stress ratio and hence affects the triaxiality-dependence of the damage initiation (El-Magd and Abouridouane, 2006).

The simulation of progressive failure generally requires a gradual reduction of the element's stiffness once a critical strain is reached. Hence, a strain-or alternatively a displacement-necessary to damage the respective finite element completely has to be provided. In this work, the damage evolution is considered to obey a stress-displacement law developed by Hokka et al. (2011). It requires the definition of effective plastic displacement

$$\bar{u}^{pl} = L\bar{\epsilon}^{pl}, \quad (5.3)$$

where L is the characteristic length of the element and $\bar{\epsilon}^{pl}$ is the equivalent plastic strain. Before damage initiation \bar{u}^{pl} and failure will occur if the effective plastic displacement at failure \bar{u}_f^{pl} is reached. As in an implicit code the erosion of elements is not foreseen, this stiffness reduction has to be treated carefully not to abolish the numerical convergence. A value of 0.25 for the effective plastic displacement at failure was found to be a good compromise between failure evolution rate and numerical convergence for all materials (typical element length was 2.99 mm). The damage initiation function was calibrated based on the equivalent failure strain in uniaxial compression ($\theta_s=2.2$) and biaxial compression ($\theta_s=2.4$). The equivalent failure strain in uniaxial compression is taken from the uniaxial compression test results, see Figure 1. The respective value for biaxial compression ($\theta_s=2.4$) was iteratively determined from the structural response during the crush experiment. The failure strain is specified as a tabular function of the shear stress ratio using the two sets of input data.

5.4 Results

Fig. 5.2 shows some of the tested profiles. The buckles formed progressively in the crash tests. Once one buckle was formed, it triggered its neighbor to evolve. For configuration a, the profiles made with AZ31 forms more buckles than that of ZE10 before the global failure of the structures. The buckling modes of configuration a and c are almost the same. For configuration c, the number of the buckles for AZ31 and ZE10 is the same. For configuration b

which is only produced using ZE10, only one buckle is formed before global failure.



Figure 5.2: Deformed profiles after crush test: configuration a (AZ31 and ZE10), configuration b (ZE10) and configuration c (AZ31 and ZE10, from left to right) (Steglich et al., 2015)

In the experiments, cracks initiate from the corner of the structure and propagate to the base material. Once a crack is initiated the crush force starts to decrease. If the axial displacement on the specimen is further increased, shear-compression cracks will propagate mainly perpendicular to the loading direction, see Fig. 5.3.

The buckling mode of the aluminium structure is different from that of the magnesium structure, see Fig. 5.4c. Because of the high ductility of aluminium 6060, global failure does not happen. Only small cracks were identified at the round corners of the buckles. The outer surfaces of every buckles contact each other and the inner surfaces of each buckle contact with itself. This is the common buckling modes observed in aluminium profiles, see Jensen et al. (2004).



Figure 5.3: Cracks initiated at the edges and propagated perpendicular to the loading direction for ZE10 configuration a (a) and configuration b (b) (Steglich et al., 2015)

Fig. 5.5 shows the force displacement curves of the crush tests. The force was normalised by the cross section of the structure in order to eliminate its effect. All simulation results reveal identical features with the tests. For AZ31, both configuration a and c reveal the same feature. The force increases linearly and reaches the maximum. This corresponds the uniform compressive deformation of the structure before the instability point. Then the force decreases and reaches a stabilised level during the formation of buckles. Before the global failure, the force increase linearly and reaches the second maximum point. This is related with the high work hardening rate of rolled AZ31. Failure is accompanied with a sharp drop of the load. For ZE10, the force-displacement record of configuration a and c has the similar feature with that of AZ31. The only difference is that the force record of configuration a did not show the second maximum point before the global failure of the structure. As already mentioned, the buckling modes of configuration b is generally different to the ones of configurations a and c, which is well visible in the crush force record. The force did not stabilise but decreased steadily, because only two buckles were formed before the global failure of the structure, see Fig. 5.4(b).

Because of the anisotropy of the magnesium sheets, the crush force of the configuration fabricated along TD is higher than that of RD for rolled AZ31.



Figure 5.4: The simulated deformation patterns of configuration a (a) and b (b) at global failure in comparison to the reference aluminium alloy (c) (Steglich et al., 2015)

It is just in the opposite for rolled ZE10. The force level of configuration c which is the extruded profile is much lower than that of configuration a for magnesium alloy ZE10. It is related with the different mechanical behaviour between the extruded material and rolled material. The deformation in the crush test is compression stress dominated. The yield stress in compression for extruded ZE10 is much lower than that of rolled ZE10, see Table 3.2. It explains the much lower normalised force record for configuration c compared with that of configuration a.

Assessment of crush tests

The specific mechanical work for each test was calculated to assess the performance of different configurations and alloys. The specific mechanical work W_u was calculated with the equation below. The representative axial displacement of 20 mm was selected as a basis,

$$W_u = \frac{1}{m} \int_0^u F(\tilde{u}) d\tilde{u}, \quad (5.4)$$

F is the axial crush force recorded during the experiment, u is the cross head

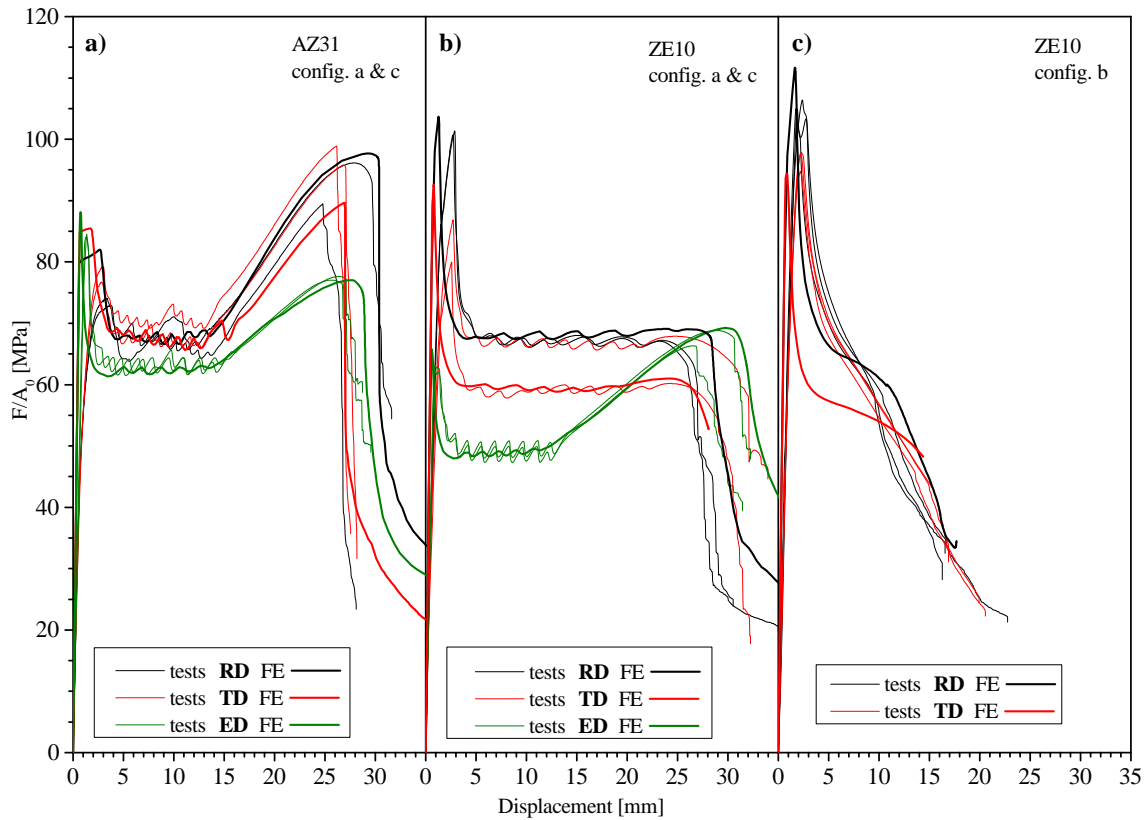


Figure 5.5: Normalised force-displacement records of crush tests; AZ31 (a), ZE10 (b) and ZE10 configuration b (c); “RD” and “TD” refer to the rolling and transverse direction of configuration a and b, “ED” to the extrusion direction of configuration c (Steglich et al., 2015)

displacement and m is the mass of the deformed volume.

Fig. 5.6 shows the specific mechanical work calculated for all of the tests. Configuration a absorbed more energy in the crush tests than other configuration. Caused by the second increase of force appeared before the global failure of the structure of AZ31 for configuration a, AZ31 shows higher specific energy than ZE10. For configuration b, its specific energy is lower than other configuration because only one buckle was formed before the global failure of the structure. Because of the anisotropy of rolled magnesium sheets, for AZ31 the specific energy of the structure which is fabricated along TD is higher than that of RD and this is inverted in case of ZE10.

For AZ31, the specific energy of configuration a is higher than that of configuration c, although the yield stress in uniaxial compression of extruded sheets is higher than that of rolled sheets, see Table 3.2.

The performances of different profiles cannot be only decided by the material characteristics. It requires a more detailed view on the structure: the thinner

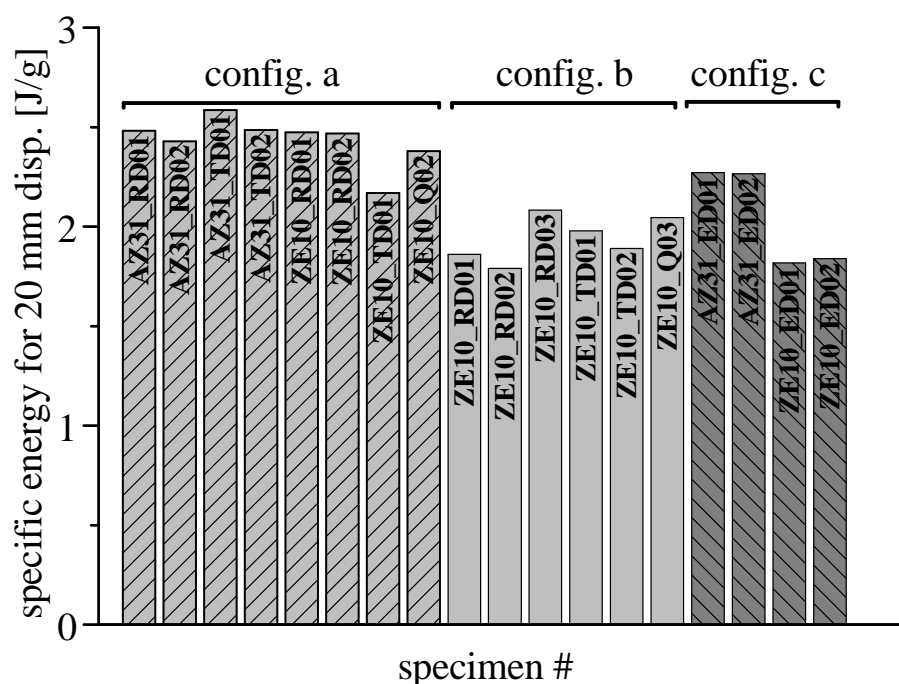


Figure 5.6: Specific energy calculated from the crush tests up to a global displacement of 20 mm

walls of configuration c (1.7 mm) causing lower surface moment (second order moment of inertia) leading to a less stiff response. For configuration c AZ31 gives a significantly higher energy than ZE10 because for extruded material the work hardening in uniaxial compression tests of AZ31 is higher than that of ZE10.

5.5 Discussion

The crashworthiness of magnesium structures is affected by several factors. First, the material which has higher work hardening rates evidenced in the uniaxial compression tests is conducive to higher specific energy. Second, the profile design influences the buckling modes and thus the energy dissipation. Third, high ductility of the material will improve the crushed length and end with high specific mechanical work.

The crush tests were conducted under quasi-static loading condition. However, in the crash scenarios, the strain rate effects should be included. Experimental investigation of the strain rate effects on magnesium sheets reports a positive strain rate effect (the stress increases with the increase of the strain rate)(Ulacia et al., 2011). The influence of the strain rate on the ductility of magnesium sheets is also observed for AZ80 (El-Magd and Abouridouane,

2006). The first aspect can be evaluated easily using numerical simulation by including rate-dependent hardening. For the later aspect, a deeper understanding of failure mechanisms is required. This can be achieved in case of tension, where strain localisation and damage are present, but it is not expected to have a major influence in compressive states.

The laser welding for configurations a and b was necessary to fabricate the crush elements from plane sheets. It was shown that the weld itself does not influence the crushing performance of the respective structure. The FE modelling reveals both, the macroscopic response and the crack initiation sites, with good accuracy without explicitly considering the weld. The macroscopic behaviour as well as cracking pattern are identical between configurations a (welded) and c (not welded). Although the stress triaxiality is high near the edges and failure starts at this point, the local strain at failure is not reduced significantly compared to the uniaxial (compression) experiment. The reported decrease of ductility for AZ31 laser welds (Coelho et al., 2008) do not take effect here and the crashworthiness of the profiles is not altered by the weld.

The material model parameters and the isotropic hardening used for the crash test simulation are based on the experimental result from uniaxial compression tests results, which prove to be reasonable because compression is dominant in crush deformation. For a more general assessment this assumption should be carefully checked.

The work presented here revealed that once magnesium profiles are considered as crash boxes for vehicles, the fabrication requires either extrusion facilities (favoured for mass production) or joining technology (small batch production). The latter turns out to be favoured with respect to its energy absorption.

6 Summary and conclusion

The present work deals with the characterisation of the plastic behaviour of the wrought magnesium sheets. Rolled sheets and extrusions of two alloys AZ31 and ZE10 were studied experimentally. For the rolled sheets, the standard uniaxial tensile tests were conducted along both rolling direction and transverse direction. Two sets of extensometers were used to record the longitudinal and the transversal strains. For the extruded product, the micro-tensile test along the transverse direction was performed instead of the conventional tensile test due to the size limitation. A cube specimen glued with magnesium sheets was used to conduct the uniaxial in-plane compression test. Two independent sets of extensometers were used to record the longitudinal and transversal strains. This compression testing method was successfully validated by an experimental facility using a comb-shaped die and a single sheet. The equi-biaxial tension behaviour of the materials was assessed with the through thickness compression test using layer specimens. The experimental results were compared with that of hydraulic bulge and cruciform specimen tests and find a good agreement. Much higher failure strain was achieved because plastic instabilities were suppressed using this testing method. The U-notched bar tensile tests and the shear tests were conducted to investigate the mechanical behaviour at higher levels of stress triaxiality and shear stress state respectively.

The measured behaviour was correlated with the microstructural information. Certain trends could be explained through the fundamental deformation mechanisms present in magnesium alloys. The rolled sheets AZ31 and extruded product AZ31 and ZE10 shows very strong basal texture. The rolled sheets ZE10 exhibit a significantly weaker texture. An evolving strength differential effect in both flow stress and r-value response of all materials was observed. Both of the flow stress and the r-value exhibits anisotropy for all the material. The compressive r-values are generally lower than the tensile r-values. Because of less strong basal texture, rolled sheets ZE10 did not show very strong strength differential effect and differential hardening under biaxial loading condition like other materials, but it shows stronger stress anisotropy in the uniaxial tensile tests and the U-notched bar tensile tests along two orientations.

A phenomenological 3D plasticity model was proposed based on the CPB2006 yield function. To capture the evolving tension compression asymmetry, the strength differential effect parameter k was considered to vary continuously with plastic multiplier but vary differently in tension and compression. The anisotropy coefficients included in the liner transformation tensor of the yield function were also considered to be a function of plastic multiplier in order to account for the distortional hardening behaviour. The numerous model

parameters were determined by minimising the difference between the experiments on different samples over the entire range of deformation until fracture. The stress and strain measurements in the uniaxial tensile and compression tests, the through thickness compression tests, the U-notched bar tensile tests and the shear tests were included in the model parameter optimisation. The calibrated model was employed in the numerical analyses of pure bending simulation which includes both tension and compression stress states. The bending moment-curvature diagram was calculated semi-analytically based on the Euler-Bernoulli beam theory. The simulated bending moment-curvature diagram fits very good with the semi-analytically calculated results. For the sake of comparison, an isotropic von Mises plasticity was also used. From the respective numerical results, it could clearly be seen that the proposed model leads to significantly better predictions. But it should be noticed that the developed model is limited in the application on the deformation including shear stress state because of the in-convexity of the model.

Finally, the crush tests were performed to assess the crashworthiness of magnesium sheet structures. An isotropic Hill plasticity model with the hardening evolution obtained from the uniaxial compression test results was employed in the numerical analyses of the crush test. It could clearly be seen that it leads to significantly good predictions. In summary, the Hill model based on the uniaxial compression test results is very promising for getting further insight in the crashworthiness analysis for magnesium sheet structures.

Bibliography

- N. Abedrabbo, R. Mayer, A. Thompson, C. Salisbury, M. Worswick, and I. v. Riemsdijk. Crash response of advanced high-strength steel tubes: Experiment and model. *International Journal of Impact Engineering*, 36:1044–1057, 2009.
- W. Abramowicz and T. Wierzbicki. Axial crushing of multicorner sheet metal columns. *Journal of Applied Mechanics*, 56:113–120, 1989.
- S. R. Agnew. Deformation mechanisms of magnesium alloys. In *Advances in wrought magnesium alloys*, pages 63–93. Woodhead Publishing Limited, 2012.
- S. R. Agnew. Plastic anisotropy of magnesium alloy AZ31B sheet. In *Essential Readings in Magnesium Technology*, pages 351–356. John Wiley Sons, 2014.
- S. R. Agnew and O. Duygulu. Plastic anisotropy and the role of non-basal slip in magnesium alloy AZ31. *International Journal of Plasticity*, 21:1161–1193, 2005.
- S. R. Agnew, C. N. Tomé, D. W. Brown, T. M. Holden, and S. C. Vogel. Study of slip mechanisms in a magnesium alloy by neutron diffraction and modeling. *Scripta Materialia*, 48:1003–1008, 2003.
- T. Al-Samman and G. Gottstein. Room temperature formability of a magnesium AZ31 alloy: Examining the role of texture on the deformation mechanisms. *Materials Science and Engineering: A*, 488(1-2):406–414, 2008.
- J. M. Alexander. An approximate analysis of the collapse of thin cylindrical shells under axial loading. *Imperial College of Science and Technology*, 13: 10–15, 1960.
- M. O. Andar, T. Kuwabara, and D. Steglich. Material modeling of AZ31 Mg sheet considering variation of r-values and asymmetry of the yield locus. *Materials Science and Engineering A*, 549:82–92, 2012.
- H. Aretz and S. Keller. On the non-balanced biaxial stress state in bulge-testing. *Steel Research International*, pages 738–743, 2011.
- D. H. Avery, W. F. Hosford, and W. A. Backofen. Plastic anisotropy in magnesium alloy sheets. *Trans. Metall. Soc.*, pages 71–78, 1965.
- ASTM B831-14. Standard test method for shear testing of thin aluminium alloy products. ASTM International, West Conshohocken, PA, 2014.

- F. Bachmann, R. Hielscher, and H. Schaeben. Texture analysis with mtex - free and open source software toolbox. *Solid State Phenomena*, 160:63–68, 2010.
- D. Banabic, H. J. Bunge, K. Poehlandt, and A. E. Tekkaya. *Formability of metallic materials*. Springer, 2000.
- Y. Bao and T. Wierzbicki. On fracture locus in the equivalent strain and stress triaxiality space. *International Journal of Mechanical Sciences*, 46:81–98, 2004.
- F. Barlat, J. C. Brem, J. W. Yoon, K. Chung, R. E. Dick, D. J. Lege, F. Pourboghrat, S. H. Choi, and E. Chu. Plane stress yield function for aluminium alloy sheets-part I: theory. *International Journal of Plasticity*, 19:1297–1319, 2003.
- P. D. Barros, M. C. Oliveira, J. L. Alves, and L. F. Menezes. Earing prediction in drawing and ironing processes using an advanced yield criterion. In *Key Engineering Materials*, volume 554, pages 2266–2276. Trans Tech Publ, 2013.
- O. A. Bauchau and J. I. Craig. Euler-bernoulli beam theory. In *Structural analysis*, pages 173–221. Springer, 2009.
- J. Besson, R. Leriche, R. Foerch, and G. Cailletaud. Object-oriented programming applied to the finite element method part II. application to material behaviors. *Revue européenne des éléments finis*, 7(5):567–588, 1998.
- J. P. Boehler, S. Demmerle, and S. Koss. A new direct biaxial testing machine for anisotropic materials. *Experimental Mechanics*, 34:1–9, 1994.
- R. K. Boger, R. H. Wagoner, F. Barlat, M. G. Lee, and K. Chung. Continuous, large strain, tension/compression testing of sheet material. *International Journal of Plasticity*, 21:2319–2343, 2005.
- J. Bohlen, M. R. Nürnberg, J. W. Senn, D. Letzig, and S. R. Agnew. The texture and anisotropy of magnesium-zinc-rare earth alloy sheets. *Acta Materialia*, 55:2101–2112, 2007.
- N. Bonora, D. Gentile, A. Pirondi, and G. Newaz. Ductile damage evolution under triaxial state of stress: theory and experiments. *International Journal of Plasticity*, 21:981–1007, 2005.
- P. W. Bridgman. The measurement of high hydrostatic pressure. I. A simple primary gauge. *Proceedings of the American Academy of Arts and Sciences*, 44:201–217, 1909.

- P. W. Bridgman. *Studies In Large Plastic Flow And Fracture: with Special Emphasis On the Effects of Hydrostatic Pressure*. McGraw, 1952.
- F. Bron and J. Besson. A yield function for anisotropic materials application to aluminum alloys. *International Journal of Plasticity*, 20(4):937–963, 2004.
- M. Brunig, O. Chyra, D. Albrecht, L. Driemeier, and M. Alves. A ductile damage criterion at various stress triaxialities. *International Journal of Plasticity*, 24:1731–1755, 2008.
- G. Çam, Ç. Yeni, S. Erim, V. Ventzke, and M. Koçak. Investigation into properties of laser welded similar and dissimilar steel joints. *Science and Technology of Welding & Joining*, 3(4):177–189, 1998.
- O. Cazacu and F. Barlat. A criterion for description of anisotropy and yield differential effects in pressure-insensitive metals. *International Journal of Plasticity*, 20:2027–2045, 2004.
- O. Cazacu, B. Plunkett, and F. Barlat. Orthotropic yield criterion for hexagonal closed packed metals. *International Journal of Plasticity*, 22:1171–1194, 2006.
- W. Z. Chen, X. Wang, E. D. Wang, Z. Y. Liu, and L. X. Hu. Texture dependence of uniform elongation for a magnesium alloy. *Scripta Materialia*, 67: 858–861, 2012.
- J. W. Christian and S. Mahajan. Deformation twinning. *Progress in Materials Science*, 39:1–157, 1995.
- R. S. Coelho, A. Kostka, H. Pinto, S. Riekehr, M. Kocak, and A. R. Pyzalla. Microstructure and mechanical properties of magnesium alloy AZ31B laser beam welds. *Materials Science and Engineering: A*, 485(1):20–30, 2008.
- J. C. Earl and D. K. Brown. Distributions of stress and plastic strain in circumferentially notched tension specimens. *Engineering Fracture Mechanics*, 8:599–611, 1976.
- E. El-Magd and M. Abouridouane. Characterization, modelling and simulation of deformation and fracture behaviour of the light-weight wrought alloys under high strain rate loading. *International Journal of Impact Engineering*, 32:741–758, 2006.
- P. W. Flynn, J. Mote, and J. E. Dorn. On the thermally activated mechanism of prismatic slip in magnesium single crystals. *Transactions of the TMS-AIME*, 221:1148–1154, 1961.

- T. D. Ghaffari, M. J. Worswick, U. Ali, and M. A. Gharghoury. Mechanical response of AZ31B magnesium alloy: Experimental characterization and material modeling considering proportional loading at room temperature. *International Journal of Plasticity*, 55:247–267, 2014.
- L. Greve, A. K. Pickett, and F. Payen. Experimental testing and phenomenological modelling of the fragmentation process of braided carbon/epoxy composite tubes under axial and oblique impact. *Composites Part B: Engineering*, 39:1221–1232, 2008.
- J. W. Hancock and A. C. Mackenzie. On the mechanisms of ductile failure in high-strength steels subjected to multi-axial stress-states. *Journal of the Mechanics and Physics of Solids*, 24:147–160, 1976.
- F. E. Hauser, P. R. Landon, and J. E. Dorn. Deformation and fracture of alpha solid solutions of lithium in magnesium. *Transactions of the ASM*, 50:856–883, 1958.
- R. Hill. The theory of the yielding and plastic flow of anisotropic metals. *Proceeding of the Royal Society A*, 193:281–297, 1948.
- R. Hill and J. W. Hutchinson. Differential hardening in sheet metal under biaxial loading: A theoretical framework. *Journal of Applied Mechanics*, 59:S1–S9, 1992.
- R. Hill, S. S. Hecker, and M. G. Stout. An investigation of plastic flow and differential work hardening in orthotropic brass tubes under fluid pressure and axial load. *International Journal of Solids and Structures*, 31:2999–3021, 1994a.
- R. Hill, S. S. Hecker, and M. G. Stout. An investigation of plastic flow and differential work hardening in orthotropic brass tubes under fluid pressure and axial load. *International Journal of Solids and Structures*, 31:2999–3021, 1994b.
- M. Hokka, J. Seidt, T. Matrka, A. Gilat, V. T. Kuokkala, J. Nykänen, and S. Müller. Compression behavior of near-UFG AZ31 Mg-alloy at high strain rates. In *Dynamic Behavior of Materials, Volume 1*, pages 295–301. Springer, 2011.
- Ø. Jensen, M. Langseth, and O. S. Hopperstad. Experimental investigations on the behaviour of short to long square aluminium tubes subjected to axial loading. *International Journal of Impact Engineering*, 30:973–1003, 2004.
- L. Jiang, J. J. Jonas, R. K. Mishra, A. A. Luo, A. K. Sachdev, and S. Godet. Twinning and texture development in two mg alloys subjected to loading along three different strain paths. *Acta Materialia*, 55:3899–3910, 2007.

- P. H. John and L. Jens. *Theory of Dislocations*. John Wiley Sons, New York, 1982.
- W. Johnson and J. L. Duncan. The use of the biaxial test extensometer. *Sheet Metal Ind.*, 42:271–275, 1965.
- J. Kang, D. S. Wilkinson, and R. K. Mishra. Inhomogeneous deformation of AZ31B magnesium sheet in uniaxial tension. In *Magnesium Technology 2011*, 2011.
- A. S. Khan, A. Pandey, T. Gnäupel-Herold, and R. Mishra. Mechanical response and texture evolution of AZ31 alloy at large strains for different strain rates and temperatures. *International Journal of Plasticity*, 27(5): 688–706, 2011.
- G. S. Kim. *Small volume investigation of slip and twinning in magnesium single crystals*. PhD thesis, Université de Grenoble, 2011.
- U. F. Kocks and D. G. Westlake. The importance of twinning for the ductility of CPH polycrystals. *Transactions of the TMS-AIME*, 239:1107–1109, 1967.
- T. Kuwabara, Y. Morita, Y. Miyashita, and S. Takahashi. Elastic-plastic behavior of sheet metal subjected to in-plane reverse loading. In *The fifth international symposium on plasticity and its current applications*, 1995.
- T. Kuwabara, S. Ikeda, and K. Kuroda. Measurement and analysis of differential work hardening in cold-rolled steel sheet under biaxial tension. *Journal of Materials Processing Technology*, 80-81:517–523, 1998.
- W. T. Lankford, S. C. Snyder, and J. A. Bausher. New criteria for predicting the press performance of deep drawing sheets. *Trans. ASM*, 42:1197–1205, 1950.
- X. Y. Lou, M. Li, R. K. Boger, S. R. Agnew, and R. H. Wagoner. Hardening evolution of AZ31B Mg sheet. *International Journal of Plasticity*, 23:44–86, 2007.
- J. Lubliner. *Plasticity theory*. Dover Publications, 2008.
- L. W. F. Mackenzie and M. O. Pekguleryuz. The recrystallization and texture of magnesium-zinc-cerium alloys. *Scripta Materialia*, 59:665–668, 2008.
- A. Makinde, L. Thibodeau, and K. W. Neale. Development of an apparatus for biaxial testing using cruciform specimens. *Experimental Mechanics*, 32: 138–144, 1992.

- M. N. Mekonen, D. , J. Bohlen, D. Letzig, and J. Mosler. Mechanical characterization and constitutive modeling of Mg alloy sheets. *Materials Science and Engineering: A*, 540:174 – 186, 2012.
- P. B. Mellor and A. Parmar. *Computational inelasticity*. Springer, 1978.
- M. Merklein and A. Kuppert. A method for the layer compression test considering the anisotropic material behavior. *International Journal of Material Forming*, 2:483–486, 2009.
- R. v. Mises. Mechanik der festen Körper im plastisch-deformablen Zustand. *Mathematisch-Physikalische Klasse*, pages 582–592, 1913.
- R. v. Mises. Mechanik der plastischen Formänderung von Kristallen. *Journal of Applied Mathematics and Mechanics*, 8:161–185, 1928.
- R. K. Mishra, A. K. Gupta, P. R. Rao, A. K. Sachdev, A. M. Kumar, and A. A. Luo. Influence of cerium on the texture and ductility of magnesium extrusions. *Scripta Materialia*, 59:562–565, 2008.
- T. Obara, H. Yoshinaga, and S. Morozumi. $(112\bar{2})[\bar{1}\bar{1}23]$ slip system in magnesium. *Acta Metallurgica*, 21:845–853, 1973.
- L. Prandtl. Spannungsverteilung in plastischen Körpern. In *Proceedings of the first International Congress for Applied Mechanics*, pages 43–46, Delft, 1924.
- A. Reuss. Berücksichtigung der elastischen Formänderung in der Plastizitätstheorie. *Journal of Applied Mathematics and Mechanics*, 10:266–274, 1930.
- A. Reyes, M. Eriksson, O. G. Lademo, O. S. Hopperstad, and M. Langseth. Assessment of yield and fracture criteria using shear and bending tests. *Materials Design*, 30:596 – 608, 2009.
- C. S. Roberts. *The deformation of magnesium*. John Wiley Sons, New York, 1964.
- S. P. Santosa, T. Wierzbicki, A. G. Hanssen, and M. Langseth. Experimental and numerical studies of foam-filled sections. *International Journal of Impact Engineering*, 24:509–534, 2000.
- J. Scott, M. Miles, D. Fullwood, B. Adams, A. Khosravani, and R. K. Mishra. Room temperature shear band development in highly twinned wrought magnesium AZ31B sheet. *Metallurgical and Materials Transactions A*, 44:512–516, 2012.

- J. W. Senn and S. R. Agnew. Texture randomization during thermomechanical processing of a magnesium-yttrium-neodymium alloy. In *Magnesium Technology in the Global Age*, 2006.
- E. Shiratori and K. Ikegami. Experimental study of the subsequent yield surface by using cross-shaped specimens. *Journal of the Mechanics and Physics of Solids*, 16:373–394, 1968.
- D. Steglich, W. Brocks, J. Bohlen, and F. Barlat. Modelling direction-dependent hardening in magnesium sheet forming simulations. *International Journal of Material Forming*, 4:243–253, 2011.
- D. Steglich, Y. Jeong, M. O. Andar, and T. Kuwabara. Biaxial deformation behaviour of AZ31 magnesium alloy: Crystal-plasticity-based prediction and experimental validation. *International Journal of Solids and Structures*, 49:3551–3561, 2012.
- D. Steglich, J. Bohlen, X. Tian, S. Riekehr, N. Kashaev, and S. Bargmann. Crashworthiness of magnesium sheet structures. *Materials Science Forum*, 765:590 – 594, 2013.
- D. Steglich, X. Tian, J. Bohlen, and T. Kuwabara. Mechanical testing of thin sheet magnesium alloys in biaxial tension and uniaxial compression. *Experimental Mechanics*, 54(7):1247–1258, 2014.
- D. Steglich, X. Tian, J. Bohlen, S. Riekehr, N. Kashaev, K. U. Kainer, and N. Huber. Experimental and numerical crushing analyses of thin-walled magnesium profiles. *International Journal of Crashworthiness*, 20(2):177–190, 2015.
- D. Steglich, X. Tian, and J. Besson. Mechanism-based modelling of plastic deformation in magnesium alloys. *European Journal of Mechanics - A/Solids*, 55:289–303, 2016.
- M. G. Stout, S. S. Hecker, and R. Bourcier. Evaluation of anisotropic effective stress-strain criteria for the biaxial yield and flow of 2024 aluminum tubes. *Journal of Engineering Materials and Technology*, 105, 1983.
- M. Taghvaipourm, J. Chakrabarty, and P. B. Mellor. The variation of the r -value in titanium with increasing strain. *International Journal of Mechanical Sciences*, 14:117–124, 1972.
- H. Takayuki and T. Hirohiko. Crystal plasticity finite-element simulation of work-hardening behavior in a magnesium alloy sheet under biaxial tension. *Computational Materials Science*, 51:156–164, 2012.

- Z. Tan, B. Persson, and C. Magnusson. Plastic bending of anisotropic sheet metals. *International journal of mechanical sciences*, 37(4):405–421, 1995.
- V. Tarigopula, M. Langseth, O. S. Hopperstad, and A. H. Clausen. An approximate analysis of the collapse of thin cylindrical shells under axial loading. *International Journal of Impact Engineering*, 32:847–882, 2006.
- G. I. Taylor. Plastic strain in metals. *Journal of the Institute of Metals*, 62:307–338, 1938.
- Y. Tozawa. Plastic deformation behavior under conditions of combined stress. In *Mechanics of Sheet Metal Forming*, pages 81–110. Springer US, 1978.
- I. Ulacia, C. P. Salisbury, I. Hurtado, and M. J. Worswick. Tensile characterization and constitutive modeling of AZ31B magnesium alloy sheet over wide range of strain rates and temperatures. *Journal of Materials Processing Technology*, 211:830–839, 2011.
- H. Wang, M. Wan, X. Wu, and Y. Yan. The equivalent plastic strain-dependent yld2000-2d yield function and the experimental verification. *Computational Materials Science*, 47(1):12–22, 2009.
- J. Wendt, K. U. Kainer, G. Arruebarrena, K. Hantzsche, J. Bohlen, and D. Letzig. On the microstructure and texture development of magnesium alloy ZEK100 during rolling. In *Magnesium Technology 2009*, pages 289–605. John Wiley Sons, Inc., 2009.
- T. Wierzbicki, L. Recke, W. Abramowicz, and T. Gholami. Stress profiles in thin-walled prismatic columns subjected to crush loading - I. compression. *Computers Structures*, 51:611–623, 1994.
- Wikipedia. von Mises yield criterion – Wikipedia, the free encyclopedia. https://en.wikipedia.org/wiki/Von_Mises_yield_criterion. [Online; accessed 31-January-2017].
- B. C. Wonsiewicz and W. A. Backofen. Plasticity of magnesium crystals. *Transactions TMS-AIME*, 239:1422–1431, 1967.
- S. B. Yi, J. Bohlen, F. Heinemann, and D. Letzig. Mechanical anisotropy and deep drawing behaviour of AZ31 and ZE10 magnesium alloy sheets. *Acta Materialia*, 58:592–605, 2010.
- R. F. Young, J. E. Bird, and J. L. Duncan. An automated hydraulic bulge tester. *Journal of Applied Metalworking*, 2:11–18, 1981.
- S. L. Zang, S. Thuillier, A. Le Port, and P. Manach. Prediction of anisotropy and hardening for metallic sheets in tension, simple shear and biaxial tension. *International Journal of Mechanical Sciences*, 53(5):338–347, 2011.

Lebenslauf

Name	Tian
Vorname	Xiaowei
Geburtsdatum	23.12.1987
Geburtsort, -land	Anhui Provinz, PR China
01.2012 - 12.2015	Studium an der Helmholtz-Zentrum Geesthacht in Simulation von Werkstoff- und Strukturverhalten
09.2009 - 12.2011	Studium an der Huazhong University of Science & Technology in Material Processing Engineering Abschluss: Master
09.2005 - 07.2009	Studium an der Hefei university of Technology in Material Forming and Control Engineering Abschluss: Bachelor